Faculdade de Engenharia da Universidade do Porto

A Wearable High-Accuracy Hand Sensing System

Diogo Alexandre Mendes da Costa

Dissertação realizada no âmbito do
Mestrado Integrado em Bioengenharia
Major Engenharia Biomédica

Supervisor: João Paulo Trigueiros da Silva Cunha
Collaborator: Duarte Filipe Dias
Collaborator: Nuno Ferreira

September 17, 2018

Resumo

As limitações na força e na cinemática da mão e do pulso podem debilitar drasticamente um individuo com impacto direto no seu bem-estar, impedindo-o de realizar eficientemente as suas atividades diárias. Estes casos estão geralmente relacionados com patologias como artrite, AVC, doença de Parkinson, entre outras. Na prática clínica são utilizados dispositivos convencionais combinados com metodologias simples de forma a realizar uma avaliação esporádica e intervir na apreciação da reabilitação. De modo geral, estes dispositivos têm como principais objetivos a medição dos ângulos máximos de cada articulação e a força em algumas posições de interesse, no entanto estes começam a tornar-se obsoletos. Assim, é de extrema importância o desenvolvimento de dispositivos tecnológicos que auxiliem o diagnóstico destas limitações através de parâmetros objetivos.

Esta dissertação tem como objetivo desenvolver um novo protótipo de um dispositivo vestível (baseado em tecnologia IMUs) acompanhado de uma plataforma de visualização e processamento, para medir a amplitude máxima nos diferentes movimentos do pulso. A este trabalho foi ainda incorporado o algoritmo de quantificação de rigidez já implementado. Trabalho este desenvolvido ao abrigo do projeto BioGlove no INESC TEC em parceria com a Biodevices S.A., incluindo ainda o projecto iHandU do INESC TEC.

Assim, a primeira fase de implementação consistiu na integração do hardware e no desenvolvimento do firmware para aquisição dos dados inerciais, calibração dos sensores e envio dos dados através do Bluetooth de baixa energia para a aplicação Android. A segunda fase compreendeu um estudo para a otimização do algoritmo de estimação da orientação baseada nos dados dos IMUs, a implementar posteriormente na aplicação Android. Na terceira fase, assumindo um papel central no sistema, foi desenvolvida uma aplicação Android para receber os dados do protótipo, realizar a avaliação e comunicar com a base de dados onde as avaliações são guardadas. Por fim, a quarta e última fase contemplou o desenvolvimento de uma plataforma web para visualização das avaliações e gestão da base de dados, com o objetivo de produzir um sistema completo e de arquitetura escalável. De uma visão global, os médicos que utilizem este sistema podem realizar a avaliação de forma simples, intuitiva e tecnológica, disponibilizando as avaliações em qualquer dispositivo.

No final, o protótipo desenvolvido como prova de conceito comprova a possibilidade de avaliar parâmetros cinemáticos do pulso a partir de sensores inerciais com precisão, encontrando-se preparado para a próxima integração. Desta forma, o trabalho desenvolvido contribui com mais uma parcela para o avanço dos dispositivos vestíveis na área de diagnóstico médico assistido.

Abstract

The limitation of strength and kinematics in hand and wrist can drastically debilitate the well-being of an individual, preventing him from achieving the daily activities effectively. These cases are usually related to pathologies such as arthritis, stroke, Parkinson's disease, among others. In clinical practice, conventional devices combined with simple methodologies are used to perform a sporadic assessment and intervene during rehabilitation. In general, these devices aim to measure the maximum angles of each joint and the strength in some positions of interest. However, they are becoming obsolete. Thus, it is imperative to develop technological devices to assist in the evaluation of these limitations through objective parameters.

This dissertation aims to develop a new prototype of a wearable device (based on IMUs technology) combined with a visualization and processing platform to measure the range of motion in the wrist. To this work was incorporated the quantification of the rigidity algorithm already implemented. This work was developed under the BioGlove project at INESC TEC in partnership with Biodevices S.A., being included the iHandU project of INESC TEC.

Thus, the first phase of implementation consisted in the hardware integration and firmware development for inertial data acquisition, sensors calibration, and data transmission via Bluetooth Low-Energy to an Android application. The second phase comprised a study for the optimization of the orientation's estimation algorithm based on IMUs data to be implemented in the Android application. In the third phase, assuming a central role in the system, an Android application was developed to receive the data from the prototype, perform the evaluation and communicate with the database where the evaluations are saved. Finally, the fourth and final phase included the development of a web platform for visualization of evaluations and database management, with the aim of producing a complete and scalable architecture of the system. The physicians who use this system can carry out the evaluation in a simple, intuitive and technological way, making the evaluations available on any device.

In the end, the developed prototype as a proof of concept proves the possibility of accurately assessing the kinematic parameters of the wrist using inertial sensors, being prepared for the next iteration. The Android application and the web platform complete a system with a more significant number of functionalities, allowing the evaluation to be made and conclusions to be drawn in a simple, intuitive and technological way. Thus, the work developed contributes to another portion for the advancement of wearable devices in assisted medical diagnosis.

Agradecimentos

Em primeiro lugar gostaria de agradecer à minha família, principalmente aos meus pais e aos meus avós por me proporcionarem a oportunidade e o caminho até esta nova fase que se avizinha. Gostaria ainda de agradecer a todas as pessoas que sempre me acompanharam durante todo o percurso, e que proporcionaram grandes momentos e grandes lembranças. Momentos estes que espero que no futuro continuem a ser tão bons ou melhores como os aconteceram até aqui.

Relativamente a esta dissertação, em primeiro lugar gostaria de agradecer ao Professor Doutor João Paulo Cunha pela oportunidade de realizar este trabalho, sempre com a vertente de futura aplicabilidade em soluções reais, tornando-se mais do que um vulgar projeto. Gostaria também de agradecer a sua partilha de conhecimento para que o trabalho cumprisse da melhor forma os requisitos. Quero ainda deixar uma palavra de apreço a todos os membros do BRAIN Lab, principalmente ao Duarte Dias por toda a orientação e total disponibilidade para discutir decisões, possíveis soluções e aprimoramentos do trabalho. Por último, gostaria de agradecer a disponibilidade de todas as pessoas que deram o seu contributo para esta dissertação.

Contents

List of Figures

List of Tables

Abbreviations and Symbols

List of abbreviations (alphabetical order)

ADC	Analog-to-Digital Converter
CMC	Carpometacarpal joint
DCM	Direction Cosine Matrix
DIP	Distal interphalangeal joint
DoF	Degree of Freedom
DPM	Digital Motion Processor™
ECF	Explicit Complementary Filter
GATT	Generic Attribute Profile
GDCF	Gradient Descent Based Complementart Filter
IMU	Inertial Measurement Unit
I^2C	Inter-Integrated Circuit
IC	Integrated Circuit
IDE	Integrated Development Environment
IoT	Internet of Things
IT	Information Technology
IP	Interphalangeal joint
MARG	Magnetic, Angular Rate and Gravity Module
MCP	Metacarpophalangeal joint
MEMS	Micro Electrical Mechanical Systems
OA	Osteoarthritis
PD	Parkinson´s Disease
PHS	Personal Health Systems
PIP	Proximal interphalangeal joint
RA	Rheumatoid arthritis
ROM	Range of Motion
SCI	Spinal Cord Injury
SPI	Serial Peripheral Interface

SSc	Systemic sclerosis
SWS	Smart Wearable Systems
TBI	Traumatic Brain Injury
UART	Universal Asynchronous Receiver-Transmitter
UI	User Interface
UML	Unified Modeling Language
UUID	Universally Unique Identifier
WHS	Wearable Health Systems
WMSD	Work-related musculoskeletal disorders
XML	Extensible Markup Language

List of symbols

ω	Angular velocity
ψ	Yaw/heading
θ	Pitch
Φ	Roll

Chapter 1

Introduction

1.1 - Background and Context

The hand and wrist allow a wide range of tasks, from the simplest to the most complex. These have always been important to the human being, inferring the ability to build and communicate, and allowing him to create our current society [1, 2].

The limitations in kinematics and strength of these structures come from a variety of pathologies such as arthritis, stroke, Parkinson's disease and many others with less prevalence in the population. Additionally, the hand-wrist complex is a fundamental and active part of the human body, becoming vulnerable to work-related pathologies. These injuries, in more severe cases can lead to disability, impairing the performance of the individual on daily tasks and at the workplace [3].

At the moment there are already some devices in the clinical environment capable of objectively evaluate kinematics and strength limitations of the hand and wrist, which are combined with the help of questionnaires and professional experience [4]. These devices measure the maximum angles made by one joint at a time and the strength in some specific cases, usually related to grasp and pinch movements [5]. As a result, this methodology presents an unfeasible process regarding time efficiency and costs associated with the duration of the exam. From a more technological point of view, there are already devices in the market that have the potential to have a positive impact in such areas. Nevertheless, these have been specially developed with the intention of being used in animation and virtual reality. Given the lack of such a tool in the clinical environment, there is a need to create an easy-to-use device, taking advantage of the recent exponential technological growth of mobile devices and wearable health systems.

The work developed in this dissertation is based on the BioGlove and iHandU projects developed by the Biomedical Research And INnovation (BRAIN) group hosted in INESC TEC, and supervised by Professor Ph.D. João Paulo Cunha. This work is intended to improve the BioGlove project through a prototype as a proof of concept with new sensors to measure the maximum angles in the wrist, incorporating the innovation and leading development in the quantification of the motor improvements during the Deep Brain Stimulation (DBS) surgeries in charge of the iHandU project.

1.2 - Motivation

The lack of technological devices for this type of assessments gives to biomedical engineering an opportunity to improve the current systems regarding accuracy and time efficiency. This work integrates the relatively recent concepts of mobile devices and wearable health systems. Currently, these are two of the most promising concepts in medical technology. The choice of these concepts focuses on increasing knowledge in an emerging area with countless market opportunities in the near future, with the aim of improving the technology in the current clinical diagnoses. Throughout the work, the possibility of working in distinct areas with different programming languages allowed me to carry out an end-to-end project, making my knowledge more widespread.

In addition to this perspective, the opportunity to work on projects of INESC TEC in partnership with Biodevices, S.A. with the mentality to improve and develop new products that can be released in the market is a great incentive and enormous personal gratification.

1.3 - Objectives

In this dissertation, different areas and steps need to be covered to understand and implement a technological project in hand/wrist kinematics, with the primary goal of future application in the clinical environment. Consequently, this dissertation is segmented into 5 main objectives.

The first objective is to understand the complex working principle of hand and wrist, how the kinematic evaluation is performed by physicians and what parameters should be analyzed. Then, a study of the technological devices (on the market or being developed) with relevant features for this dissertation becomes crucial. From the technical point of view, it is still essential to build background knowledge in wearable health systems, especially their generic architecture and their standard operating principles. In addition to wearable health systems, it is necessary to acknowledge the operating principals of inertial measurement units and their differences, emphasizing the theoretical insight that makes these sensors a viable option for this project.

The second objective is to develop a glove prototype with the necessary hardware and firmware to acquire, process and send kinematic data via Bluetooth Low-Energy to the Android smartphone. This prototype will act as proof of concept for a new stage of the BRAIN group projects.

The third objective is to perform an offline processing from the data sent by the wearable device in order to understand the best algorithm to estimate the angles performed by the patient.

The fourth objective is to develop a simple and intuitive Android application to receive, process and illustrate the real-time kinematics evaluation of the patient's wrist from the data received by BLE. This application should have a central role in the system, allowing the storage of the performed evaluation and their upload to an online platform, providing a more user-friendly, structured, efficient and technological methodology to the health professional.

The fifth and final objective contemplates the development of a web platform consisted by a database and a website. This allows a greater management of the evaluation, extending the scalability of the project.

1.4 - Document Outline

This master thesis is divided into 5 chapters. After this introductory chapter, four other chapters contemplate all the state of the art necessary for the accomplishment of this dissertation, the prototype development process, the results obtained by comparison with devices currently used in the clinical environment, and finally the main conclusions and future work.

Having that said, chapter 2 covers the state of the art according to the existing literature in this area, beginning with the description of anatomy and biomechanics of hand and wrist. Thereupon, it is emphasized the kinematic parameters with clinical interest, providing some details regarding the evaluation of strength due to their complementarity. After this description, the epidemiology of the major pathologies that can cause some limitations respecting motion and strength in the anatomical regions of interest are highlighted, emphasizing the need for the development of a truly effective evaluation device in this area. The following topics portray the devices that are currently used for this type of evaluation and those that are already present in the market. These devices can converge to this area of interest since many of them have been designed with the same features but for different purposes. Also in Chapter 2, the fundamental bases of this project will be addressed, beginning with the description of the generic architecture of wearable health systems and the emerging market opportunity that is associated with the need for innovation in clinical practice. Finally, it will be given relevance to the theory of inertial sensors and the main considerations required to estimate the orientation of each sensor.

Chapter 3 describes the development phase of this dissertation. This chapter is segmented into the 5 main components (hardware, firmware, offline processing, Android application, and web platform), mentioning for each one the development methodology, their components and possible decisions/alternatives, results and problems found. In the final phase, it is represented an overall view of the entire system.

Chapter 4 illustrates the testing and validation process by comparing the prototype with the devices currently used in clinical practice, complemented by their discussion.

Last but not least, chapter 5 ends this master thesis by presenting some conclusions about the wearable health system prototype developed, in conjunction with some suggestions of future improvements and future work with the main goal of approaching the final product.

Chapter 2

State of Art

In this chapter, the necessary background for this dissertation will be portrayed constructively. Foremostly, this chapter starts by describing the basic knowledge of biology required for this thesis as well as notions about the assessment of kinematics and hand strength in the clinical environment, and the origin of these limitations.

Nearing the conclusion of the chapter, it will be highlighted the potential competing devices for the presented proposal, and it will be approached the fundamentals of this work from a more technological point of view.

2.1 - Hand Anatomy

The hand is the distal end of the upper extremity, and it is capable of a wide variety of functions, ranging from the simplest to the relatively complex tasks. Simple the tasks are usually related to gross motor movements, which allow to pick up heavier objects and perform more arduous work. On the other hand, complex tasks are associated with holding small objects and performing small and delicate tasks, which are some features of fine motor movements. These movements grant the essential and complex abilities, allowing communication, expressive articulation and functions with greater complexity than others living beings [1, 2].

2.1.1 - Bones and Joints

The human hand is made up of 27 small bones grouped by carpals (wrist bones), metacarpals and phalanges (proximal, middle and distal), as shown in figure 2.1. The fingers can be numbered from 1 to 5, commonly known as thumb, index (or pointer), long, ring and small, respectively. For further explanations, it will be followed the termination that most easily applies to the situation. Each of the five fingers contains a metacarpal and a group of phalanges. These small bones are articulated, and these joints are anatomically recognized as it will be described below [6].

The carpometacarpal joint (CMC) is an articulation between the proximal end of a metacarpal and the distal row of carpal bones. The connection between each metacarpal and

each carpal bone is shown in figure 2.1. In this case, the thumb has a saddle-type joint[1], while the remaining fingers have plane joints[2][6].

The metacarpophalangeal joint (MCP) is an articulation between the distal ends of the metacarpals and the proximal phalanges. In this joint, the structure in the thumb is also different from the remaining, being from hinge[3] and condyloid[4] type, respectively [6].

The interphalangeal joint (IP) is segmented into proximal interphalangeal (PIP) and distal interphalangeal joint (DIP) with the exception of the thumb. This one is an exception since it does not has the middle phalange. In the final type, there is congruence since all fingers have hinge joints [6].

In addition, the wrist also contains particular features, and it is the most complex at the bones and joints level. It is constituted by the 8 carpal bones oriented in two lines (proximal and distal) already mentioned and identified in figure 2.1 (B). These carpal bones are also articulated, similarly to the finger bones, in two main joints [6].

The radiocarpal joint is located between the distal part of the radius (concave), radioulnar disk and the proximal carpal row (convex), except the pisiform bone. This joint is being classified as a condyloid joint. The articular disk mentioned is a thin, oval plate of fibrocartilage located between the ulna and the proximal row of carpals. This plate acts as a shock absorber and fills the space between the distal ulna and its adjacent carpal bones—the triquetrum and lunate. This joint is still responsible for the transition of 80% of the force that passes through the wrist, from the scaphoid and the lunate to the radius. In people with bone problems, these bones can be easily fractured, given their functions [7]. The midcarpal joint is located between the two lines of the carpal bones, having a more irregular shape than the previous one and it is classified as a plane joint [6].

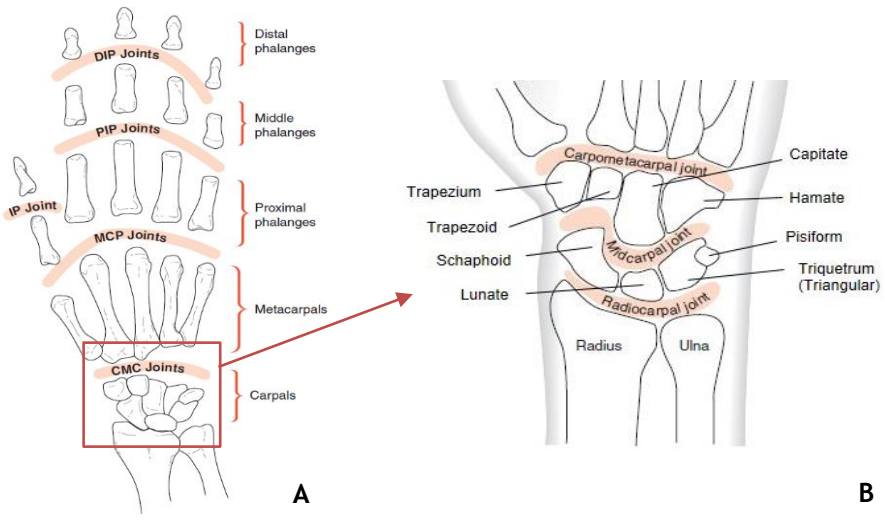

Figure 2.1- Joints and bones of the fingers and wrist. Denomination and location of bones and joints of the fingers in A (anterior view) and of the left wrist in B (anterior view) [6].

[1] Saddle joint has the opposing surfaces reciprocally concave-convex.

[2] Plane joint has the opposing surfaces of the bones flat or almost flat.

[3] Hinge joint has the articular surfaces molded in such a manner to allow motion only in one plane.

[4] Condyloid joint is an ovoid articular surface that is received into an elliptical cavity.

2.1.2 -Ligaments and Other Supporting Structures

This topic inherently refers to two structures: ligaments joint and capsules. Generally, ligaments are fibrous bands of connective tissue, mainly constituted by collagen (viscoelastic material) that bind adjacent bones. These structures have as main objective to provide stability and mobility limitation in articular zones. Although they have some elasticity, it is not always possible to return to the original state when extended the elastic limit point or by extended time [8].

The joint capsules are an envelope surrounding the joint which provides passive stability, limiting the movements. It is constituted by the fibrous membrane (external) composed of avascular fibrous tissue, structurally similar to the ligaments, and the synovial membrane (internal) responsible for the secretion of synovial fluid. The proper functioning of this structure allows retaining the synovial fluid, designed to reduce friction between the articular cartilage of synovial joints during movement [9, 10].

Anatomically, the hand-wrist complex concentrates at least 123 ligaments previously acknowledged by scientists. Although there are numerous structures in the hand, only a few are commonly referred in the literature given their kinematics functions, being these the most important in the scope of this dissertation. Table 2.1 shows the major hand and wrist ligaments as well as their respective main functions. Their positions and complex anatomical relationships can be found in figure 2.2 [6].

From a functional point of view, when the hand is relaxed, the bone skeleton and the ligaments tend to form a natural concavity in the palmar zone exhibiting essentially two laterals and a longitudinal arch, classified as proximal, distal and longitudinal, respectively. The proximal is formed by the carpals and the proximal end of the metacarpals, supported by the flexor retinaculum ligament. The distal is formed by the distal end of the metacarpal bones, and finally, the longitudinal arch that crosses the hand from the wrist to the phalanges of each finger. This configuration has implications in grip movements, which are extremely important for hand mobility in humans [6].

Table 2.1 - Prime ligaments of the hand-wrist complex [6, 11].

Ligaments	Observations
Hand (phalangeal and metacarpal region)	
Collaterals ligaments	Prevent sideways movement of the joint.
Volar Plates ligaments	The strongest ligaments in the hand have as main functions to reinforce the joint capsules, enhance stability and limit hyperextension.
Deep transverse metacarpal ligaments	Keep fingers from separating, which results in a constriction of the hand abduction [12, 13].
Hand (proximal region)	
Flexor retinaculum ligament	Its primary function involves holding the tendons located in the wrist and prevent the carpal bones from separating. Mutually with the carpal bones, they form a tunnel (carpal tunnel) where are crossed by nerves and tendons that follow for the most distal part of the hand.
Extensor retinaculum ligament	Its main function occurs essentially at extension, where it holds tendon extensors near the wrist.
Extensor expansion ligament	Generally named as extensor hood, its conformation allows us to balance the action of the extrinsic muscles.
Wrist	
Radial and ulnar collateral ligaments	They have similar functions to the collaterals referred in the fingers, i.e., provide lateral and medial support.
Palmar radiocarpal ulnocarpal ligaments	This one stands out by the limitation of the extension.
Dorsal radiocarpal ligament	Conversely to the palmar, since it is not so susceptible to excessive forces when it prevents excessive flexion of the wrist, it is not as tough as the previous one.

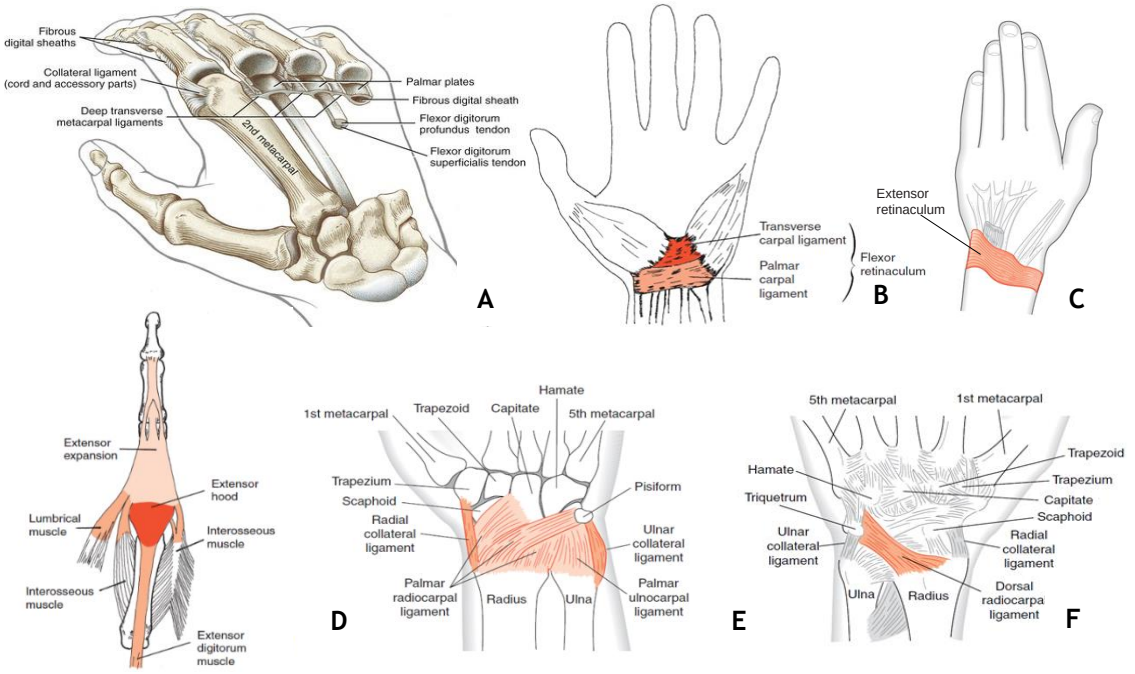

Figure 2.2 - Hand and wrist ligaments. In this figure it can be observed the ligaments of phalangeal and metacarpal region in A (posterior view), and the proximal region ligaments in B (anterior view), C (posterior view) and D (posterior view). The wrist ligaments wrist ligaments are illustrated in E (anterior view) and F (posterior view), both on the left wrist [6, 14].

2.1.3 - Muscles

The muscular system is responsible for all movements of the human body, and the muscles are classified as skeletal, smooth and cardiac. Since the study focuses on the distal end of the upper extremity and their motion abilities, only the skeletal muscles are relevant. This type is the only one that allows its voluntary control and performs all the necessary conscious actions for motion and communication of the human body. Notably, the majority of these muscles are attached to two bones across a joint, moving those bones closer to each other. This movement takes place when the muscular contraction is triggered by the excitation of its fibers by the motor nerves [15]. In addition, the hand-wrist complex is contemplated with more than 30 muscles working together in a highly complex way, reason why only those of greater relief for the movement and strength will be approached [16].

Starting with the hand muscles, the literature reveals a segmentation according to the place of insertion and then by its anatomical position. Contributing to this, muscles have a simple denomination, indicating in large part their action and actuation zone. These will not be identified for the most part in this topic, but other muscles may still have in their denomination the shape, number of heads, direction of the fibers, among others [6]. Most anatomists describe the muscles as extrinsic when their proximal attachment is above the wrist and as intrinsic when their proximal attachment is in the wrist region or distal to this. These last, although of smaller magnitude order when compared to the previous ones, are the main reason for fine motor control and precision movements previously mentioned [6].

Furthermore, the name of the muscles can provide some insight regarding their function and position, since the flexor muscles concentrate primarily on the anterior region, while the extensors concentrate on the posterior region acting as antagonists. In addition, these muscles can be classified according to their performance on the thumb or the remaining

fingers, given their distinct features. These muscles are generally described in table 2.2 and shown in figure 2.3 in order to reference their anatomical relationships [6].

Table 2.2 - Prime movers of the hand [6].

Action	Joint	Muscles (and adjacent nerves)
Thumb		
Flexion	CMC, MCP	*flexor pollicis brevis* (median nerve)
	IP (CMC,CMC)	*flexor pollicis longus*(median nerve)
Extension	CMC, MCP	*extensor pollicis brevis* (radial nerve)
	IP (MCP, CMC)	*extensor pollicis longus* (radial nerve)
Abduction	CMC	*abductor pollicis brevis*, *abductor pollicis longus* (radial nerve)
Adduction	CMC	*adductor pollicis* (ulnar nerve)
Opposition	CMC	*opponens pollicis* (median nerve)
Reposition	CMC	*adductor pollicis (ulnar nerve)*, *extensor pollicis longus* (radial nerve), *extensor pollicis brevis* (radial nerve)
Finger		
Flexion	MCP	*lumbricales* (median and ulnar nerves), *flexor digitorum superficialis* (median nerve), *flexor digitorum profundus* (median and ulnar nerves)
	DIP	*flexor digitorum superficialis* (median nerve), *flexor digitorum profundus* (median and ulnar nerves)
	PIP	*flexor digitorum profundus* (median nerve)
Extension	MCP	*Extensor digitorum*, *extensor indicis*, *extensor digiti minimi* (radial nerve)
	PIP, DIP	*Lumbricales* (median and ulnar nerves), *extensor digitorum* (radial nerve), *extensor digiti minimi* (radial nerve), *extensor indicis* (radial nerve)
Abduction	MCP	*dorsal interossei*, *abductor digiti minimi* (ulnar nerve)
Adduction	MCP	*palmar interossei* (ulnar nerve)
Opposition (fifth)	MCP	*opponens digiti minimi* (ulnar nerve)

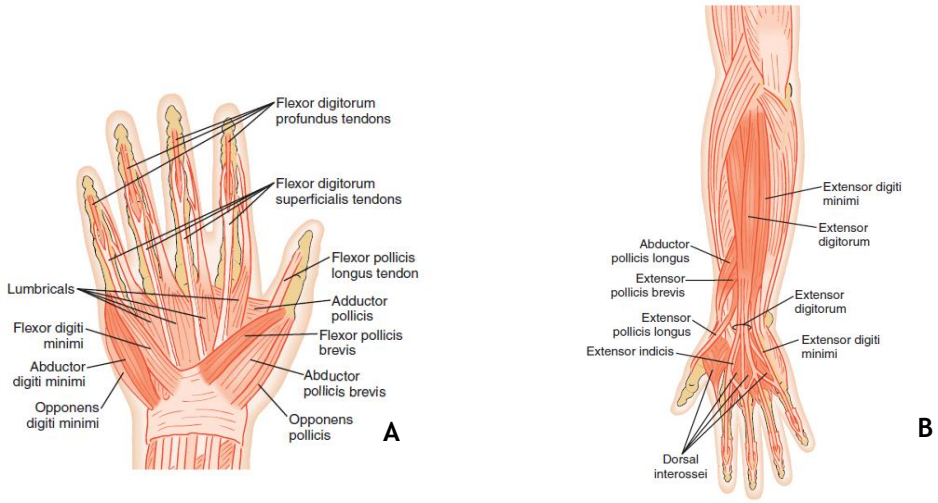

Figure 2.3 - Hand muscles. Anterior view in A and posterior view in B [6].

As before, it is verified that the wrist also has interesting structures for this dissertation, so with the muscles, it is no exception. There are 6 muscles that guarantee the movement of the wrist, which are divided into the anterior and posterior. The muscles in these regions also function as antagonists and are represented in table 2.3, and their anatomical relationships are illustrated in figure 2.4 [6].

Table 2.3 - Prime movers of the wrist [6].

Action	Muscles (and adjacent nerves)
Flexion	*flexor carpi radialis* (median nerve), *flexor carpi ulnaris* (ulnar nerve)
Extension	*extensor carpi radialis longus and brevis*, *extensor carpi ulnaris* (radial nerve)
Radial deviation	*flexor carpi radialis* (median nerve), *extensor carpi radialis longus* (radial nerve)
Ulnar deviation	*flexor carpi ulnaris* (ulnar nerve), *extensor carpi ulnaris* (radial nerve)

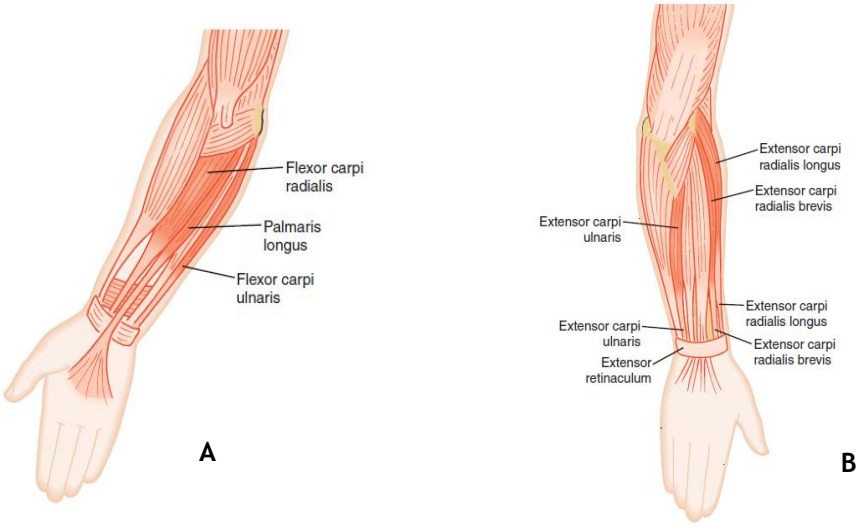

Figure 2.4 - Wrist muscles. Anterior view in A and posterior view in B [6].

Established the main anatomical components and their functions, it will be discussed in the next section in greater detail the movements so far referred. Parameters and their range of values for which these values are healthy will also be analyzed.

2.2 - Hand Kinematics

2.2.1 - Metrics and Parameters Evaluated

Patients with motion problems at the distal ends of the upper limbs usually perform the diagnosis through a wide range of methodologies. In this diagnosis, it is usual for the specialized physician to perform physical exams where he looks for swelling and tenderness, and evaluates the range of motion (ROM) of the joints. After this, antibody blood tests or imaging tests can be performed on some diseases and in more complex cases. In this subsection, it will be portrayed the parameters used in the physical examination as diagnosis or screening of possible musculoskeletal disorders [17]. Within the scope of this dissertation, it will now be studied the normal ROM values of the joints analyzed during the examination. To accomplish this, it is imperative to have some of the basic knowledge in kinematics beforehand.

Kinematics is a branch of classical mechanics that describes the movement of a point or object without considering its mass or forces that cause movement. The main goal is to provide its spatial description (position), the rate that they move (velocity) and the rate at which their velocity is changed (acceleration) [18].

The movements studied are often quantified by the degrees of freedom (DoF). These DoFs are defined as the number of independent parameters that define a system configuration in space [19]. When this mechanical ideology is transposed to the medical area, it is possible to use the work of ElKoura and Singh to model the hand-wrist complex in 27 DoFs: 4 on each finger, 5 on the thumb and 6 on the wrist [2]. However, this anatomically based hand model requires simplifications concerning the motion of the thumb and independence of fingers, joints, and motion of the hand. In the literature there are many other hand models, where DoFs vary between 22 and 29, depending on the degree of complexity [20].

Regarding the model of ElKoura and Singh, each finger has 4 DoFs, while 2 of them represent the flexion/extension in the 2 IPs between the phalanges, the remaining 2 represent the flexion/extension as well as abduction/adduction in the MCP. The thumb, as a reflection of its complex movements has 5 DoFs. For this finger, there is 1 DoF for flexion/extension in the IP, 2 DoFs for flexion/extension and abduction/adduction in the MCP and finally 2 DoFs for flexion/extension and abduction/adduction CMC. Note that there was a simplification in the MCP joint since it was considered to have similar movement ability as the other fingers. Anatomically, this joint is different from the remaining MCP joints and therefore only allows flexion/extension. The last 6 DoFs define the translation and rotation movements of the wrist. Anatomically, the 3 rotational DoFs can be defined as flexion/extension, abduction/adduction and supination/pronation between the carpals and the radius [21].

The aforementioned movements are restricted by the morphology and constitution of the hand, so it becomes possible to measure the ROMs of the joints. The evaluation of these ranges allows an objective assessment of the movements performed by the hand. This is a crucial diagnosis once the reduction of these ranges severely impairs the hand function [5].

The ROMs can be measured through two methodologies: active and passive. The active motion refers to the movements that the patient himself can achieve with the strength of his muscles. The passive motion refers to the freedom with which a joint moves when a force is applied [5]. Whereas the first methodology verifies the maximum parameters of movement for the patient, the second methodology specifically illustrates the stiffness of the joint under analysis. This passive methodology is only applied if abnormalities are detected in the active [22].

In order to quantify the angles achieved by the joints in the distal areas to the wrist, it must be taken into account that the wrist must be in a neutral position to allow the tendon excursion of long flexors and extensors of the fingers. To calculate the maximum angles of a particular joint on one finger, the same motion must be actively performed on the others to maximize the measured angle, independently of other adjacent muscles or ligaments. Initially, it will be discussed the standard values from the second to the fifth finger and subsequently to the first (thumb) [5].

Starting with the MCP joint, the normal range of motion in flexion/extension is 0º-90º, and there may be some hyperextension considered normal up to 45º, as shown in figure 2.5 [23]. There is no standardized technique to evaluate abduction/adduction. However, it is common to measure the distance between abducted fingers. This method has been used only as a follow-up of the treatment [22, 24]. Some authors, such as John Fox and Richard Day, affirm that the angle between the abducted finger and the longitudinal axis of the metacarpal can be measured, but other variables can affect the reliability of normal values

[25, 26]. The PIP and DIP joints, as previously mentioned, have similar anatomical constitutions. In this case, their ROMs are 0°-110° and 0°- 60°/70°, respectively [5].

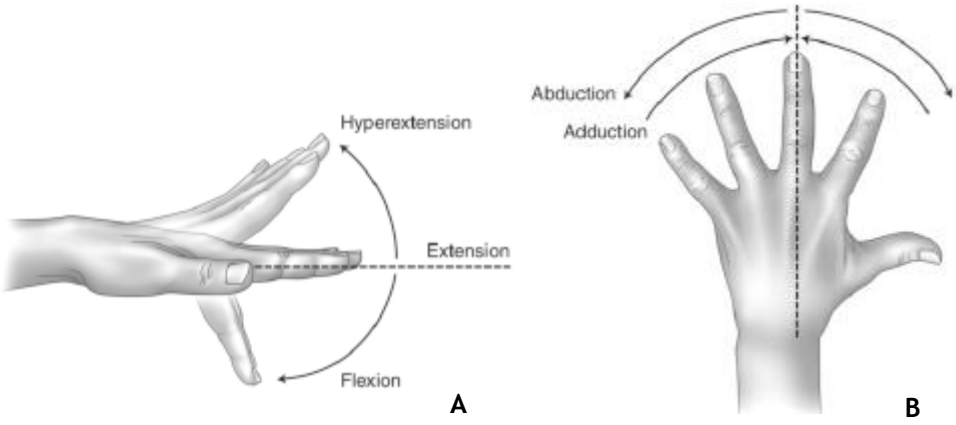

Figure 2.5 - Main movements of the MCP joint. The movement of flexion/extension in A and abduction/adduction in B [5].

The thumb has movement patterns much more complex and disparate when compared to the remaining fingers and, as such, must be given special attention. The CMC joint of the thumb can perform two different types of movements: flexion/extension and abduction/adduction. In the first case, the angles measured between the longitudinal axis of the radius and the first metacarpal shall reach 0°-15° and 0°-20° in flexion and extension, respectively. Note that flexion is the movement of the thumb towards the palm, and extension is the opposite movement. The thumb abduction measurement is performed based on the angle achieved between the first and second metacarpals. The value in the resting state is in the range of 15°-20°, so when the offset is removed, the thumb abduction movement must reach 70° [26]. These two movements can be performed together allowing the opposition/reposition of the thumb toward the fifth finger [6].

The remaining joints of the thumb, MCP and IP joints, have similar characteristics to the other fingers since they only allow the flexion/extension movement. At the MCP joint level the normal value range is 0°-80°, while in the IP joint, the range is lowered to 0°-60°. In some cases, people can extend the IP joint up to 45°. The main movements of the thumb are shown in figure 2.6 [27].

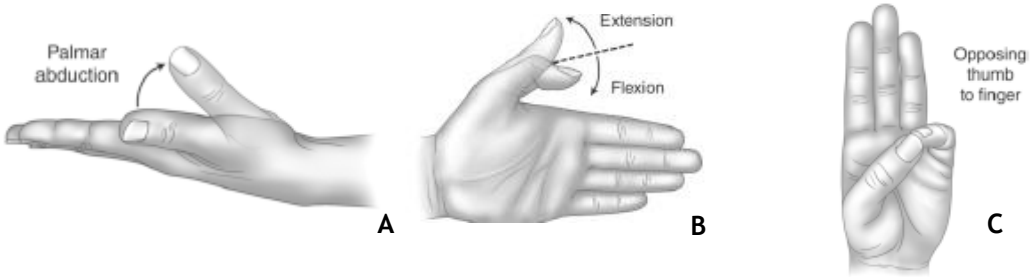

Figure 2.6 - Main movements of the thumb. The movement of abduction/adduction in A, flexion/extension in B and opposition/reposition in C [5].

Finally, in the wrist, there are 3 different movements of prominent role: flexion/extension, pronation/supination, and radial/ulnar deviation, as shown in figure 2.7. The normal ranges for flexion and extension of the wrist are 0°-80° and 0°-70°, respectively. The pronation/supination presents a normal range of 0°-80°/90° for each side concerning the

neutral position when only the position of the hand moves. The radial or ulnar deviation is calculated with the wrist in neutral position and the forearm in pronation, i.e., palmar zone down. Here, the normal ranges are 0°-20° for radial deviation and 0°-30° for ulnar deviation [5].

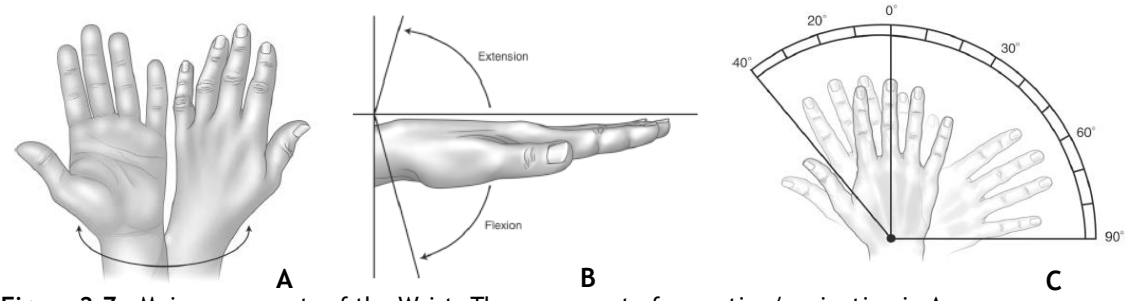

Figure 2.7 - Main movements of the Wrist. The movement of pronation/supination in A, flexion/extension in B and radial/ulnar deviation in C [5].

In addition to this evaluation, the motor functions of the hand are usually analyzed, especially in muscle/tendon injuries and peripheral or central nerve lesions. Muscle strength is commonly assessed according to the Medical Research Council scale [5]. This scale has 5 levels that evaluate the force from no movement observed until the normal contraction of the muscle against full resistance [28].

The movements hitherto referred in this subsection can also be evaluated regarding the strength. Standardly, the strength of each movement in each finger is individually assessed through the ability of these to contract normally against a resistance. After the examination, by crossing the extracted information with the medical knowledge, the conclusions about the affected muscles, tendons or nerves can be drawn [5].

In these strength tests, there are some essential considerations in some movements that must be taken into account. During adduction, it is recommended a trial in which the patient tries to hold a sheet of paper between the extended and adducted fingers. Afterward, the ease with which the doctor removes the sheet between the fingers of the patient can be evaluated if the first step has been successfully performed. The same happens during the thumb adduction in which the patient is instructed to hold a paper between the ulnar side of the thumb and radial side of the second finger in extended position. In the opposition of the thumb, it is evaluated the strength with which it touches the pulp of the fifth finger [5].

Finally, there are more complex tests with a more functional point of view, where pinch and grip strength are evaluated. In the pinch function, the patient should be able to perform an "o" shape with the thumb and the second finger. Although it is possible to perform strength tests, if the patient cannot achieve this first test it is an indication of muscle problems. There are 3 types of pinch that can be segmented into: lateral or key, tip-to-tip or three-fingered or three-point chuck [5].

Whereas in the lateral pinch it is evaluated the thumb force against the proximal phalanx of the second finger, in the tip-to-tip pinch it is assessed the thumb strength against the tip of the second finger and the three-fingered pinch strength is evaluated for the first three fingers held in a central point, as shown in figure 2.8. Moreover, the total strength of the hand while the patient grabs an object or the distance between the tip of the fingers during flexion and the distal palm crease can be extremely useful metrics for the physician [5].

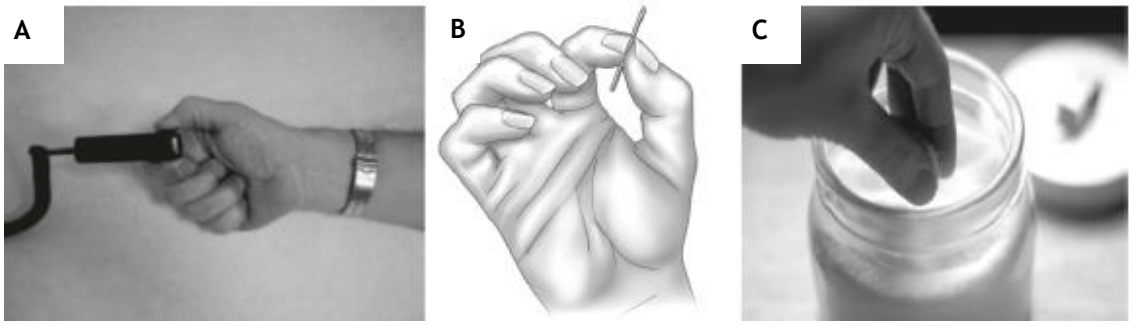

Figure 2.8 - Main pinch movements. In this figure are illustrated lateral pinch in A, tip-to-tip pinch in B and three-fingered pinch in C [5].

In conclusion, this study allows us to obtain metrics with clinical interest that when allied to the technology can evaluate parameters such as joint displacement over time, the range of motion, linear and angular velocities, linear accelerations, time and efficiency of the task. Subsequently, this data allows us to obtain more complex measurements as smoothness and coordination of the movements [29].

Now that all the kinematics and the main points of the physical examinations have been discriminated, the main pathologies will be highlighted.

2.2.2 -Associated Pathologies

The pathologies in the hand and wrist can be due to injuries in its own complex structure, such as in bones, ligaments, muscles, tendons, nerves and circulatory system. On the other hand, a decrease in movement and strength can be caused by pathologies in other independent systems of organs.

When adopting a more peripheral view, it can be concluded that the hand and wrist are the most active and intrinsic part of the upper extremity, hence being more vulnerable to injuries and functional difficulties [3]. This topic intends to reflect the importance of devices for diagnosis and evaluation of the hand movements and strength since these are essential in many pathologies with considerable prevalence in the population.

2.2.2.1 - Arthritis

According to the Arthritis Foundation, this disease with over 100 different types was diagnosed in about 52.5 million adults in the US, from which approximately 43% had arthritis-attributable activity limitation between 2010 and 2012. It is also estimated that by 2040, the number of American adults with this diagnosed disease will exceed 78.4 million. This high percentage in active adults is projected in 172 million days of missed work due to arthritis and other rheumatic conditions. In 2013, the total economic impact of medical costs and earning losses were accounted in $304 billion only in America [30].

This pathology without particular causes began with symptoms such as swelling, pain, stiffness and decreased range of motion. When not adequately monitored, it can damage the joint cartilage responsible for smoothness, acting as a gliding surface for joint motion between bones, as well as the bones themselves. Over time, these joints become loose, unstable, painful and lose their mobility. In more severe situations, it is expected chronic pain, inability to do daily activities, making it difficult to walk or climb stairs. At this stage, there is a high probability of permanent joint injuries [31].

The two most influential types of arthritis are osteoarthritis (OA) and rheumatoid arthritis (RA). While in osteoarthritis there is rupture of the cartilage, in rheumatoid arthritis the cartilage is progressively eroded by an internal inflammation originated by the immune system itself, in people with a greater genetic predisposition. Regarding the results of the impairments in hand, osteoarthritis (OA) involves in many cases the CMC joint of the thumb (15% of adults older than 30 years), and Heberden's and Bouchard's nodes in the DIP and PIP joints, respectively. On the other hand, rheumatoid arthritis (RA) causes impairments more frequently during ulnar deviation and subluxation in the MCP joint. In the PIP and DIP joint, the main injuries include swan neck or boutonniere deformities, which affect an estimated 30.8 and 1.5 million adults in the US, respectively [31, 32]. In addition, these conditions are linked to increased rates of comorbidity (e.g., obesity, diabetes, heart disease and depression) [30].

2.2.2.2 - **Traumatic Brain Injury (TBI)**

According to the National Center for Injury Prevention and Control in the US, this is a problem that contributes to about 30% of all injury deaths. Specifically, in 2013 the TBI-related visits number of the emergency department reached 2.8 million. Traumatic brain injury (TBI) is caused by a collision, shock or blow to the head that disrupts normal brain function. In milder cases, this pathology is classified as a contusion. Patients usually have some impairments in thinking, memory, movement, sensation, and emotional changes over an indeterminate period or even for the rest of their lives [33].

2.2.2.3 - **Stroke**

Classified as the fifth disease with the highest mortality in the US, this disease reaches about 800 000 people each year with ¾ of first occurrences. The American Stroke Association considers the stroke as the leading preventable cause of long-term disability [34]. In particular, Ilaria Carpinella et al. refers that approximately 60% of stroke survivors experience hand dysfunction that leads to limitations of daily activities [35].

This pathology occurs when the blood flow to an area of the brain is interrupted. In fact, when brain cells are deprived of oxygen, they begin to decease, damaging the zones of the brains such as the ones responsible by memory and muscular control. The way this pathology affects the patient depends essentially on the area where it occurred and how much the brain is damaged. Some of the people recover entirely from a stroke, but more than ⅔ remain with some type of disability. This disorder is classified as hemorrhagic when an aneurysm bursts or the weakened blood vessel leaks in the intracerebral and subarachnoid sites, and as ischemic when a blood vessel carrying blood to the brain is blocked by a blood clot. This last takes place in 87% of cases [36]. For most occurrences, a post-stroke recovery of motor function involves relearning motor skills mediated by neuroplasticity [37].

2.2.2.4 - **Parkinson’s Disease (PD)**

This pathology reaches about one million Americans and every year 60 000 new cases are diagnosed, according to the statistical data from Parkinson’s Foundation [38]. The Parkinson’s disease is an idiopathic neurodegenerative disease that causes the death of brain cells which produce dopamine. In the brain this compound works as a neurotransmitter, i.e., a chemical released by neurons, to send signals to neighbouring cells of the same type. Although there is

no standard methodology for diagnosis, medical experts search for shaking or tremor, bradykinesia, i.e., slowness of movement, rigidity on the arms, wrist, legs or trunk and postural instability [39].

2.2.2.5 - Systemic sclerosis (SSc)

A study conducted by Maureen D. Mayes et al. concludes an estimated prevalence of 275 cases per million US adults and an annual incidence of new cases in 19 cases per million adults [40]. This pathology, also recognized as scleroderma, is a chronic connective disease, especially involving fibrotic changes in the skin, blood vessels, internal organs, skeleton muscles, tendons, and joints. Focusing on the hand, these fibrotic changes often reduce the flexion of the MCP joint, the extension of the PIP joint, and the general thumb movements. From a global perspective, finger flexion and extension, grip strength and dexterity are the main reductions diagnosed [31]. The origin of this disease is still unknown as well as an effective treatment [40].

2.2.2.6 - Spinal Cord Injury (SCI)

According to the National Spinal Cord Statistical Center, there are approximately 54 cases per million people in the US and about 17 500 new cases each year [41]. The spinal cord is an extension of the central nervous system allocated inside the spine, and its main function is to carry the signals from the brain to all parts of the body and vice versa. When it is damaged as a result of trauma, disease or degeneration, the nerve impulses do not reach their target, which leads to motor and sensory loss (temporary or permanent) functions, and in more severe cases it can lead to paralysis [42].

This medically complex and life-disrupting condition affects people differently depending on the location of the lesion and its intensity. Specifically, injuries in the C6 and C7 vertebrae cause loss of strength and ROM problems in the hand and wrist [43].

2.2.2.7 - Illnesses with side effects on hand

Unlike the diseases previously explained, some illnesses in their advanced stage can be responsible for some type of disorder located in the hand and the wrist. For instance, chronic renal failure is intrinsically linked to the process of haemodialysis, since it is a process that when used over long periods of time begins to cause musculoskeletal disorders and some functional limitations. Its main symptoms are carpal tunnel syndrome, juxta-articular bone cysts or erosions, and destructive spondyloarthropathy [4].

The effect of diabetes type II and its metabolic disorders was also studied in a similar way. It is estimated that 50% of people with this pathology present disorders in the connective tissues, causing musculoskeletal impairments. The associated symptoms, despite lower intensity, include limited joint mobility, stiff hand syndrome, carpal tunnel syndrome, among others [31].

2.2.2.8 - Work-related

The US Department of Labor defines work-related musculoskeletal disorders (WMSDs) as all injuries in the joints, cartilage, muscles, tendons, nerves and spinal discs associated with exposure to risk factors in the workplace. These are overwhelmingly related to the

performance of a repetitive and forceful hand-intensive task. Analysing the statistical data on occupational illnesses, it can be noticed that approximately 65% are associated with repeated trauma. More concrete cases of occupational illnesses can be a consequence of incorrect hand and wrist postures, low temperatures and constant vibration. The most common cases reveal irritations and inflammations in the tendons (tendinitis) and ligaments, which in the most severe cases lead to their rupture, causing pain, discomfort, and loss of function [44].

The WMSDs of the hand and wrist are in most cases the most significant cause of absenteeism at work, corresponding to a lower productivity at work when compared to the same type of problems in other regions of the body. In the general context, this type of lesions constitutes 28% of the total injuries that occur in the hand [44, 45].

In conclusion, these types of injuries may lead to the need for rehabilitation, where quantifications of their evolutions over time can be essential to progress.

2.2.3 - Common Devices in Medicine

Nowadays, there are already some devices in the hospitals that are daily used in this type of pathologies along with Duruöz Hand Index (DHI) and other types of questionnaires [4]. These devices have specific functions to improve rehabilitation and medical diagnosis. The rehabilitation devices, also classified as active, are designed to re-impose movements in patients with reduced mobility, empowering them to live an active life. On the other hand, the diagnostic devices classified as passive have more sensorial features and essentially evaluate the strength and kinematic capacity of patients [46]. These diagnostic devices have an appreciable added function since they can be used throughout the treatment as a quantifier of improvement and treatment efficiency for the patient. Within the scope of this dissertation, only the diagnostic tools will be highlighted, since this is its main focus.

Initiating the discussion with the kinematic evaluation, it is usual in clinical practice the use of goniometers. These devices shown in figure 2.9 (A) are already considered obsolete and of low technological level. In addition, they allow the measurement of the range of motion of the joints individually, which takes too long when considering all the joints to evaluate. Nowadays, the goniometers have undergone some updates, reason why it is possible to see some electrogoniometers similar to figure 2.9 (B). Nevertheless, this technology continues to have some problems regarding the difficulty of aligning with the joints, the impossibility of measuring all DoFs at the same time in the same joint and its associated costs [47]. However, there are already some variations of the traditional goniometer as is the case of the pollexograph in figure 2.9 (C), specifically designed to measure the palmar abduction of the thumb [48].

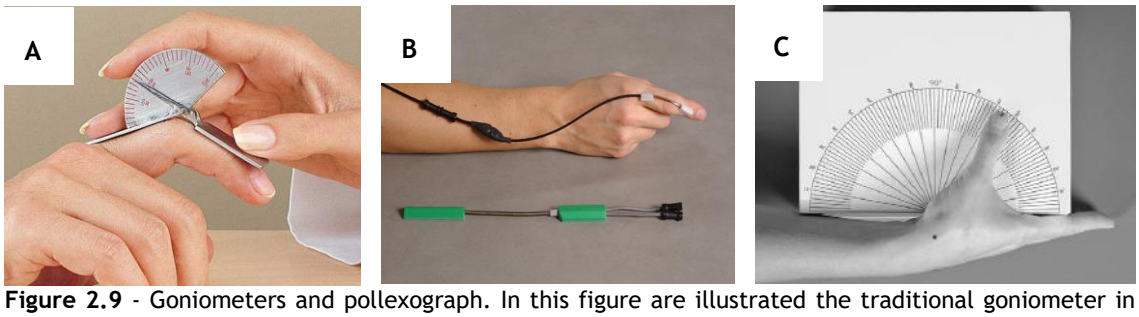

Figure 2.9 - Goniometers and pollexograph. In this figure are illustrated the traditional goniometer in A, the electrogoniometer in B and pollexograph in C [47–49].

On the other hand, the evaluation of the strength is mainly performed with low objective metrics as already mentioned above and there are few devices in this area. Traditionally, the physician begins by evaluating with naked eye the ability of the patient to pick up and hold objects. At this stage, the physician may also create some resistance to the movements of the patient, assessing the ability to counteract the opposing force [5].

Devices such as the pinchmeters and the Jamar dynamometers can be found in some medical centres. Whereas the pinchmeter evaluates the maximum strength of the patient during the pinch, the Jamar dynamometer evaluates the maximum grasp strength in the whole hand [5]. These devices can be found in figure 2.10.

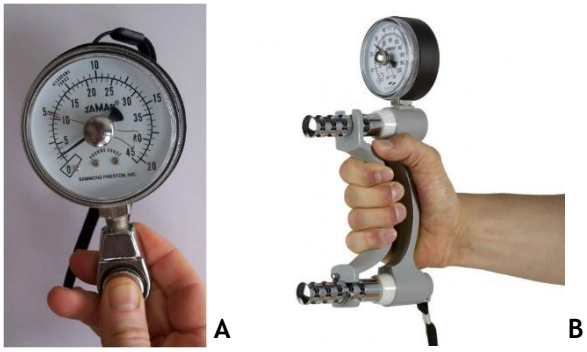

Figure 2.10 - Pinchmeter and Jamar dynamometer. In this figure are illustrated the pinchmeter in A, the Jamar dynamometer in B [50, 51].

With this description of the devices found in clinical practice, the need for technological development in this branch is emphasized in order to make the most accurate and precise quantification in a quick and trivial way.

2.2.4 - Alternative Devices on the Market or being Developed

Over the years technological advancement has enabled computers to become capable of communicating effortlessly with a variety of hardware. Merging these tools with software developed specifically for these cases, a myriad of solutions emerged with the goal of updating or resolving the current gaps. In hand assessment and rehabilitation, reliable methodologies or devices capable of sensorial and passive tracking have emerged in recent decades.

Most recent advances concerning this topic are concentrated in wearable technology described in detail in the next section. This technology allows the integration of sensing components in garments, creating a new generation of sensors called "smart garments" [52].

Throughout this section, it will be portrayed the different *modus operandi* of devices found in the market or in development, especially datagloves (an input device for human-computer interaction worn like a glove). Nevertheless, there is the need to highlight other technologies that have the capacity to extract similar parameters, such as the camera-based systems.

2.2.4.1 - **Datagloves based on flexible optical sensors**

This is one of the most mature methodologies in angular displacement. It uses a flexible reflector tube capable of conducting light between the two ends, reassembling a more straightforward operating principle than the others, since it only needs a light source and a

photosensitive detector at each end. As the curvature occurs, the sensor detects variations in the intensity and wavelength of the light, which is directly proportional to the increase of the measured angle [46, 53].

This is a low-cost, simple, electronic-resistant and small-sized technology that was at the base of the first instrumented glove (Sayre Glove in 1977) illustrated in figure 2.11 (A) [54]. Nowadays there are instrumented gloves with these characteristics such as the 5DT DataGloves with several models in optical fiber. For instance, this company produces the DataGlove 14 ultra (figure 2.11 (B)) incorporated by 14 sensors capable of measuring the flexion/extension of the MCP and PIP joints on each finger, as well as its abduction/adduction with the exception of the thumb where only flexion/extension of the joints are measured. Although there are some RA studies with this glove, it is primarily sold as a capturing solution for animation and virtual reality [55–57].

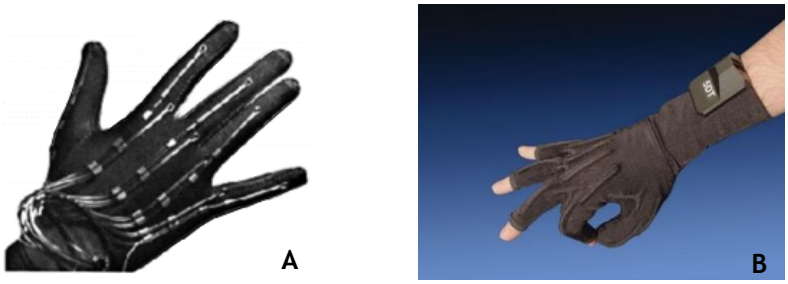

Figure 2.11 - Datagloves based on flexible optical sensors. In this figure are illustrated the Sayre Glove in A and the 5DT Data Glove 14 Utra in B [55, 58].

2.2.4.2 - Datagloves based on flex sensors

In addition to optical fiber sensors, the use of resistive bending sensors is also very intrinsic in this type of technology [59]. More precisely, the sensors are generally structured by conductive ink-based strips containing carbon or silver particles mixed into a pigmented medium. Its operation principle involves changing (increasing in most cases) the resistance as the deflection increases in one direction [60].

These flexible sensors are nowadays the thinnest, lightest, most robust and cost-effective variable resistor available with more than sufficient life cycles for most applications. On the other hand, some studies indicate as a disadvantage the saturation of the sensor from the 100°, for which it becomes imperative to have a sensor of this type in each joint [61, 62].

This was the working principle used by PowerGlove (figure 2.12 (A)) launched in 1989 for Nintendo Entertainment System with a futuristic intention in the world of games but without success at the time [63]. Currently on the market, the most used devices are the CyberGlove III model from CyberGlove Systems and Manus VR glove. Describing the CyberGLove III, it has 18 or 22 sensors (3 flexion sensors per finger, 4 abduction sensors, the palm-arch sensor, and sensors to measure wrist flexion and abduction in the case of 22 sensors). The Manus VR glove has 12 sensors in total (10 sensors to measure the MCP and PIP/IP joints and 2 IMUs to measure the hand and wrist orientation). These gloves are used in a wide variety of real-world applications, including virtual reality, animation, digital prototype evaluation, biomechanics, high-performance hand-measurement, and real-time motion capture. Both devices are represented in figure 2.12 (B and C) [64, 65].

In development, there are gloves capable of translating sign language into text from these sensors [68, 69]. In addition to the above-mentioned sensors, a new kind of sensors have been created that use conductive liquid metal injected in a soft chamber. The resistance of the sensor changes according to the deformation of external forces. Although they have some limitations, these sensors easily adapt to the definition of wearable devices being already tested as an alternative to flex sensors [59].

Figure 2.12 - Datagloves based on flexible flex sensors (I). In this figure are illustrated the Power Glove in A, the CyberGLove III in B and Manus VR glove in C [64, 66, 67].

With the same ideals, sensors with capacitive materials can also be used. For instance, StretchSense manufactures elastic strips of capacitive material constructed from a laminar polymeric structure. These sensors have the ability to measure the angular displacement of the joints since when movement is performed, the straps adjacent to the fingers deform by varying the sensor capacity. The bending of the finger reduces the distance between the two conductive materials separated by a dielectric material, which in its turn increases the capacity of the material. In this way, it is possible to have values inversely proportional to the associated angle. More recently, this company has already presented a complete prototype in addition to the sensors, which is represented in figure 2.13 [68, 69].

This configuration allows an alternative to previous methods, creating a more stable and better repeatable device. On the other hand, these sensors have an unpredictable resistance and suffer minimum variations in the value of their capacity. Nevertheless, some authors such as Zhong Shen et al. claim that for wider and further applications, bending or strain sensors are still in need of flexibility, comfort and accuracy as well as low cost and non-toxicity [59, 68, 69].

Figure 2.13 - Datagloves based on flexible flex sensors (II). In this figure is illustrated the StretchSense DataGlove [69].

2.2.4.3 - Datagloves based on inertial tracking

The gloves with inertial systems consist of IMUs (inertial measurements units) combining accelerometers, gyroscopes and most of the time magnetometers. Starting with the accelerometer, it is a device used to measure the acceleration of a system in relation to another in a free fall. As so, accelerometers are used to determine the direction of the local vertical by sensing acceleration due to gravity. Furthermore, accelerometers are able to calculate linear motion from the specific force, i.e., the non-gravitational force per unit mass (m/s^2). It has as main drawback the high sensitivity to vibration [70].

Rate gyroscopes measure angular velocity ω ($rad.s^{-1}$), around one axis, without an external reference and if integrated over time, can provide the change in angle (or orientation) with respect to an initially known orientation. Although these sensors allow calculating the pitch, roll and yaw rotational, the continuous integration of sensor data tends to drift over time because gyroscopes sense angular changes but do not have a fixed frame of reference. Finally, the magnetometers are able to sense the direction of the earth magnetic field like a compass that provides stability in the horizontal plane. Its main disadvantage is its sensitivity to magnetic interference [70].

The data from these complementary sensors as a set allow to eliminate the drift and get the correct position and orientation of an object in three-dimensional space. This is the concept of sensor fusion, which is a process by which data from several different sensors are "fused" to compute something more than it could be determined by any sensor alone. Also, it can improve accuracy and reliability [70, 71]. Currently, these devices have reduced size and cost, mainly due to the increase in MEMS technology (Micro Electrical Mechanical Systems). This technology is commonly implemented in textile clothing without causing inconvenience to the user [72].

The set of sensors described can be found in the datagloves market, in particular the IGS Cobra Glove from Synertial that is available in the configuration of 7, 12 and 15 IMUs with 9DoFs each. Figure 2.14 (A) shows the extremes of these configurations. These are distinguished from the rest of the market by their ability to record the motion between the fingers (adduction/abduction), measure and record palm flex, and thumb and fingertip touching. Additionally, figure 2.14 (B) illustrates Synertial's Calibration Pipeline still with pending patent but with the objective of obtaining an exact initial calibration of the IMU system [73, 74].

Figure 2.14 - Datagloves based on inertial tracking. In this figure are illustrated the IGS Cobra Glove from Synertial with the respective sensors location in A and Synertial's Calibration Pipeline in B [73, 74].

Moreover, some of this type of devices are still under development as exemplified by the device developed by Henk G Kortier et al. shown in figure 2.15 (A). This device deploys in each string three triaxial gyroscope and accelerometer pairs, one for each finger/thumb segment. In addition, the triaxial magnetometer is placed on the fingertip and on the back of the hand. Their research showed that inertial and magnetic sensors are of interest for the human hand and finger kinematics assessment, concluding with good static accuracy, dynamic range and repeatability. These sets of sensors allowed an estimation of multi-degree of freedom joint movements with a low-cost solution [72].

Subsequently dubbed as PowerGlove, its main focuses are in the medical field, specifically in the evaluation of movements and follow-up of rehabilitation. The same authors are now in the testing phase, where they look for possible applications of their device in healthy aging and Parkinson's disease monitoring. The long-term goal is to apply its device in PD patients during DBS-surgery, as an optimizer of the evaluation of the state of the patient while new DBS-stimulation protocols are being tested [75].

Another work by Brendan O'Flynn et al. called "IMU Smart Glove" is a dataglove that also measures the range of motion of the hand quantitatively (figure 2.15 (B)). Its measurements are performed from 16 IMUs with 9DoFs each, which when synchronized measure all movements originated in the MCP, PIP and DIP (or IP to the thumb) joints of the fingers and thumb in degrees. Its main focus is to assist physicians with accurate and easy-to-acquire measures in the evaluation of motion in patients with Rheumatoid Arthritis [76].

As already mentioned, diseases affect not only the hand kinematics but also its strength. With this in mind, Pei-Chi Hsiao et al. proposed a dataglove embedded with seventeen 9-axis inertial sensors and five force sensitive resistors, as shown in figure 2.15 (C). This dataglove has its IMUs in a similar position to the previous prototype, however it has 5 force sensors attached to the fingertips to measure pressure when the patient grabs an object [77].

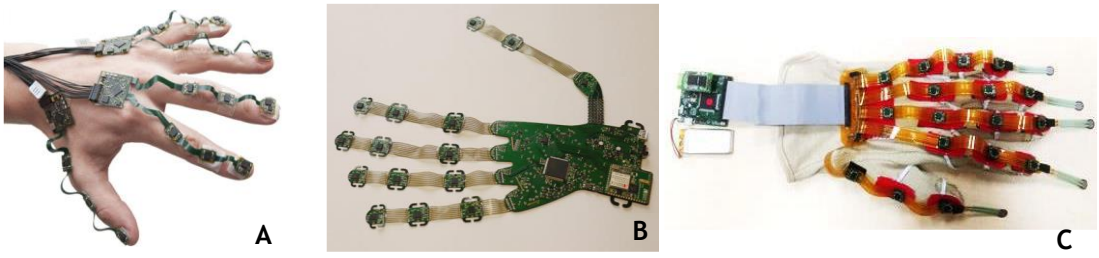

Figure 2.15 - Datagloves based on inertial tracking under development. In this figure are illustrated the PowerGlove in A, the IMU Smart Glove in B and the dataglove proposed by Pei-Chi Hsiao et al. in C [72, 76, 77].

2.2.4.4 - Magnetic Tracking

In general, magnetic tracking uses a source element radiating a magnetic field and a small sensor that reports its position and orientation with respect to the source [53]. The sensors with the most impact on this market belong to Polhemus (figure 2.16) and are able to obtain 6 DoFs by calculating the coordinates of the person or object on the x, y, and z-axes in space, as well as their orientation from yaw, pitch and roll. Motion tracking is performed with a source that acts as a transmitter, which emits an electromagnetic dipole field, making it possible to calculate the position and orientation of the tracker components relative to the source [78, 79].

The advantages of these sensors compared to the rest are the best signal-to-noise ratios and multiple tracking systems in the same environment, without cross-talk interference. These sensors are still easily scalable and only need to add additional tracker components to the environment to be detected. In addition, they do not have issues with drifts (error in tracking output over time), which are very common in inertial technologies. The main drawback is that metal objects can interfere and distort the magnetic field [53, 78].

Figure 2.16 - Magnetic tracking sensors. In this figure can be seen the Polhemus sensors [84].

2.2.4.5 - Optical Tracking

In this topic, it will be approached two types of camera-based tracking: video processing and marker systems. In the first place, the video processing algorithms are commonly based on hand contours from cameras such as Kinect or Xtion, which in addition to the image also acquire the depth map, also known as RGB-D cameras [72, 80].

The software developed by CVRL, ICS and FORTH allows 3D tracking of the position, orientation and articulation of the hand, estimating a total of 26 DoFs without the need for calibration. The 2D and 3D segmentation of the hand is performed from the skin color followed by the depth detection, respectively. Then, a 3D model of the hand is made from primitive geometric objects. Each pose is represented by a vector of 27 parameters, which are sufficient to minimize the discrepancy between the model and the observation. After some optimization algorithms, the model is represented as the output that corresponds to the frame (figure 2.17). The tracking is then performed for each frame over time [80].

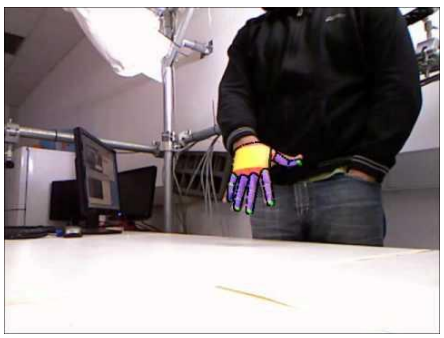

Figure 2.17 - 3D hand tracking software developed by CVRL, ICS and FORTH. In this figure can be seen the output model [80].

At last, marker systems are considered as actives when the position is triangulated by LEDs simultaneously or multiple LEDs with software to identify them by their relative positions. On the other hand, they are considered as passives when markers are coated with a retroreflective material to reflect the light that is generated near the camera lens [81]. For instance, ART produces an active finger tracking (figure 2.18) with 3 or 5 finger marker

versions. The complete system along with the cameras is capable to calculate the position and orientation of the posterior face of the hand, as well as the angles between the phalanges and their lengths from tracked markers and empirical data. This was designed in view of augmented and virtual reality [82].

Figure 2.18 - ART active finger tracking device. In this figure is illustrated the 5 fingers version [82].

ART and Vicon produce cameras and passive markers similar to those in figure 2.19. These systems allow more freedom in the position of the markers, which propelled its widespread use in biomechanics and sports, but also in gait analysis, rehabilitation and in studies related to posture, balance and motor control. In particular, Vicon's optical motion capture systems have already been classified as Medical Devices, certified by ISO 13485 and ISO 9001 [83].

Some studies have already been carried out in hand kinematics evaluation based on markers, such as the research conducted by Jéssica de Abreu et al., measuring the flexion/extension in the PIP and DIP joint with 8 infrared cameras and two versions of 16 and 23 markers in the hand [84].

Figure 2.19 - Example of a Vicon passive motion capture system. The figure illustrates a study carried out by MDW (University of Music and Performing Arts Vienna), where the passive markers are found in A, the configuration of infrared cameras in B and the respective output in C [85].

In conclusion, camera-based systems can be an alternative to datagloves since they allow easier assembly of a 3D environment. Furthermore, video processing may require extremely complex algorithms at the development level and sometimes do not translate into precise and important information as the sensors previously referred. The marker systems can sometimes be cumbersome to deploy, and the equipment is too expensive when compared to the price of the sensors needed to constitute datagloves. The major drawback of camera-based systems occurs when there is occlusion of the hand-segments or markers, which results in a non-observable situation, inducing a poor estimate of the hand pose. This is a disadvantage that does not exist in datagloves [53]. An interesting aspect would be the performance comparison between the different devices/systems described. However, given the diversity in system architectures there is a notable unavailability of the accuracy values in a standardized way provided by companies and developers, which makes a structured comparison unfeasible.

2.3 - Project Fundamentals

This master thesis focuses on two theoretical fundamentals that provide insight for the following steps: the architecture of wearable systems and the theory behind inertial measurement units. In a first approach, the generic architecture of wearable systems will be described, as well as some considerations according to the market trends where these systems have been developed.

The second approach intends to describe the theory behind inertial measurement units. This topic aims to understand the *modus operandi* of these sensors and some deliberations regarding the achievement of objective metrics, which are essential for clinical evaluation. In addition, these will be the sensors that will integrate the prototype, making it possible to infer the movements of the wrist and its rigidity through the correlated data between IMUs.

2.3.1 -Wearable Systems

Smart Wearable Systems (SWS) are defined as mobile electronic devices that can be unobtrusively embedded in the outfit of the user as part of the clothing or an accessory. In contrast to the remaining systems with the same purposes, they must have very little or no interference to user activity [86]. This new idea of a simplistic interface between the user and technology arises inheriting ideas from Internet of Things (IoT). This term currently in vogue began a journey for a new era of smart and portable devices integrating various sensors, microcontrollers and all sorts of communication protocols, establishing the foundation for futuristic communication standard (human-things interaction) [87].

Supported by recent technological advances in micro and nanotechnologies, the continuous advances in SWS will progressively change the landscape of healthcare creating the next-generation of healthcare systems. These changes allow a constant and individual status monitoring of the patients or users for clinical or autonomous applications [87].

With this background emerges the Wearable Health Systems (WHS) improving the concept of Personal Health Systems (PHS) introduced in the late 90s. The interest in this concept initially arose in favour of the need to extend health services out of the hospital and monitor patients over extended periods of time, but quickly became vulgarized by IT companies, launching to the market devices that promote individual adoption of healthy lifestyles and self-care [88].

This section describes the generic WHS architecture, segmenting in tiers by its functionalities. Then it will be given importance to the market that these systems entail and its growth prospects. Finally, in the form of a conclusion, a small revision will be made to its insertion in the current health systems and in the daily activity of the users.

2.3.1.1 - **Generic System Architecture**

The WHS follow a generic hierarchical architecture capable of representing all systems, differing for each target application the combinations and types of communications implemented. In addition, not all wearable devices need to constitute a large-scale model composed by all tiers [89, 90]. Therefore, the WHS architecture is essentially segmented into 3 tiers, as shown in figure 2.20.

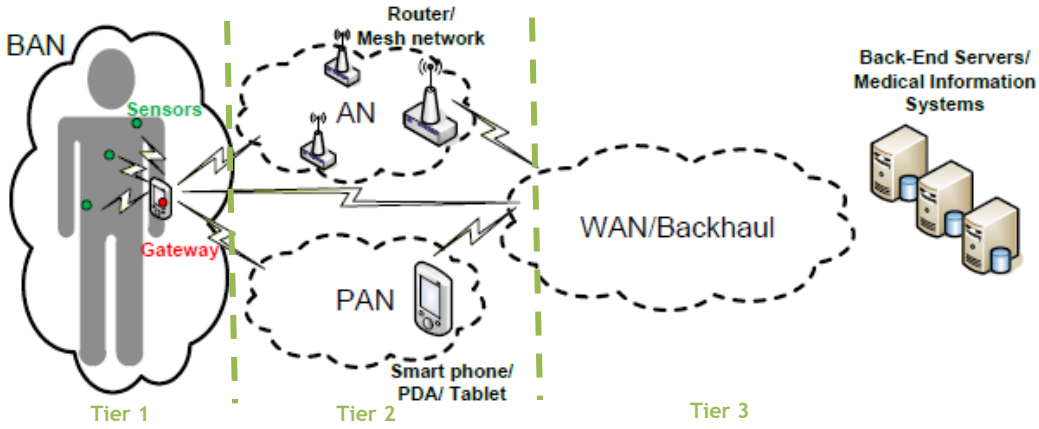

Figure 2.20 - Generic System Architecture for WHMS. Adapted from [89].

Tier 1: Patient/user and BAN

The first tier is made by the patient/user and the BAN (Body Area Network). As mentioned above, the usufruct of these systems is performed not only by patients in hospital situations, but also by regular users interested in self-healthcare that intend to maintain a constant monitoring of their vital signs and physical activity. In recent years it has been found that the increase in consumption by regular users is largely due to a more active and high-performance physical practice. These users seek to track the physiological and kinematic data, trying to obtain alternatives or indications of the parameters that they must improve to achieve better results until reaching its own limits. On the other hand, the application of these devices in a clinical/hospital environment is seen as an alternative to the increase of health care costs, whether in the hospital or domestic environment, especially in cases of continuous monitoring as patients with chronic diseases or elderly people [91].

Marie Chan et al. reports a set of diseases, handicaps or disabilities that may already be monitored, among which: cardiovascular diseases, diabetes mellitus, renal diseases, respiratory disease, cancer, posture and motion control, neurological disorders and brain stimulation, rehabilitation, Parkinson's disease, stress, among others. Many of these are reserved only for the clinical environment, and only the less specific parameters such as stress, posture and motion control are accessible to the common market. These devices play an important role in the assessment and rehabilitation, since they have the capacity to store motion and muscle activity patterns using sensor-equipped garments, benefiting from the comfort and unrestrictive movement originated in rigid and uncomfortable platforms [91].

The Body Area Network (BAN) is defined as the set of sensors implanted in the body, placed on the body in fixed positions or carried by the person in clothes pockets, by hand or in a bag. This assembly is generally connected by wires inherent to the garment to a local collector, also called BAN coordinator (BANC). This device allows centralizing all the data of the sensors, collecting them for future eventualities [92].

In situations of higher distance in the sensor-BANC relationship, the need for wireless communication becomes imperative. For this, the sensor nodes must have communication protocols such as Bluetooth, Wi-Fi (IEEE 802.11), and Zigbee that operates according to IEEE 802.15.4, which has become a standard for robust, low cost and low power communication [89]. More recently, the ability to make the body of the patient into biological channels where it can be used as the transmitter of electrostatic fields is being studied, but the limitation generated by the low transmission of the data has raised some issues given the amount of data transmitted [93, 94].

Momentarily prior to the input of the raw data in the BANC, signal processing generally takes place including possible amplifications, filtering and finally the analog to digital signal conversion using A/D converters. Note that this set of sensors and coordinator must have low-power consumption, even when they have wireless communications infrastructure to support wide coverage and mobility [90, 93]. Also, it should be noted that BANCs may have processing capacity, but the most correct and commonly done is to leave the second and third tiers in charge due to their minimal computing power when compared to the top tier devices [91].

BANCs can also be segmented into offline and online applications. In offline applications, BANCs must be able to store data on SD cards or similar structures. Subsequently, these data in a compatible format with other devices should allow analyses on the personal computer or by the physician when downloaded to the medical information platform. On the other hand, in online applications BANCs must have Wi-Fi to communicate directly with information systems or other communications technologies, such as Bluetooth, Zigbee or radio-frequency identification (RFID) for communication with other external devices as will be explained in detail in the next tier [89].

Tier 2: AN and PAN gateways

This layer integrates technologies that have direct contact with the BAN when there is some type of communication, segmenting the gateways into AN where routers and mesh networks are included, and personal area network (PAN). Communication with the AN allows direct connection of the BANs to the network for sending data ordinarily using the Wi-Fi. The wireless mesh network is based on Wi-Fi or others with IEEE 802.15 compliant specifications. However, this gateway has applications in restricted and controlled areas such as hospitals. This communication allows simplified communication with the back-end system through the gateway as will be explained in tier 3 [89].

On the other hand, PAN allows the connection between BAN and smartphones, tablets and personal or clinical computers, allowing a greater variety of available communications. In this context, communications such as Bluetooth, Zigbee or RFID are the most used. The combination of these different types can also be found in WHS. In practice, Bluetooth is one of the most widely used communications technologies for PAN, since it provides reasonably high bandwidth (able to aggregate the traffic coming from the BAN) and is widely implemented in commercial devices, such as smartphones, tablets and laptops [89].

These PAN devices enable fast data processing for more efficient feedback, and data transmission between wearables and back-end servers when desired. In some situations, it is possible to leave the processing in charge of the “cloud” in tier 3, allowing a greater battery saving of the smart device [95]. In the literature there are some cases where by choice or by necessity, implementation merges the PANs and BANCs, i.e., smart devices directly receive the data from the sensors [89, 91, 95].

Tier 3: WAN/Backhaul communication

The third and last layer also known as back-end network tier is considered the long distance communication level composed by the WAN/Backhaul and subsequently by the servers or medical information systems [96]. The Wi-Fi, as well as cellular technologies (e.g., GSM, GPRS, GPRS, 3G and more recently 4G) and broadband wired technologies (e.g., ADSL, cable and more recently optical fiber) have been types of communication between this layer

and the previous one. In practice, the most widely used has been wireless communication [89, 97].

This layer has essentially two purposes. The first is intrinsically associated with telemedicine applications, promoting a remote monitoring and diagnosis of the health status of the patient or group of patients in and out of the hospital. This may still be able to trigger additional services such as emergencies and rapid interventions [95, 101]. The second purpose relates to big data support in this area, enabling "cloud" services and allowing to perform predominant data mining tasks in the medical environment: prediction, anomaly detection and applying machine or deep learning concepts [90, 93].

2.3.1.2 - **Market Opportunity**

Turning this concept into numbers and market trends, it is estimated an annual growth of 65% for smart wearable healthcare systems between the periods of 2014 to 2020, which corresponds to an increase in the global market size (devices, software and directly linked services) in the amount from $2 billion to $41 billion, respectively [98]. IDC Health Insights estimates that 70% of healthcare organizations worldwide will invest in consumer-facing technology including apps, wearables, remote monitoring and virtual care [99].

It is also estimated that 88% of physicians want their patients to monitor their health parameters at home, and that this technology can lower hospital costs by 16% over five years according to studies conducted by Orange Healthcare and Vitality Group [100, 101]. The consumer market also skyrocketed in the wristband and smartwatch market by around 684% in the first half of 2014 when compared to the same period in the previous year [102].

In conclusion, these devices bring a new perspective to medical applications, being able to address the needs of the care provider, monitoring, analyzing, diagnosing and alerting. These also have the advantage of promoting patient-centered care at lower cost delivered in the natural environments of the patient, thus giving rise to the concept of ubiquitous ambulatory monitoring [92, 103].

Wearable devices are indeed able to reduce the overall costs of prevention and long-term health monitoring. This technology along with mobile apps is increasingly being integrated with telemedicine and telehealth in an efficient manner, to structure the medical Internet of Things, making it a bet with excellent unsaturated market trends [104]. However, there are still some issues that need to be taken into account, mainly related to the difficulty of merging these systems with current healthcare systems. In addition to being difficult to change because of their size, a steady state is easily encountered for innovations when there is a need to change rather intrinsic methodologies or when physicians require to learn new technologies that they must subsequently apply to patients. Additionally, the massive processing capacity of systems to handle the huge pile of collected data in an efficient manner and certifications of data security and privacy should also be taken into account [103].

2.3.2 -Inertial Measurement Unit (Working Principles)

Inertial navigation is a technique in which the position and orientation of an object are determined through the data given by accelerometers and gyroscopes. The result is further calculated over time from the initial position and orientation of the object itself. This system

provides a distinct kinematic analysis when compared to navigation systems such as GPS or radar, since its position and orientation is not calculated from an external frame of reference. The inertial sensors have a very extensive range of use, from applications in airplanes to the automotive industry, smartphones, and more recently in the medical field [105].

Recalling the definition of the previous section, IMUs (inertial measurements units) are devices capable of measuring the specific force of the body, angular rate, and sometimes the magnetic field surrounding the body from the merge of accelerometers, gyroscopes and most of the time magnetometers. Generally, these sensors have triaxial readability, promoting a data acquisition with 9DoFs when grouped in the IMU [70].

Although there is a wide variety of operating principles for these sensors, currently the MEMS IMUs are the ones used in most cases since they allow great miniaturization and low costs. This technology created in the 90s enabled the development of new modern devices, but some constraints had to be taken into account. Only a few operating principles could be adopted given their need for miniaturization. These are the most relevant to this dissertation, so they will be addressed in this section [105].

2.3.2.1 - MEMS accelerometers

MEMS accelerometers are based on measuring the displacement of a proof mass as a result of acceleration based on a mechanical sensing element. In general, the proof mass is fixed to a mechanical suspension system with respect to a reference frame. Therefore, the inertial force due to acceleration or gravity will cause a deflection in the proof mass according to Newton's Second Law. Complementarily, the acceleration measurement can be calculated according to physical changes in displacement of the proof mass with respect to the reference frame [105, 107].

Currently, it is common to find three different linear accelerometers to measure the three-dimensional movement, but there are also triaxial accelerometers capable of measuring on all three axes simultaneously. Although there are several ways of measuring the displacement of proof mass, the most commonly used in MEMS are capacitors, piezoelectric crystals and piezoresistive materials [105, 106, 108].

Capacitive-based accelerometers measure the displacement of the proof mass capacitively. This proof mass is encapsulated between two electrodes and the differential capacitance is proportional to the motion of this between the two electrodes. Given its low power consumption, high output range and fast response to movements, this principle has been used in many applications related with mobile and portable systems, and consumer electronics. These are still DC-responsive enabling the measurement of constant accelerations such as gravity. On the other hand, the disadvantages centre on its far-flung triviality given its complex mechanism [107, 108].

In piezoelectric-based accelerometers are used crystal materials, which generate a voltage when subjected to mechanical stress. Although not relevant to accelerometers, these materials also have the opposite capability, i.e., when applied to an electric field they undergo deformation. Physically, when stress is applied the arrangement of the atoms is altered, releasing electrical charges between them. With this property, the sensing elements are capable of causing a voltage output when a force is applied to the proof mass as a result of acceleration. These accelerometers can also have different conformations depending on

the application. It should also be noted that these accelerometers do not respond to a continuous component of accelerations [105, 107].

Finally, piezoresistive-based accelerometers have a similar operating principle to piezoelectric-based. The only difference is that the mechanical stress applied by the proof mass translates into a change of the material resistivity. Therefore, the resulting resistivity is linear with the force applied, and the output voltage can be measured for a constant electric current using Ohm's Law ($V = RI$). In contrast to the previous ones, these are DC-responsive, simpler and cheaper. The major drawbacks of this operating principle are the temperature-sensitive drift and the lower level of the output signals [105, 107].

The last two principles present more robust characteristics, since they are more associated with high-shock applications. On the other hand, they are less accurate compared to the first type of accelerometer [105].

The three accelerometers detailed herein are illustrated in figure 2.21.

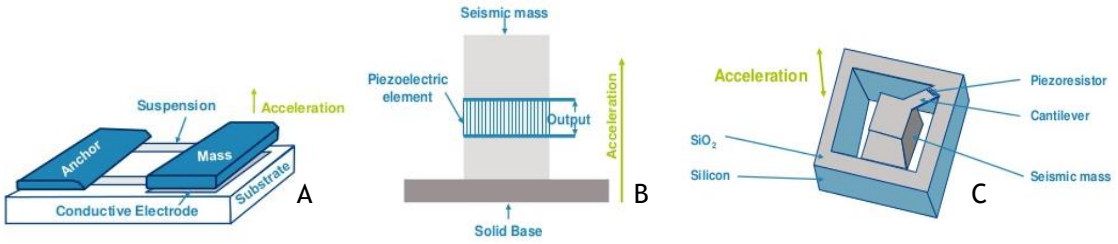

Figure 2.21 - Schematic of MEMS accelerometers. The figure illustrates the capacitive-based accelerometer in A, the piezoelectric-based accelerometer in B and piezorestive-based accelerometer in C. Adapted from [109].

2.3.2.2 - MEMS gyroscopes

In MEMS, mechanical gyroscopes are the most common types. These are based on the Coriolis effect, which is a phenomenon observed when an object moves in the rotating frame of reference at a certain speed. In the frame of reference under analysis, there is a misperception on the part of the observer, where it seems that the object changes its trajectory. This effect is realized by a force called the Coriolis force that is proportional to the rotation speed of the frame of reference. Therefore, by measuring the effect of this force on a proof mass, it is possible to determine the rotational speed of the frame of reference. As for the accelerometers, there are two operating principles that are most commonly used in MEMS gyroscopes: the turning forks or resonant beam and the vibrating plate. These, as well as the previous ones can also have triaxial configurations [105].

The turning forks MEMS gyroscopes are essentially based on resonant structures. Those structures have to be set in motion using an actuator, usually piezoelectric crystal material placed under electrical voltage variation or two electrodes that permute their state between on and off. The turning fork consists of two beams of the same size and a material with a common shaft, which when oscillated at resonance frequency oscillate 180º out-of-phase. As soon as the system rotates in a particular direction, the vibration frequency varies with Coriolis force. This change can be detected by a piezoelectric or piezoresistive material placed on a common shaft [105].

On the other hand, the vibrating plate MEMS gyroscopes have the plate suspended by springs as folded beams. As in the previous one, an actuator vibrates this structure at a specific frequency and phase. If vibration changes similarly to the previous principle in the x-

axis, the normal rotation to the plane in the z-axis will translate into a vibration change in the y-axis. Using this principle and as an example, a variation in the capacitance of a material can be induced, in proportion to the rotation. This is a principle used in triaxial sensors, however other divergent configurations share the same principle but are not as successful as this one presented [105].

For both gyroscopes, their schematics are shown in figure 2.22.

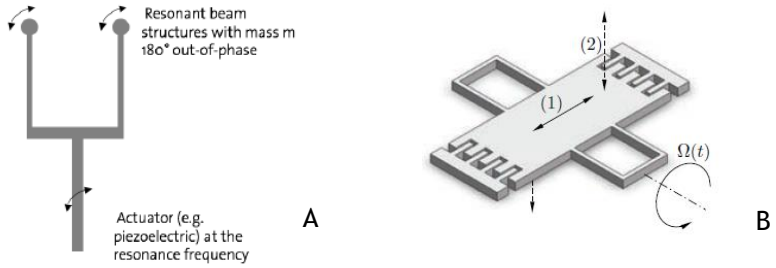

Figure 2.22 - Schematic of MEMS gyroscopes. The figure illustrates the turning fork gyroscope in A and the linear vibrating plate gyroscope in B. Adapted from [105, 110].

2.3.2.3 - MEMS magnetometers

MEMS magnetometers have been employed most frequently in industry, oceanography and medical fields. There are essentially five operating principles, such as the Hall effect, magnetic magnetoresistance (GMR), magnetic tunnelling junction (MTJ) sensing, anisotropic magnetoresistance (AMR) and the latest Lorentz force. As the previous ones, these can also have triaxial configurations [111].

Hall Effect based MEMS magnetometers are currently the most common on the market. Its operation principle involves detecting a voltage difference (the Hall voltage) across a thin metallic element when a strong magnetic field is placed perpendicular to the element plane. This method allows creating MEMS magnetometers of small size, low consumption and cheap. On the other hand, it produces a smaller output signal and has low sensitivity and temperature stability when compared with the other methodologies [111].

GMRs are based on a quantum effect. In their simplest form, these sensors use the four-layer structure that consists of two thin-film ferromagnets separated by a material conductor. The fourth layer is an antiferromagnetic field that is used to fix or inhibit the rotation of the magnetization of the ferromagnetic layers. Consequently, electrical resistance can change between two values depending on the relative alignment of the magnetization in the layers, aligned "up" or "down" according to an external magnetic field, sharing similar characteristics to a spin valve. These sensors are capable of displaying high sensitivity levels, a wide range of output signal and significant stability with temperature. However, the major disadvantage is their high cost given their manufacturing complexity [111].

The MTJs are based on a quantum mechanical phenomenon. Its structure is consisted in two ferromagnets (magnetic layers) separated by a very thin layer of insulating material (barrier layer). The electrons can move from one ferromagnet to another using a procedure similar to the GMR, the only difference is that the middle layer is insulating rather than conductive [112]. Thus, when a voltage is applied to the top and bottom of the structure, the current flow between the two magnetized materials. This current is maximized when the fields in both layers are aligned with one another and minimized when the two fields have opposite polarity [113]. This sensor simulates the resistor effect that is dependent on the

magnetic field. This methodology allows a high output signal range with high sensitivity and low noise. By contrast, it consumes more energy and the cost is too high taking into account the philosophy of MEMS [111].

The AMR is another approach that has the concept of using a common material to act as a magnetometer. In this case, the permalloy (alloy with 80% nickel and 20% iron) is used in a way that its resistance is dependent on the angle between the direction of electric current and the direction of magnetization. In the presence of a magnetic field, magnetization rotates toward the direction of the magnetic field depending on its magnitude. The resistance value decreases as the magnetization direction rotates away from the direction of the current, reaching its minimum when they are perpendicular. Although this principle has a low range of signal output, it has been widely used in consumer mobile phones once it is sufficient and becoming an increasing competitor to the Hall effect magnetometers. In addition, it has even better sensitivity and stability with temperature [111].

Finally, the most recent ones to reach this market were the Lorentz force magnetometers. Lorentz force is defined as the combination of electric and magnetic force on a point charge due to electromagnetic fields. These sensors sense the Lorentz force from one or more current-carrying beams, causing the movement of a suspended mass. This movement can then be felt from capacitive, piezoresistive, and in some cases optical sensors. In its more simplistic implementation, the sensor is composed of two springs with both ends connected, where the current crosses. In the middle of the springs, a frame (rotor) is suspended by which ideally the current does not cross and where the stators are anchored. In the presence of an out-of-plane magnetic field, the Lorentz force appears on the springs. This force causes a deformation in the springs, which in turn causes the displacement of the suspended frame. Since the stators do not move, the value between the rotor and stators changes in a way proportional to the external magnetic field [114, 115].

All the magnetometers described in this subsection are schematically represented in figure 2.23.

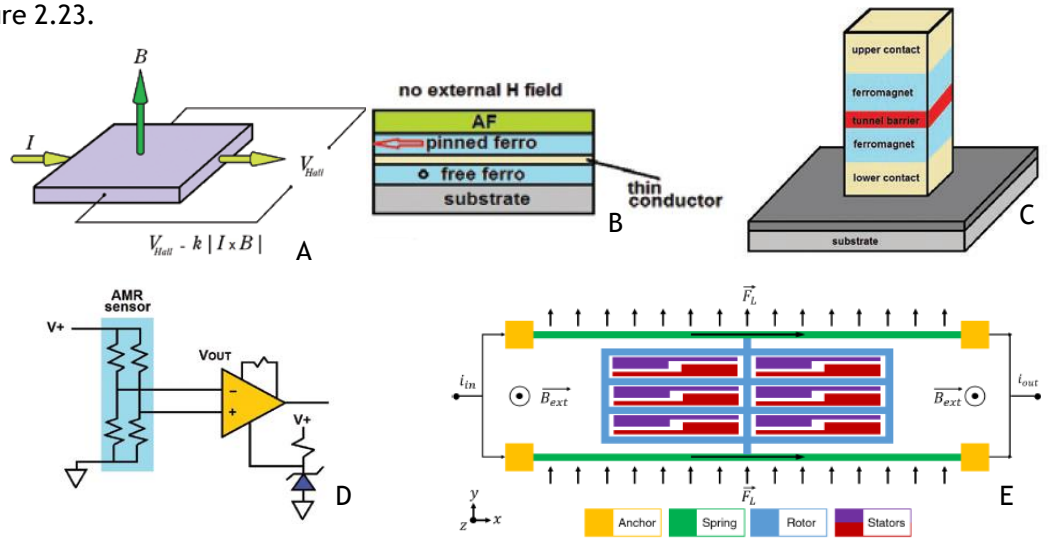

Figure 2.23 - Schematic of MEMS magnetometers. The figure illustrates Hall effect based MEMS magnetometer in A, the GMR magnetometer in B, the AMR magnetometer in C, the MTJ magnetometer in D, and Lorentz force magnetometers in E. Adapted from [111, 115].

2.3.3 -Reference Frames

Before highlighting the representation of orientation and the algorithms for orientation's estimation, some concepts must be detailed, including coordinate frames. Usually, there are four frames that must be taken into account. Firstly, the body frame is the coordinate frame of the moving IMU, with the origin at the center of the device and in line with the axes of the sensors. All inertial measurements are calculated in this frame. The inertial frame is a stationary frame with its origin located in the center of the earth with its axes aligned with respect to the stars. It is in respect to this frame that the IMU measures its linear acceleration and angular velocity. The navigation frame is a local geographic frame to where the IMU will navigate, that allows maintaining the relation of position and orientation between this and body frame. For small movements, this frame is considered stationary. Finally, the earth frame, also known as ECEF (earth-centered, earth-fixed), coincides with the inertial frame differing only in rotation according to the earth. However, since in applications such as human motion tracking the movements are mostly related with orientation and have relatively small temporal analysis, the literature tends to fuse the designations of earth frame and inertial frame given their similarities [116]. These last three frames are schematically shown in figure 2.24 [107].

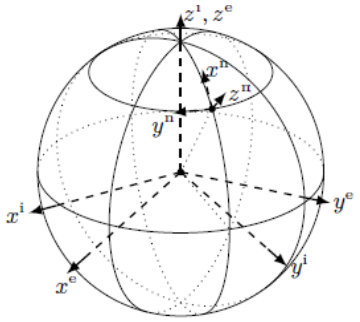

Figure 2.24 - Illustration of the earth frame (e-frame), inertial frame (i-frame) and navigation frame (n-frame). This figure illustrates the three frames external to the device and their relations [107].

In practice, it is common to use algorithms that compute orientation in relation to the North east down (NED) geographical coordinate system, also known as the local navigation system. Its origin can be established at any point of the globe and the axis points to the true north, the z-axis points to the center of the Earth, and its y-axis is referenced according to the right-hand rule, as shown in figure 2.25, where the green axes represent the NED system and the orange axes the earth frame [117].

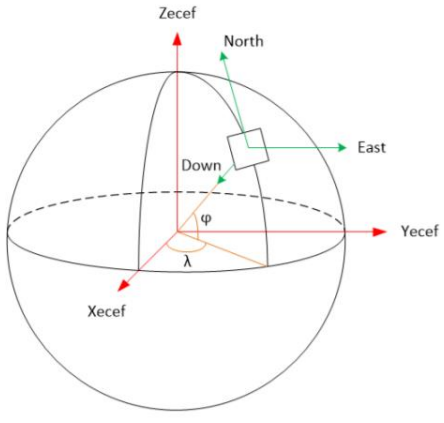

Figure 2.25 - NED coordinate system [117].

2.3.4 -Representation of Orientation

The orientation is calculated as a set of parameters that relates the angular position of a frame to another reference frame. There are a large number of methods that can describe this relationship, some are simpler and easier to visualize, but all have some limitations. Among all, the direction cosine matrix (DCM), Euler angles and quaternions are the most outstanding in practice. In addition, all these methods involve a rotation matrix that can be called either the transformation matrix or the direction cosine matrices (DCM). All methods can be related to each other through specific equations for each case [118].

In the first place, the direction cosine matrix (DCM) is a rotational matrix where the entries are the cosines of the angles between each basis vector of the two frames. This matrix allows a good physical interpretation, and thus it has been a widely used method. This method has as main disadvantage the amount of elements needed to describe the rotation when compared to the following methodologies [119]. In practice, six of the nine parameters turn out to be redundant, thus being related to the Euler angles [120].

The DCM between the two frames is given by:

$$[C] = \begin{bmatrix} \cos\alpha_{11} & \cos\alpha_{12} & \cos\alpha_{13} \\ \cos\alpha_{21} & \cos\alpha_{22} & \cos\alpha_{23} \\ \cos\alpha_{31} & \cos\alpha_{32} & \cos\alpha_{33} \end{bmatrix}. \qquad (2.1)$$

The previously mentioned Euler angles define the rotation as a consecutive rotation around three axes. Considering the conventional axes (x, y, z), there are 12 distinct ways of applying consecutive rotation. Note that 3x2x2=12, since if they have two successive rotations on the same axis, it would combine in only one rotation. Although the terminations are often used inconsistently, there is a convention to denominate Proper Euler angles at rotations that involve the same axis more than once, and Tait-Bryan angles the rotations that involve the 3 axes. In this work, it will be used the consecutive z-y-x (or 3-2-1) convention from the Tait-Brain angles, as it is the most indicated (reasons to be addressed in the next chapter) and one of the most used in practice [121].

In the z-y-x convention, the first angle ψ is calculated around the z-axis, then the angle θ is calculated around the y-axis and finally the angle Φ around the x-axis. The angles described are represented in figure 2.26 and are generally referred to as yaw (or heading), pitch and roll, respectively [107].

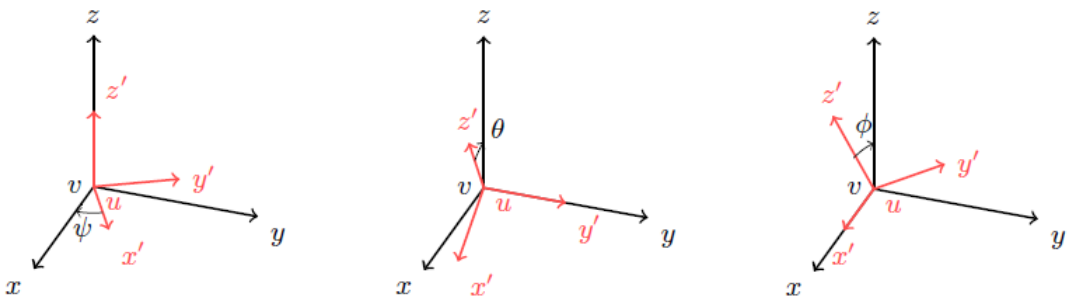

Figure 2.26 - Schematization of Tait-Bryan angles. This figure shows the rotation of the yaw around the z-axis in A, the rotation of the pitch around the y-axis in B, and the rotation of the roll around the x-axis in C [107].

Supporting with a practical case, the Tait-Bryan angles are represented by figure 2.27.

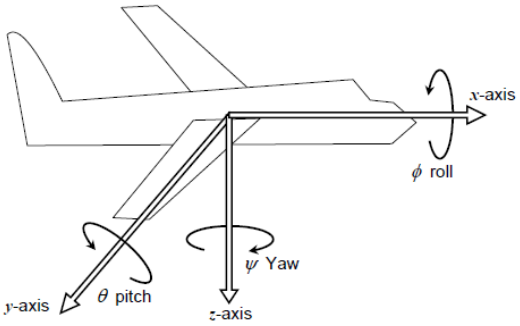

Figure 2.27 - Tait-Bryan angles (practical case) [121].

Assuming the frames of figure 2.26, the rotation of the v-frame (ψ, θ, φ) with respect to a u-frame is given by the rotation matrix R^{UV}:

$$R^{UV} = R_z^{UV}(\psi)R_y^{UV}(\theta)R_z^{UV}(\Phi)$$

$$= \begin{pmatrix} \cos\psi & -\sin\psi & 0 \\ \sin\psi & \cos\psi & 0 \\ 0 & 0 & 1 \end{pmatrix} \begin{pmatrix} \cos\theta & 0 & \sin\theta \\ 0 & 1 & 0 \\ -\sin\theta & 0 & \cos\theta \end{pmatrix} \begin{pmatrix} 1 & 0 & 0 \\ 0 & \cos\Phi & -\sin\Phi \\ 0 & \sin\Phi & \cos\Phi \end{pmatrix}$$

$$= \begin{pmatrix} \cos\psi\cos\theta & \cos\psi\sin\theta\sin\Phi - \sin\psi\cos\Phi & \cos\psi\sin\theta\cos\Phi + \sin\psi\sin\Phi \\ \sin\psi\cos\theta & \sin\psi\sin\theta\sin\Phi + \cos\psi\cos\Phi & \sin\psi\sin\theta\cos\Phi - \cos\psi\sin\Phi \\ -\sin\theta & \cos\theta\sin\Phi & \cos\theta\cos\Phi \end{pmatrix}. \quad (2.2)$$

Although the Euler angles provide the calculations in a more intuitive and representative way, its main drawbacks are expressed in a higher computational cost, and by the fact that they possess discontinuities inherent in trigonometric functions and high nonlinearity attributes [123, 124]. In fact, it is meant that the representations of the Euler angles or Tait-Bryan angles are not unique descriptions of rotation essentially in two situations.

The first one due to the wrapping of the angles, meaning that the rotation for angles (0,0,0) and (0,0,2πk) where k is any integer, the values are the same. The second one and the most important in practice focuses on the possibility of the second consecutive angle reaching $\theta = \pm\pi/2$ (θ in this case), which causes a phenomenon called gimbal lock, where one degree of freedom is lost in a three-dimensional, three-gimbal mechanism that occurs when the axes of two of the three gimbals are driven into a parallel configuration. In this configuration, the gimbals lie in a single plane and rotation within that plane is "locked out" by the gimbal mechanism [121]. In the gimbal lock position, the $\tilde{x}$-axis becomes parallel to the z-axis and the consecutive rotations collapse down to a single main rotation, as shown in equation 2.3 and 2.4.

$$\theta = \frac{\pi}{2}: \quad R_z(\psi)R_y\left(\frac{\pi}{2}\right)R_x(\Phi) = R_z(\psi + \Phi) \quad (2.3)$$

$$\theta = -\frac{\pi}{2}: \quad R_z(\psi)R_y\left(-\frac{\pi}{2}\right)R_x(\Phi) = R_z(\psi - \Phi) \quad (2.4)$$

The quaternions are a reasonably common parameterization for orientation estimation. The unit quaternion is a set of four normalized parameters where three complex components

form an axis of rotation, and the real component describes the rotation about that axis [115, 123]. These elements use the 4-dimensional representation of the orientation according to:

$$q = \begin{pmatrix} q_0 & q_1 & q_2 & q_3 \end{pmatrix}^{\mathsf{T}} = \begin{pmatrix} q_0 \\ q_v \end{pmatrix}, \qquad q \in \mathbb{R}^4, \qquad \|q\|_2 = 1. \tag{2.5}$$

This method has as main advantages the absence of high nonlinearities and gimbal lock, unlike the Euler angles. On the other hand, it has a much more complex physical interpretation and needs one more element compared to the Tait-Bryan angles [115, 123].

Finally, since the sensor fusion algorithm usually provides the output in quaternions and given the need for more noticeable orientation, the conversion between quaternion and Tait-Bryan angles (z-y-x convention) is given by [121]:

$$\Phi = arctan2((q_2q_3 + q_0q_1), \tfrac{1}{2} - (q_1^2 + q_2^2)) \tag{2.6}$$

$$\theta = arcsin(-2(q_1q_3 - q_0q_2)) \tag{2.7}$$

$$\psi = arctan2((q_1q_2 + q_0q_3), \tfrac{1}{2} - (q_2^2 + q_3^2)) \tag{2.8}$$

2.3.5 -Estimation of Orientation

As already mentioned, the use of inertial sensors has been increasing in medical applications. In this field, they stand out for their ability to track human motion from one or a combination of multiple sensors to obtain information on the pose of several zones connected to each other. Currently, there is already a large amount of literature about the use of inertial sensors for estimating orientation and position. However, it is essential to keep in mind that these are nonlinear estimation problems where different parameterizations with their own properties must be considered, depending on the accuracy to be achieved [107].

The estimation of the orientation of a device is made from the integration of the gyroscope over time. After subtracting the gravity of the earth, the accelerometers can provide information about the position of the sensor over time from the double integration of the data. The estimation of position and orientation are inherently linked, a process commonly called dead-reckoning and represented in figure 2.28 [107].

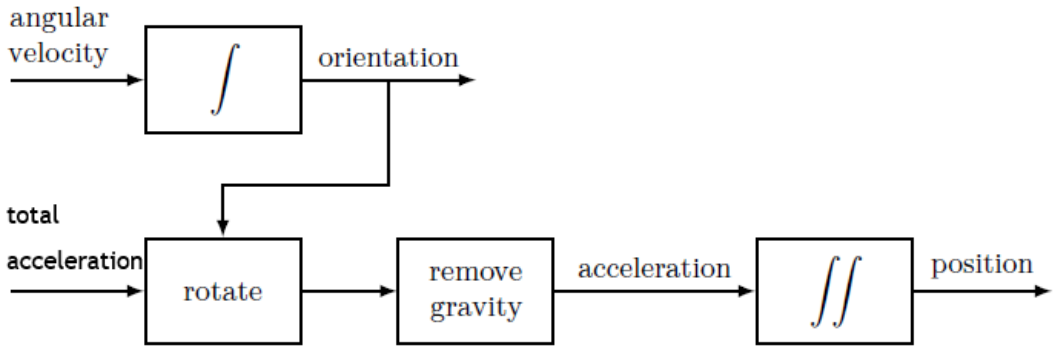

Figure 2.28 - Schematic illustration of dead-reckoning. This scheme illustrates the common process for obtaining the position and orientation of the data coming from the accelerometer and gyroscope [107].

In theory, this presented model would be capable of a correct estimation. In practice, the inertial measurements are noisy and biased, introducing an integration drift in the

integrations of angular velocity and acceleration. Generally, it is found that the integration of a constant bias and noise causes a distinct cumulative drift for each axis, even with the device in a steady state. Furthermore, a more significant drift is found in the estimation of the position since the values need to be integrated twice. Therefore, having some inaccuracies in the orientation estimation can lead to a wrong subtraction of gravity [107].

In order to suppress the presented problem, the inertial sensors are often supplemented with other sensors with lower sampling rate but without drift over time. For the estimation pose, inertial sensors are usually combined with global navigation satellite systems (GNSS), ultrawideband systems (UWB) or cameras. In this dissertation, the combination of inertial sensors with magnetometers becomes the most interesting solution to improve the estimation. Thus, the initial conditions for proper integration of the gyro data are given by the combination of the accelerometer with the magnetometer [106, 116].

To sum up, gyroscopes alone cannot provide an accurate measurement of orientation. An accelerometer and magnetometer will measure the earth's gravitational and magnetic fields respectively, and so give an absolute reference of orientation. However, they are likely subject to higher levels of noise. As an example, accelerations caused by motion will corrupt the estimated direction of gravity.

The task of an orientation filter is to compute a single estimate of orientation through the optimal fusion of gyroscope, accelerometer and magnetometer measurements [125]. In orientation filters, accelerometers are usually used to calculate the vertical direction from the gravity measurement, which can be decomposed into more than one axis when there is a slope, allowing corrections in pitch and roll. The orientation around the vertical axis is calculated from the magnetic field measured by the magnetometer. In this way, it is possible to correct the heading or yaw angle and provide horizontal stability. This principle works correctly, except when it is in the north or south magnetic pole [106]. This process of combining data from two or the three sensors to improve the accuracy is known as sensor fusion. Currently in the literature, there are essentially two major approaches developed in the last few years: Kalman Filters and Complementary Filters [126, 127].

2.3.5.1- **Kalman Filters**

The Kalman filter is commonly used in practice, combining data and noise filtering with sensor fusion. Due to their extensive applicability, Kalman filters are used in a wide range of fields given the existing generalized derivations. Once the orientation is inherently a nonlinear problem, these types of filters have become standard where the Extended Kalman Filter and Unscented Kalman Filter stands out [128, 129].

However, despite its popularity, Kalman based algorithms have shown an increased computational cost due to its complexity and intensive matrix operations, which makes it impractical to use in embedded systems and small mobile devices [127]. The need for alternative approaches has led to the development of the complementary filters, which are characterized by being more straightforward and with similar accuracy to Kalman filters.

2.3.5.2- **Complementary Filters**

The complementary filters are a relatively recent concept that have been implemented to compute the orientation in several areas. From a broader perspective, the unreliable frequencies of each sensor are filtered, combining them into a final output for a better

estimation throughout the entire bandwidth of the system. As an example, while the accelerometer and magnetometer have reliable data at lower frequencies, the gyroscope has it at higher frequencies, becoming good indicators of static and dynamic conditions, respectively [128].

Although the simpler implementations have less adaptability, there are already solutions to increase the resilience of the filters, such as the gradient descent based complementary filter (GDCF) suggested by Madgwick et al. [116] and the explicit complementary filter (ECF) developed by Mahony et al. [129]. These two methodologies implement novel approaches of filter adaptation in order to enable the estimation of sensor bias and readings deviations, opening doors to a new world of real-time acquisition of small devices with limited computational power. The mentioned complementary filters will be discussed in detail since they will be used in this work. The Complementary Filters are divided into 3 main sections: orientation from angular rate, algorithm fusion process and magnetic distortion compensation.

Orientation from Angular Rate

Initially and as already mentioned, the tri-axis gyroscope will measure the angular rate in the x, y, and z-axes denoted by ω_x, ω_y and ω_z (in rad/s), respectively. At this stage, the quaternion derivative describing the rate of change of the sensor frame relative to the earth frame is computed, ${}^{S}_{E}\dot{q}$, where ^ denotes the normalized vector of unit length. For a period [t-1, t], the solution is described by [125, 127]:

$$ {}^{S}_{E}\dot{q}_{\omega,t} = \frac{1}{2} {}^{S}_{E}\hat{q}_{est,t-1} \otimes {}^{S}p_t \,, \qquad (2.9) $$

where ${}^{S}_{E}\hat{q}_{est,t-1}$ is the previous orientation's estimation and ${}^{S}p = \left[0, {}^{S}\omega\right] = \left[0 \;\; \omega_x \;\; \omega_y \;\; \omega_z\right]$.

Considering Δt as the sampling period, the orientation of the earth frame relative to the sensor frame at time t, ${}^{S}_{E}q_{\omega,t}$ is given by:

$$ {}^{S}_{E}q_{\omega,t} = {}^{S}_{E}\hat{q}_{est,t-1} + {}^{S}_{E}\dot{q}_{\omega,t}\,\Delta t \,. \qquad (2.10) $$

To differentiate from the remaining quaternions in the process, the quaternions calculated so far are indicated by ω in the subscript.

Algorithm Fusion Process

It is essentially at this stage that the two algorithms are distinguished. In this section, the filters developed by Madgwick and Mahony are presented. For this, it will be assumed that ${}^{S}\hat{a}_t$ represents the normalized accelerometer measurement, ${}^{E}\hat{g}$ the gravity vector (defined as ${}^{E}\hat{g} = [0 \;\; 0 \;\; 0 \;\; 1]$), ${}^{S}\hat{m}_t$ the normalized magnetometer measurement, and ${}^{S}\hat{b}_t$ the predicted magnetic field orientation explained in the next section [125, 127, 130].

Motivated by the need **of** light and accurate fusion sensor algorithm with a focus on motion tracking, Magdwick et al. presented in 2011 a dynamic GDCF for IMUs and MARGs sensors. Madgwick stands out from Mahony's implementation by integrating a gradient descent as an optimization algorithm for its simplicity of computation, which is described in equation 2.11. For an orientation estimated at time t, the estimated orientation, ${}^{S}_{E}\hat{q}_{\nabla,t}$, is

calculated from the previous estimation, ${}^{S}_{E}\hat{q}_{\mathrm{est,t-1}}$, the step-size variable, μ_t, and the objective function error, ∇f [125].

$$ {}^{S}_{E}\hat{q}_{\nabla,\mathrm{t}} = {}^{S}_{E}\hat{q}_{\mathrm{est,t-1}} - \mu_t \frac{\nabla f}{\|\nabla f\|} \tag{2.11} $$

The value of ∇f is defined by:

$$ \nabla f = \begin{cases} J_g^T\left({}^{S}_{E}\hat{q}_{\mathrm{est,t-1}}\right) f_g\left({}^{S}_{E}\hat{q}_{\mathrm{est,t-1}},\ {}^{S}\hat{a}_t\right) \\ J_{g,b}^T\left({}^{S}_{E}\hat{q}_{\mathrm{est,t-1}},\ {}^{E}\hat{b}\right) f_{g,b}\left({}^{S}_{E}\hat{q}_{\mathrm{est,t-1}},\ {}^{S}\hat{a}_t,\ {}^{E}\hat{b},\ {}^{S}\hat{m}_t\right) \end{cases}, \tag{2.12} $$

where the equations refer to the use of the accelerometer, or the accelerometer and magnetometer, respectively. In the equations above, J represents the Jacobian and objective function, f, is calculated from the formats generically defined by:

$$ f_g\left({}^{S}_{E}\hat{q},\ {}^{S}\hat{a}\right) = \begin{bmatrix} 2(q_2q_4 - q_1q_3) - a_x \\ 2(q_1q_2 + q_3q_4) - a_y \\ 2\left(\frac{1}{2} - q_2^2 - q_3^2\right) - a_z \end{bmatrix}, \tag{2.13} $$

$$ f_b\left({}^{S}_{E}\hat{q},\ {}^{E}\hat{b},\ {}^{S}\hat{m}\right) = \begin{bmatrix} 2b_x(0.5 - q_3^2 - q_4^2) + 2b_z(q_2q_4 - q_1q_3) - m_x \\ 2b_x(q_2q_3 - q_1q_4) + 2b_z(q_1q_2 + q_3q_4) - m_y \\ 2b_x(q_1q_3 + q_2q_4) + 2b_z(0.5 - q_2^2 - q_3^2) - m_z \end{bmatrix}, \tag{2.14} $$

and

$$ f_{g,b}\left({}^{S}_{E}\hat{q},\ {}^{S}\hat{a},\ {}^{E}\hat{b},\ {}^{S}\hat{m}\right) = \begin{bmatrix} f_g\left({}^{S}_{E}\hat{q},\ {}^{S}\hat{a}\right) \\ f_b\left({}^{S}_{E}\hat{q},\ {}^{E}\hat{b},\ {}^{S}\hat{m}\right) \end{bmatrix}. \tag{2.15} $$

The value of μ_t must ensure that the convergence rate of ${}^{S}_{E}q_{\nabla,\mathrm{t}}$ is limited by the physical orientation rate to avoid large step sizes. This requirement is guaranteed by equation 2.16, where Δt is the sampling period, ${}^{S}_{E}\dot{q}_{\omega,t}$ is the rate of change of orientation measured by the gyroscope and α in the augmentation of μ to account for noise in accelerometer and magnetometer measurements.

$$ \mu_t = \alpha \left\| {}^{S}_{E}\dot{q}_{\omega,t} \right\| \Delta t, \alpha > 1 \tag{2.16} $$

Thus, the main goal of this fusion is to provide an estimation of the orientation where ${}^{S}_{E}q_{\omega,t}$ is used to filter the errors at high frequencies in ${}^{S}_{E}q_{\nabla,\mathrm{t}}$ which in turn compensates the integral drift in ${}^{S}_{E}q_{\omega,t}$ and provide convergence of the initial state. This fusion can then be described by equation 2.17, where ${}^{S}_{E}q_{est,t}$ represents the estimated quaternion, and γ_t the variable responsible for assigning the weights applied to each orientation computed in the previous steps.

$$ {}^{S}_{E}q_{est,t} = \gamma_t {}^{S}_{E}q_{\nabla,\mathrm{t}} + (1 - \gamma_t){}^{S}_{E}q_{\omega,t}, 0 \le \gamma_t \le 1 \tag{2.17} $$

The ideal value for γ_t should ensure the weighted rate of divergence of ${}^{S}_{E}q_{\omega,t}$ because the integral drift is equal to the weighted rate of convergence of ${}^{S}_{E}q_{\nabla,\mathrm{t}}$. Equation 2.18 represents the computation of γ_t, where β is the divergence rate of ${}^{S}_{E}q_{\omega}$ expressed as the magnitude of a derivative quaternion corresponding to the gyroscope measurement error, and $\mu_t/\Delta t$ is the convergence rate of ${}^{S}_{E}q_{\nabla}$.

$$\gamma_t = \frac{\beta}{\frac{\mu_t}{\Delta t} + \beta} \qquad (2.18)$$

The fusion is considered optimal when it is assumed that the convergence rate of ${}^{S}_{E}q_{\nabla}$ controlled by α is equal or higher than the rate of change of physical orientation. Considering a large value for α, according to equation 2.16, μ_t will become equally large and equation 2.11 is simplified, since ${}^{S}_{E}\hat{q}_{\mathrm{est},t-1}$ becomes negligible, thus arriving to equation 2.19.

$${}^{S}_{E}q_{\nabla,t} \approx -\mu_t \frac{\nabla f}{\|\nabla f\|} \qquad (2.19)$$

Similarly, the calculation of γ_t can be simplified, since the β in denominator becomes negligible, reaching the equation 2.20, where it is also possible to infer that $\gamma_t \approx 0$.

$$\gamma_t \approx \frac{\beta \Delta t}{\mu_t} \qquad (2.20)$$

Substituting equation 2.17 for the demonstrations so far illustrated, it becomes possible to achieve the equation 2.21, where γ_t is replaced by equation 2.20 and then by 0.

$${}^{S}_{E}q_{est,t} = \frac{\beta \Delta t}{\mu_t}\left(-\mu_t \frac{\nabla f}{\|\nabla f\|}\right) + (1-0)\left({}^{S}_{E}\hat{q}_{est,t-1} + {}^{S}_{E}\dot{q}_{\omega,t}\,\Delta t\right) \qquad (2.21)$$

This can be further simplified in equation 2.22, where ${}^{S}_{E}\dot{q}_{est,t}$ symbolizes the estimated rate of change of orientation defined by equation 2.23.

$${}^{S}_{E}q_{est,t} = {}^{S}_{E}\hat{q}_{est,t-1} + {}^{S}_{E}\dot{q}_{est,t}\,\Delta t \qquad (2.22\ (2.10\ \text{revised}))$$

$${}^{S}_{E}\dot{q}_{est,t} = {}^{S}_{E}\dot{q}_{\omega,t} - \beta \frac{\nabla f}{\|\nabla f\|} \qquad (2.23)$$

As it is possible to visualize by the two last equations, the fusion algorithm calculates ${}^{S}_{E}q_{est}$ through the integration of ${}^{S}_{E}\dot{q}_{est}$. In turn, this filter computes ${}^{S}_{E}\dot{q}_{est}$ from ${}^{S}_{E}\dot{q}_{\omega,t}$ described in the initial section and the magnitude of measurement error, β, removed in the direction of the estimated error $\nabla f/\|\nabla f\|$. The orientation's estimation algorithm presented by Madwick et al. needs the adjustable parameter, β, representing the gyroscope measurement error expressed as the magnitude of a derivative quaternion. In practice, for higher values of β, smaller errors due to integral drift are obtained and faster the bias correction, but in return, the noise due to large steps of gradient descent iterations will be higher. Finally, the normalization of the output quaternion is shown in equation 2.24.

$${}^{S}_{E}\hat{q}_{est,t} = \frac{{}^{S}_{E}q_{est,t}}{\|{}^{S}_{E}q_{est,t}\|} \qquad (2.24)$$

The Explicit Complementary Filter (ECF) proposed by Mahony et al. is distinguished by providing the feedback of the angular error from a PI (proportional-integral) controller. In this way, this type of complementary filter has the advantage of being controlled by two variables, K_p and K_i, unlike the previous one [127, 130].

Considering that ${}^{S}p_t$ is given by:

$${}^{S}p_t = [0,\ {}^{S}\Omega_t], \qquad (2.25)$$

and ${}^{S}\Omega_t$ represents the data fusion, where the data of the gyroscope is debiased by the feedback error. For this, the explicit complementary algorithm uses the normalized data from the accelerometer, ${}^{S}\hat{a}_t$, and then estimates the direction of gravity from the quaternion output as shown in equation 2.26.

$${}^{S}\hat{g}_t = {}^{S}_{E}\hat{q}^{*}_{est,t-1} \otimes {}^{E}\hat{g} \otimes {}^{S}_{E}\hat{q}_{est,t-1} \qquad (2.26)$$

Thus, it is possible to estimate the angular error, ${}^{S}\omega_{e,t}$, by calculating the cross multiplication between the normalized accelerometer data and the estimated direction of gravity as:

$${}^{S}\omega_{e,t} = {}^{S}\hat{a}_t \times {}^{S}\hat{g}_t \qquad (2.27)$$

If there is a magnetometer, ${}^{S}\omega_{e,t}$ is given by equation 2.28, where ${}^{S}\hat{m}_t$ is the normalized magnetometer measurement and ${}^{S}\hat{b}$ is the predicted magnetic field orientation.

$${}^{S}\omega_{e,t} = {}^{S}\hat{a}_t \times {}^{S}\hat{g}_t + {}^{S}\hat{m}_t \times {}^{S}\hat{b}_t \qquad (2.28)$$

Hence, it is applied the data fusion by equation 2.29, which is performed from a PI controller, allowing to control the gain of the angular error and the previous ones. The constant K_p is known as proportional gain and delimits the importance of the gyroscope sensor information versus the accelerometer and magnetometer sensors, while the integral gain, K_i, is used to correct the gyroscope offset drift.

$${}^{S}\Omega_t = {}^{S}\omega_t + K_p \,.\, {}^{S}\omega_{e,t} + K_i \,.\, \int {}^{S}\omega_{e,t} \qquad (2.29)$$

The value of ${}^{S}\Omega_t$ is then placed in equation 2.25 and it is computed the derivative quaternion ${}^{S}_{E}\dot{q}_{\omega,t}$. For a sample period Δt, the quaternion output is obtained by integrating the quaternion derivative:

$${}^{S}_{E}q_{est,t} = {}^{S}_{E}\hat{q}_{est,t-1} + {}^{S}_{E}\dot{q}_{\omega,t}\,\Delta t \qquad (2.30\ (2.10\ \text{revised}))$$

Finally, it is computed the normalized output quaternion, as shown in equation 2.24.

$${}^{S}_{E}\hat{q}_{est,t} = \frac{{}^{S}_{E}q_{est,t}}{\left\|{}^{S}_{E}q_{est,t}\right\|} \qquad (2.24)$$

Magnetic Distortion Algorithm

The computation of the predicted reference direction of the earth's magnetic field, ${}^{E}\hat{b}_t$, is made from the measured direction of the earth's magnetic field, ${}^{E}\hat{h}_t$, normalized by only admitting components in the x and z-axes of the earth frame (equations 2.31 and 2.32). Compensating the magnetic distortions through this methodology ensures that the magnetic disturbances only affect the estimated yaw/heading component.

$${}^{E}\hat{h}_t = \begin{bmatrix} 0 & h_x & h_y & h_z \end{bmatrix} = {}^{S}_{E}\hat{q}_{est,t-1} \otimes {}^{S}\hat{m}_t \otimes {}^{S}_{E}\hat{q}^{*}_{est,t-1} \qquad (2.31)$$

$$^{E}\hat{b}_t = \begin{bmatrix} 0 & \sqrt{h_x^2 + h_y^2} & 0 & h_z \end{bmatrix} \tag{3.32}$$

Whereas the methodology of Magwick et al. uses $^{E}\hat{b}_t$, Mahony computes $^{S}\hat{b}$ from:

$$^{S}\hat{b}_t = {}_{E}^{S}\hat{q}_{est,t-1}^{*} \otimes {}^{E}\hat{b} \otimes {}_{E}^{S}\hat{q}_{est,t-1} \tag{3.33}$$

The complete high-level block diagrams for each of the algorithms are shown in figure 2.29.

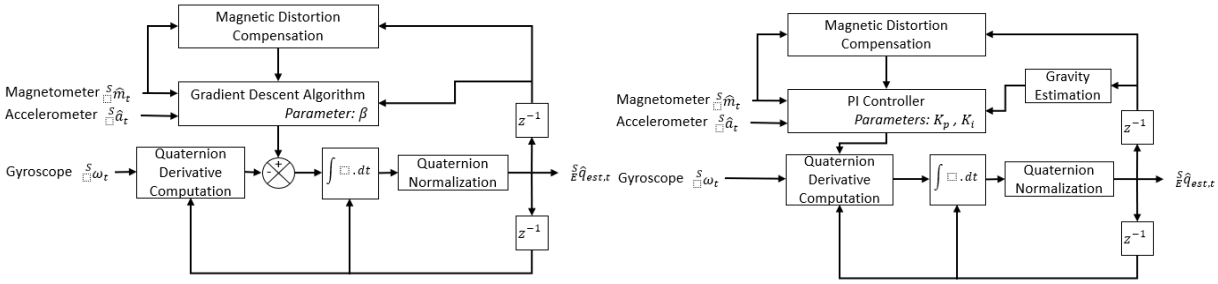

Figure 2.29 - Madgwick and Mahony Filter schematics.

In conclusion, empirical testing and benchmarking analysis performed by Madgwick and Mahony demonstrate equivalent results to the commercial quality Kalman-based systems, even with reductions of the sampling rate and lower computational load. Thus, the two most successful complementary filters presented here open a wide range of opportunities for IMUs and MARGs in real-time applications.

Chapter 3

A Wearable Hand Sensing System

This dissertation aims to develop a new complete system for range of motion (ROM) analysis applied to the wrist articulation and perform the integration of the rigidity algorithm implemented by the BRAIN Lab. Throughout this chapter, the architecture of the system developed and its main features will be presented. Subsequently, focus will be given to the description of the methodology and the operating principles of each tier.

3.1 - System Architecture

The system was developed involving the three tiers of the Wearable Health Systems architecture. In a first part the wearable device was designed from the integration of the desired hardware, and the firmware was developed for acquisition, calibration and data transmission. In the second part an application in Android was developed, allowing the performance of the evaluation and providing feedback in real-time. Finally, in the third part the web service was developed (where all the data is stored), allowing the physician to visualize the history of the exams and the BRAIN Lab to have access to crucial information that can be used to a continuous growth of the project. The general architecture of the developed system is shown in figure 3.1. In order to illustrate the main requirements, the use cases diagram is shown in figure 3.2.

Figure 3.1- Architecture Implemented.

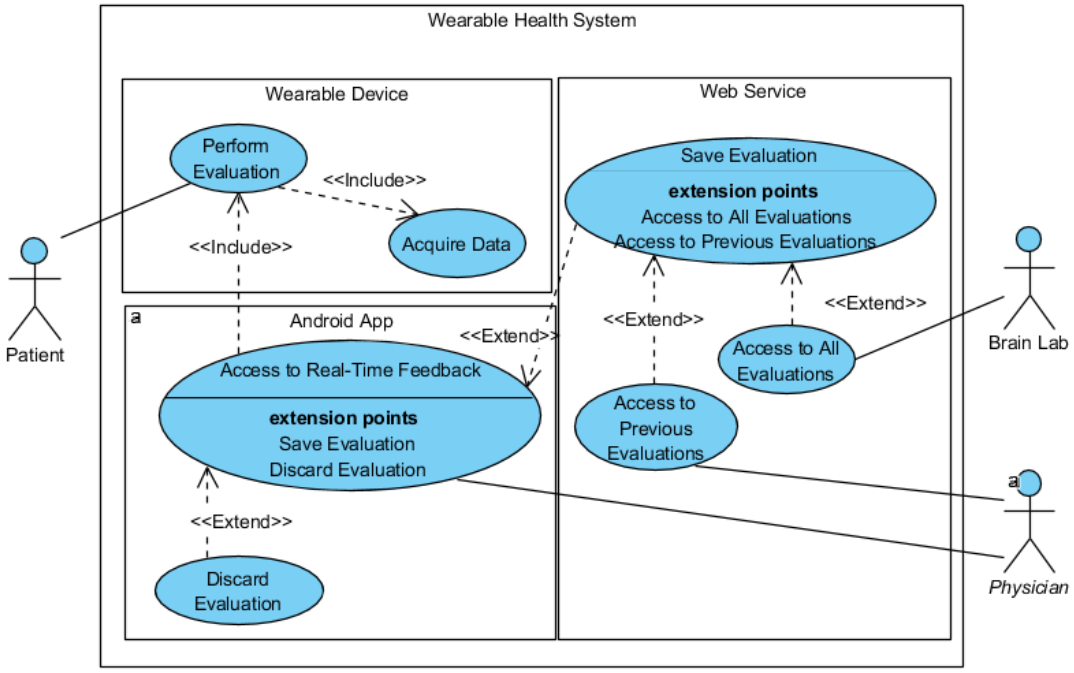

Figure 3.2- Generic Use Cases Diagram.

3.2 - Hardware Integration

This section covers the main electronic components, focusing mainly on their characteristics as well as their connections. Thus, in this dissertation it will be referenced essentially 3 distinct components: the IMU (MPU-9250), the Arduino Pro Mini and the Bluetooth module (RN4871).

3.2.1- Inertial Measurement Unit

The IMU used is called MPU-9250 from InvenSense®, already mounted on a breakout board. This means that the electrical component is an integrated circuit (IC), similar to figure 3.3 [131]. This IMU, powered at 3.3 V_{DC}, allows 9 DoFs and houses a 3-axis accelerometer, a 3-axis gyroscope and a 3-axis magnetometer. It is verified by the datasheet that this IMU has three independent vibratory MEMS rate gyroscopes, separated proof masses for each axis of the accelerometer and a highly sensitive Hall sensor technology for the magnetometer [125, 126].

Figure 3.3 - Inertial Measurement Unit MPU-9250 [131].

It also contains a digital motion processor™ (DMP) capable of offloading computation of motion processing algorithms from the host processor. The DPM acquires the sensor data and has the ability to process it. The main purpose of this unit is to offload both timing

requirements and processing power from the host processor, and it is mainly used when application updates at a much lower rate than necessary for a precise acquisition of motion. Therefore, it can be used not only as a tool to minimize computational power but also for streamline time and host processor software. In practice, this unit can be used in applications such as counting the steps of a low-power pedometer while the host processor is out of action [132].

The analog signals acquired by these sensors are converted to digital from nine 16-bit analog-to-digital converters (ADCs) with signal conditioning for each axis of each hosted sensor. For a more accurate tracking, the components have a changeable full-scale range of ± 250, ± 500, ± 1000, and ± 2000 °/s (dps) for the gyroscope, ± 2g, ± 4g, ± 8g, and ± 16g for the accelerometer and single full-scale range of ± 4800μT for the magnetometer. The MPU-9250 is also designed for more human-driven applications, such as motion-based game controllers and wearable sensors for health, fitness and sports [132]. This sensor uses I^2C (Inter-Integrated Circuit) communication protocol to communicate with the exterior, which will be discussed further with more detail in the Firmware section. Its physical interface consists on serial clock (SCL) and serial data (SDA) lines. With only two connections, it is possible to synchronize all data transfers over the I^2C bus [133].

Still in the hardware, some considerations were necessary regarding the use of two IMUs of the same model. It was required an in-depth study of Sparkfun breakout board schematics to perform physical changes to the circuit and to communicate with both sensors in a synchronized way [134].

The first aspect to be taken into account is the existence of two pre-soldered jumpers (SJ1 and SJ2), which are shown in the schematic of the breakout board in figure 3.4. The jumper SP1 connects the V_{DD} to V_{DDIO} in order to reduce the number of power supplies to one. On the other hand, the two-way SP2 jumper is initially pre-defined to connect the AD0 pin to ground, setting the address of the IMU on the I^2C bus as 0x68. If the solder of the SJ2 is moved to connect the center pad to the pad of the opposite side, it allows the connection of the pin AD0 to the outside. Thus, by connecting the AD0 pin to high or low it is possible to set the I^2C address as 0x69 or 0x68, respectively. In this way, changing one of the IMUs by placing the AD0 pin to high makes it possible to distinguish both on the I^2C bus [131].

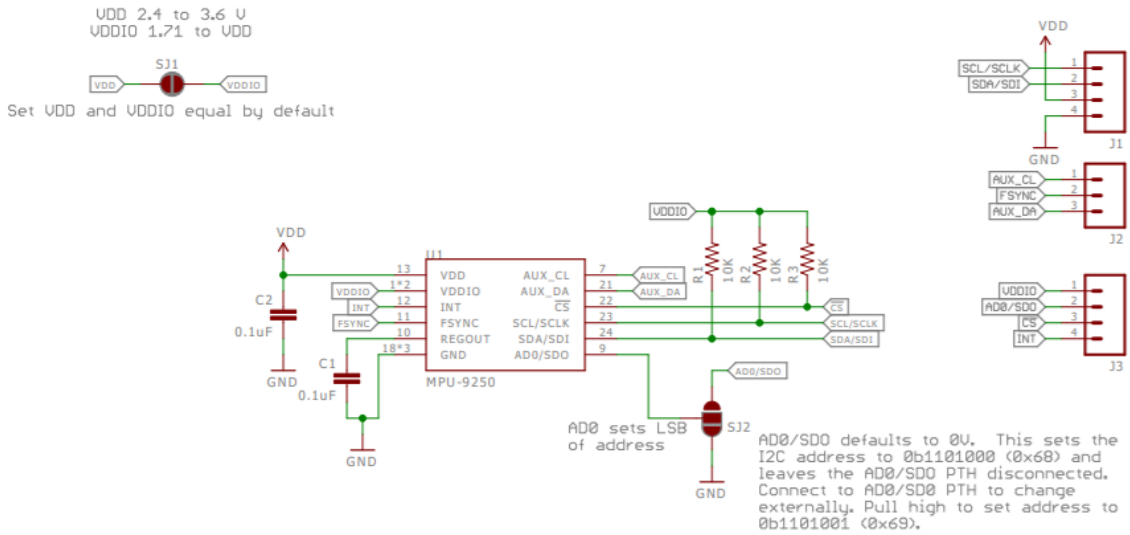

Figure 3.4- IMU MPU9250 schematic [135].

The second important aspect relates to the internal organization of the circuit. Although the addresses of each IMU can be changed physically, by the block diagram of the figure 3.5 it is verified that the magnetometer follows a different structure from the remaining sensors. Since this magnetometer has only one address, the acquisition of magnetometer data in each IMU has an increased complexity. In this case, the developed firmware must be able to make the bypass enabled or disabled for each IMU so that the microcontroller can correctly acquire the required magnetometer data. This process will be covered in the Firmware section.

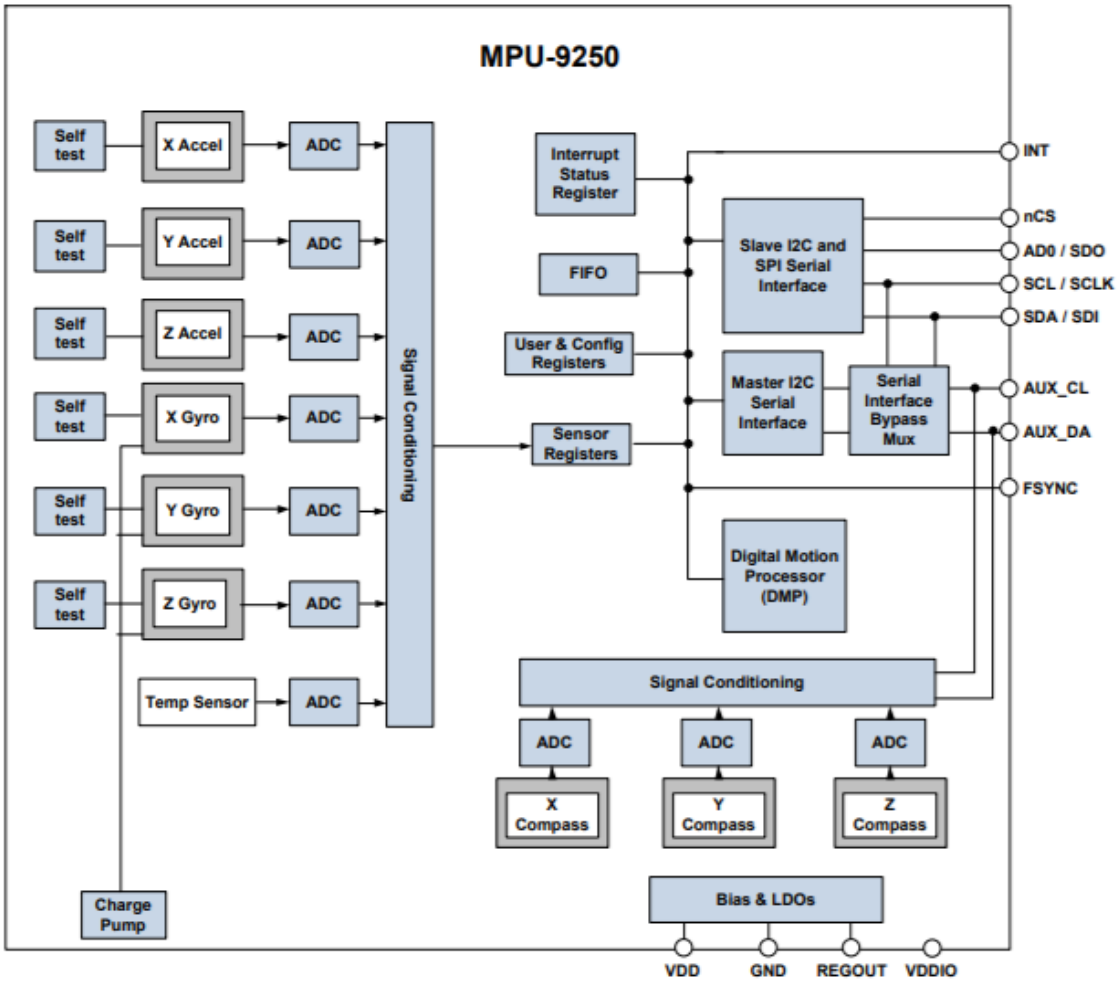

Figure 3.5 - Internal block diagram of MPU9250 [135].

3.2.2- Arduino Pro Mini

The microprocessor used is the Arduino Pro Mini 328 - 3.3V / 8MHz, similar to the one shown in figure 3.6 (A). This is the Arduino where all associated firmware will run, being chosen by its processing capabilities, freedom of implementation and size, which are critical factors in the prototyping and development of wearable devices [136].

It has an ATmega328 running at 8MHz and operates at low voltage, 3.3V, that is enough to power up most of the popular devices found in portable systems. It allows a DC input from 3.3V to 12V since it has a voltage regulator for 3.3V. This microprocessor also has 150mA of maximum output and provides 8 analog pins and 14 digital I/O pins to communicate with external devices [136].

In order to minimize the board, the USB connector is not directly connected to the Arduino, unlike most versions. In this case, it is necessary to connect FTDI Basic Breakout (figure 3.6 (B)) to the Arduino Pro mini according to the layout in figure 3.6 (C). This component allows the conversion from USB to serial, enabling the connection between the Arduino and the computer to load the developed firmware [137].

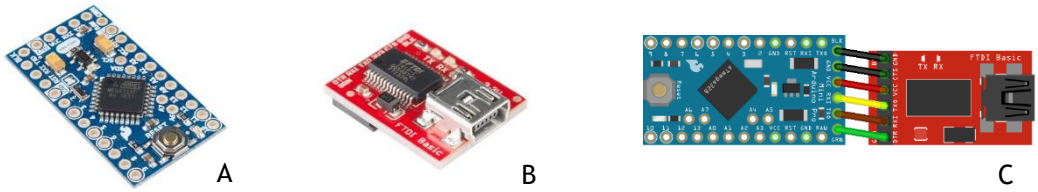

A B C

Figure 3.6 - Arduino Pro Mini and FTDI Basic Breakout. The figure illustrates the Arduino Pro Mini in A, the FTDI Basic Breakout in B and the connection between them in C [136, 137].

3.2.3- Bluetooth Low-Energy

The Bluetooth module integrated was the RN4871 (figure 3.7 (A)) developed by Microchip Technology Inc.. It has a Bluetooth 4.2 low-energy module (BLE) architecture with improved performance and security in connection when compared to previous versions. This makes it a viable option for health/medical devices, sports, IoT, wearable smart devices, among others. This module allows UART interface (Universal asynchronous receiver-transmitter), I2C and SPI (Serial Peripheral Interface), having ASCII interface commands for communication with host microcontroller and an operating range between 1.9V and 3.6V [138, 139].

The breakout board for this Bluetooth has already been designed and manufactured by the BRAIN Lab, and it is shown in figure 3.7 (B). With the implemented board, the Bluetooth will communicate with the Arduino through UART, using serial communication for transferring data. This communication is performed through the TX/RX pins, which behave as transmitters and receivers of data when connected inversely between the two devices. This type of communication will be addressed in the next section, as well as GATT (Generic Attribute Profile) Services, which will be responsible for the Bluetooth communication between the prototype and the smartphone.

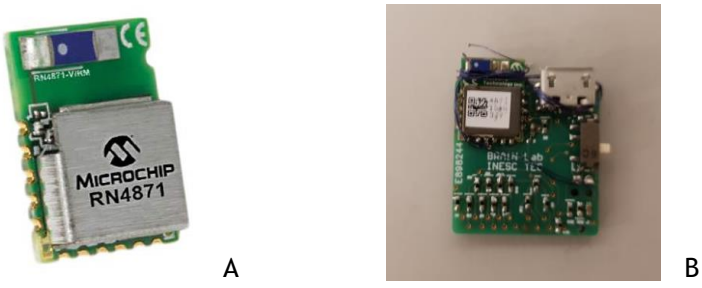

A B

Figure 3.7 - RN4871 Bluetooth module. The figure illustrates the RN4871 in A, and the breakout made by BRAIN Lab [140].

3.2.4- Wearable Device Developed

After the description of each component, all connections are represented in the diagram of figure 3.8. This figure further illustrates the generic relative representation of the components in relation to the hand-wrist complex. For the prototype, it is essential to use 2 IMUs in the illustrated configuration to compute the relative range of motion from the orientation's estimation in each set of sensors.

From the left to the right side of the image, it is possible to find the battery, the Bluetooth module, the Arduino connected to the FTDI Basic Breakout and both IMUs in the proximal and distal positions of the wrist, respectively. Still in this diagram, the red and black wires represent the power, the yellows and oranges ones the serial communication, and finally the green and blue wires represent I^2C communication. Note that the connections between the Arduino and the FTDI Basic Breakout are easily removable and are only used to load the firmware to the microcontroller or provide micro USB power.

At circuit architecture level, the battery was connected to the Bluetooth module and not to the Arduino to take advantage of the circuit already implemented by the BRAIN Lab. This circuit already has a button that allows the control of the current coming from the battery. Thus, it is possible to power the system by battery only when desired, and by USB when portability is not critical.

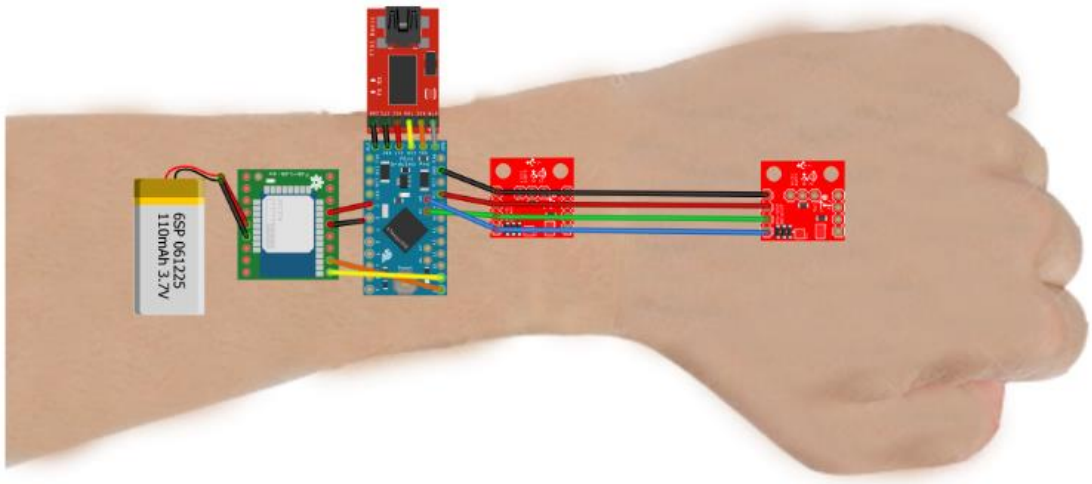

Figure 3.8 - Full diagram circuit. This figure shows from right to left the following components: battery, Arduino Pro Mini, RN4871 Bluetooth module and both MPU-9250 IMUs.

In practice, the sensors were initially placed in a glove, but over time it was proved not to be the most practical model to use. In this sense, the second model was developed from two easy-to-use bands, with elastics to remove the components whenever necessary. This model, although simple to use, adds a greater complexity in the alignment of both IMUs and causes a more significant number of breaks in the wire connections. Thus, future improvements should be made to overcome these problems, which are mentioned in the chapter of conclusion and future work. The final model is shown in figure 3.9.

Figure 3.9 – Final Prototype.

3.3 - Firmware

Firmware is a class of software in which low-level programs are implemented to control a specific set of hardware. For this section, the code was written in C/C ++ using the Arduino IDE (integrated development environment), which also allows a simple way to upload the code to the microprocessor.

3.3.1- Communication Protocols

Before describing the methodology addressed for the firmware of this dissertation, there is some prior knowledge to take into account as the communication protocols used between the microcontroller and the other components. These communication protocols briefly mentioned earlier can be found in figure 3.10.

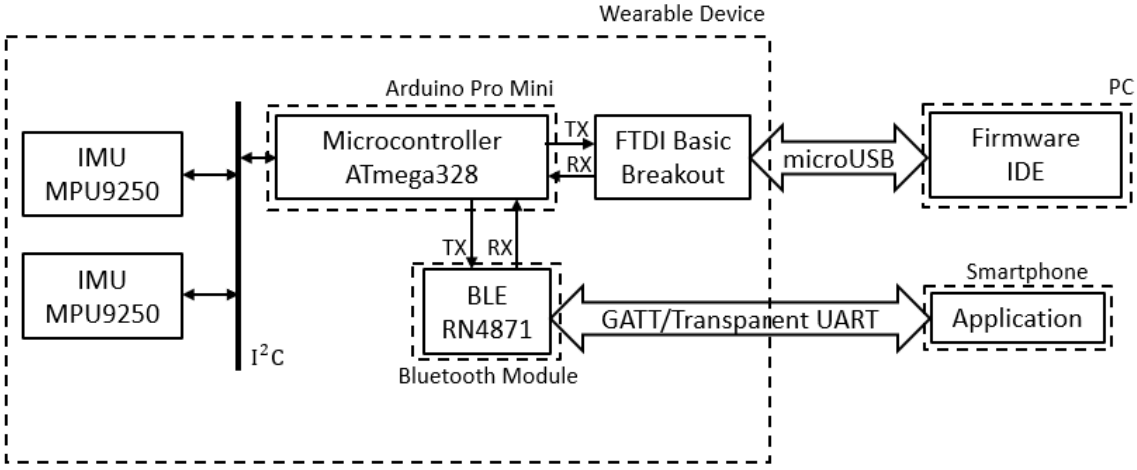

Figure 3.10- Large Overview of the wearable device.

3.3.1.1 - I²C Communication Protocol

This protocol will be used by the two IMUs, which allows multiple slaves to communicate with one or more masters, requiring only two wires to perform the exchange of information [133]. In this way, the I^2C bus is a bidirectional interface that generally uses a microcontroller as master to communicate with slave devices, which are usually sensors. In order to associate the data to each sensor on the I^2C bus, these sensors have a specific address to distinguish them from the others. Generally, data is transmitted through SDA (data signal), while SCL (clock signal) is used to synchronize all data transferred over the I^2C bus [141].

The messages are decomposed in the address frame, where the master defines the slave recipient, and by one or more data frames, where an 8-bit data message is passed from the master to the slave or vice versa. The data is placed in the SDA line only after the SCL goes low and is sampled after the SCL line goes high. Thus, the communication can be detailed in 4 phases: start condition, address frame, data frames and stop condition [142].

The start condition is the phase where the address frame is started, where the master device leaves SCL high and pulls SDA low. This conformation puts all slave devices on alert, indicating that the transmission is about to start.

The address frame is always the first frame in a new communication sequence. Assuming a 7-bit address, the address is clocked out by the most significant bit (MSB) first, and later by the R/W bit indicating whether it will be a read or write operation. The 9th is the ACK/NACK bit. As soon as the first 8 bits of the frame are sent, the receiving device has control over the SDA. If the SDA line is not set to low before the 9th clock pulse, the master device infers that the receiving device did not receive the message or does not know how to process it and decides how to proceed.

After the address frame, the data frame transmission can be started. The master device generates the clock pulses at a regular interval, and the data is placed by the master or the slave in the SDA line (depending on the R/W bit) with an undefined number of data frames.

Finally, the stop condition is performed after sending all data frames with a low to high transition on SDA after a similar transition on SCL, remaining high. All the processes mentioned here are outlined in figure 3.11 [142].

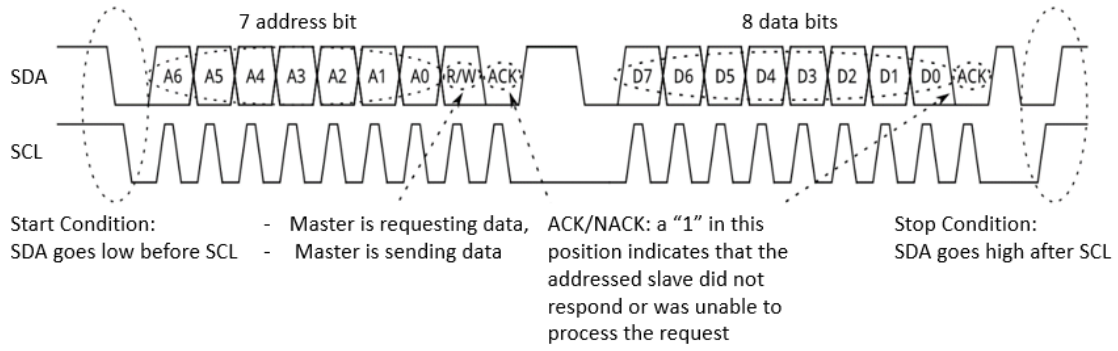

Figure 3.11- Message frame on I^2C [142].

There may still be situations where specifications require a 10-bit address. In this case, the slave address is sent in two frames, in which the first frame is consisted by b11110xyz,

where the letters x, y, and z correspond to the MSB, the bit 8 of the slave address and the R/W bit, respectively. The second frame has the bits 7:0 of the address [142].

3.3.1.2 - Universal Asynchronous Receiver/Transmitter (UART) interface

This is the communication interface between the microprocessor and the Bluetooth module, and by the microprocessor and the FTDI Basic Breakout. A universal asynchronous receiver/transmitter (UART) is a block of hardware responsible for implementing serial communication. A basic UART system allows a robust, moderate-speed and full-duplex communication through two signals, namely the Tx (transmitted serial data) and the Rx (received serial data). In serial communication, data is sent asynchronously, i.e., there is no external clock signal or other timing signal involved between the sender and the receiver. As such, a set of rules/mechanisms are used for robust and error-free data transfer [143].

The first and probably best-known mechanism is the baud rate specification. It is understood as baud rate the speed with which the data is sent over the serial line, usually expressed in bits-per-second (bps). This mechanism only requires that both devices (transmitter and receiver) define the same baud rate. However, although it is known that the higher the baud rate, the faster the data will be sent, there is a set of default values that are used. It is not common to see a baud rate over 115200 bps for common microcontrollers, since higher speeds can translate into errors in the receiver when the clocks and sampling periods cannot keep up.

In addition to the baud rate, there are still some other mechanisms related to frame data, where the synchronization and the parity bits are added as shown in figure 3.12. The data is placed in a block with a size between 5 and 9 bits. However, there is a standard data size of 8 bits (1 byte). After the agreement of the length of the data, the serial devices must agree on the endianness of their data. At this stage, it is decided whether the most-significant bit (msb) or least-significant bit (lsb) is sent first.

The frame has at its ends the synchronization bits that are responsible for marking the beginning and end of a packet. The start is always indicated by an idle data line going from 1 to 0, while the stop bit(s) is the opposite transition. Finally, parity bits are a reasonably simple way of low-level error checking. In the frame, the parity bit has a value of 1 when the sum of the given bits is odd, and 0 when the sum of the bits is even. However, despite being very useful in noisy environments, it causes a decrease in the data reception rate and requires that both devices have implemented error-handling methodologies that sometimes requires the re-sending of data [143].

Figure 3.12- Serial packet architecture [143].

3.3.1.3 - Generic Attribute Profile (GATT)

The generic attribute profile (GATT) is a type of communication used in the new Bluetooth Low Energy (BLE) devices, and it defines how they communicate with each other.

In this case, bidirectional data transmission is performed from concepts called Services and Characteristics that are stored in a generic data protocol named Attribute Protocol (ATT).

An important aspect to consider is that the connections between BLE peripheral (e.g. wearable device) and the central device (e.g. smartphone and tablet) are unique. What it is intended to infer is that a peripheral BLE can only connect to one central device at a time, stop advertising itself, but the central device can be connected to multiple peripherals. The transition of data through GATT follows the concept of server/client relationship. The peripheral device behaves as a server, which holds the ATT lookup data, service and characteristic definitions. Thus, the smartphone or tablet becomes the client and sends the requests to the server, similar to figure 3.13. The connection interval is suggested by the peripheral device, and the central device tries to reconnect at each connection interval to check for new data. This interval is merely indicative, since the central device may not be available at that exact moment [144].

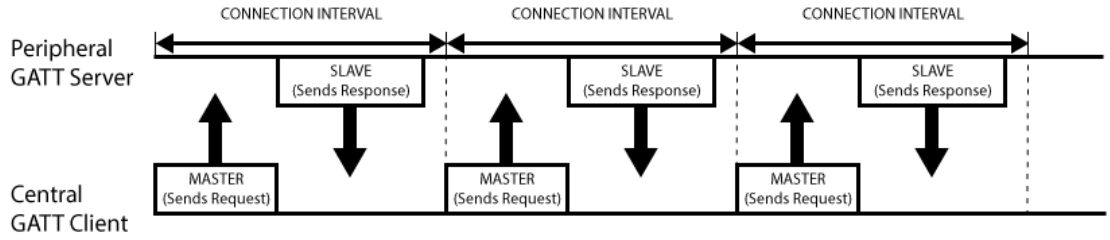

Figure 3.13- Data exchange process between a peripheral (the GATT Server) and a central device (the GATT Client) [144].

As already mentioned, the transactions in BLE devices are based on Profiles, Services and Characteristics that follow the high-level architecture of figure 3.14.

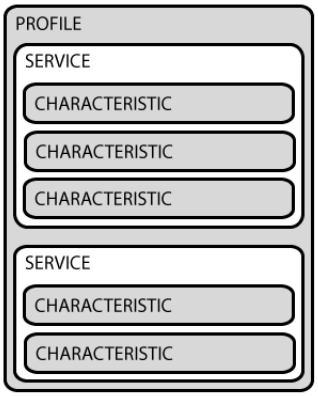

Figure 3.14 - High-level architecture of GATT transactions [144].

In this context, Profiles are a simple pre-defined collection of Services compiled on a particular device, whether they are original or developed specifically for the peripheral device. In turn, Services have the function of separating the data to be transmitted in logic entities, called Characteristics. A service can also be distinguished from the rest through the unique numeric ID called UUID (universally unique identifier), which can consist of 16 bits (officially adopted for BLE Services) or 128 bits (custom services).

Finally, Characteristics are the lowest level concept in GATT transactions and encapsulate the variable or the variable arrays to send. Just as the Services, Characteristics are distinguished by 16-bit or 128-bit pre-defined UUIDs with standard or custom settings

which only the peripheral and central devices understand. Characteristics can be used to send or receive data back to BLE peripheral according to the read or write permissions.

In its simplest state, there is a UART Service with two characteristics, one responsible for the Tx channel and the other Rx, having characteristics of read and write for the central device, respectively. This Service is known as Transparent UART and it is used to simplify serial data transfers over BLE devices. This Service transfer serial data from its UART over a BLE connection, providing an end-to-end data pipe to another Bluetooth device. In particular, the Transparent UART configuration of the BLE used in this work has UUIDs already defined. The Service UUID is set to "49535343-FE7D-4AE5-8FA9-9FAFD205E455" and the UUIDs of the Characteristics and their properties are specified in table 3.1 [145].

Table 3.1- Characteristic Properties [145]

Characteristic Name	UUID	Properties
Transparent UART TX	49535343-1E4D-4BD9-BA61-23C647249616	Notify, Write, Write without response
Transparent UART RX	49535343-8841-43F4-A8D4-ECBE34729BB3	Write, Write without response

With these new versions of BLE devices, there is a new way of organizing and sending the data, with standard Services and Characteristics already aimed for specific types of data, such as the Heart Rate Service and the Heart Rate Measurement [144].

3.3.2- Firmware Developed

Now that the protocols and data structures for communicating have been succinctly explained, it will be emphasized the developed algorithm. The firmware was developed in the Arduino IDE using C/C++ apart from the necessary changes to the original libraries of the manufacturers, which were directly changed from Sublime Text. The activity diagram of figure 3.15 represents the main stages of the algorithm developed.

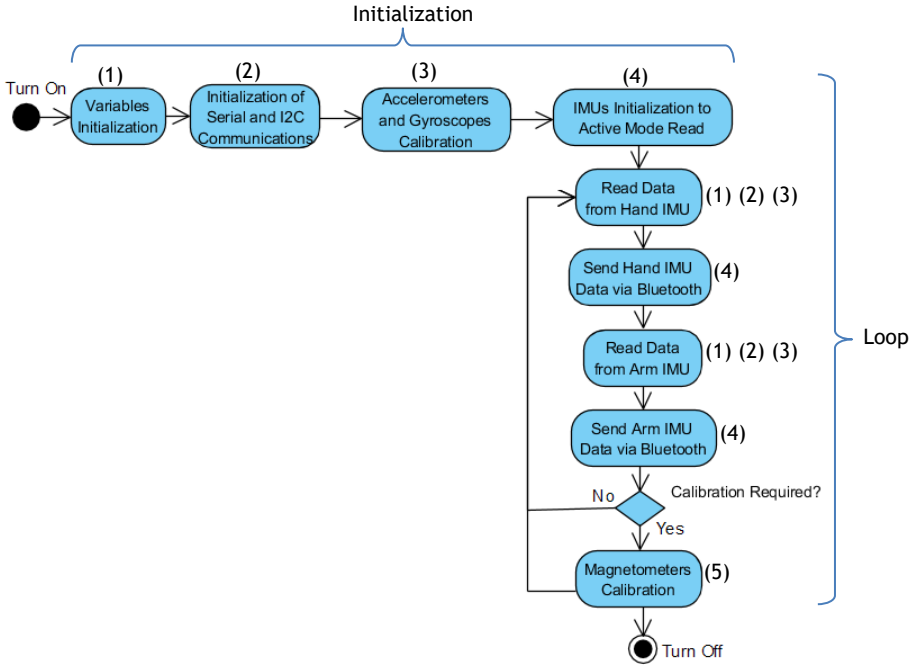

Figure 3.15- Activity diagram of the firmware developed.

The first aspect to consider before the explanation of the developed firmware is related to the BLE. The module has several communication modes, but the transparent UART was chosen for ease of implementation on both sides (peripheral and central). Since the BLE model used is in Data Mode (factory default), it was necessary to develop a small algorithm to communicate with it. The Arduino sends the "$$$" character sequence after 100ms delay before the first "$" to move from Data Mode to Command Mode. Then the local echo is activated by sending the "+" character, followed by the "SS, C0" command to activate the Transparent UART. Finally, the command "R,1" is sent to cause a reboot in the device to remain in Transparent UART. This process only needs to be performed once [145].

The main algorithm developed consists in two essential sections: the initialization where its contents run only once when the Arduino is turned on, and the loop where its composition runs consecutively. In addition, the IDE itself already has several libraries that make it easier to implement.

In this work, it was used library developed by Sparkfun for the MPU9250 that can be found in the original format at [146] and the original library for BLE4871 available at [147]. The first library was developed for one IMU on the I^2C bus, so it was necessary additional methods to assign an address for each object of the implemented class, to allow calibration of the accelerometer regardless of orientation, and to enable and disable the bypass of each IMU.

Since the Arduino Pro Mini has only one Serial communication (UART) and it would be essential to use it to download the firmware and for debugging purposes, it was used a library of the Arduino IDE called SoftwareSerial that allows a second Serial communication to emulate from digital pins [148]. In this way, the Bluetooth module can communicate through the digital pins instead of the fully UART dedicated physical ports. This process was feasible with some changes in the original BLE library. Finally, the reading and writing of the data in the EEPROM were easily performed from the library of the microcontroller manufacturers [149].

3.3.2.1- **Initialization**

The initialization can be described neatly in the following set of steps:

1. In the initial stage of the setup, the Serial and I^2C communications are initialized. Both Serial communications are initialized at a baud rate of 115200 bps for a high data transfer rate and at the limit of the SoftwareSerial capabilities. Even before any processing, the bias values of each magnetometer are read from the EEPROM.

2. The first test to verify that the I^2C communication was correctly performed for each IMU is to confirm that the WHO_AM_I from slave register is 0x71. With this simple handshake, a message is sent through the FTDI Basic Breakout Serial where it is indicated whether the connection was successful or not. In this way, the source of the problem is easily detected. If both IMUs successfully pass this stage, the initialization and calibration processes begin.

3. After the connection, a simple calibration for the accelerometers and gyroscopes of each IMU is performed. This process takes only a few seconds, but the sensors must be immobilized to calculate the bias (average of the at-rest readings) for each axis of each sensor. The magnetometers are calibrated only when required because the process is

more complex, time-consuming and requires some specific movements. This process starts with the reset of the devices with the default settings, i.e., the full-scale accelerometer at ±2g and gyroscope at ±250dps. Thereafter, several samples are collected for each of the accelerometers and each of the gyroscopes. The accelerometer reading has the gravity components that must be removed before calculating the bias. This value is calculated for each axis of each sensor from the low-pass filter:

$$gravity = \alpha * gravity + (1 - \alpha) * acc\_temp \qquad (3.1)$$

where,
α is set to 0.9 and acc_temp corresponds to the current measurement.

After subtracting the gravity estimation to the current value in x, y and z component, the value is divided by the sensitivity (16384 LSB/g) and contributes to the bias average. The gyroscope calibration is simplified since there are no extra components. The read value is divided by the sensitivity (131 LSB/degrees/sec) and added to the bias average. The calculated offset values are used for subtraction at each iteration of the loop. The raw values can be loaded into the accelerometer and gyro bias registers, but there is an increase in the difficulty of debugging during the development.

4. After calibration, the device is initialized to active mode read. The accelerometer was set with the full-scale range of ± 2g, while the gyroscope was set to ± 2000 °/s (dps). These intervals were sealed to have specifications similar to the MoMo used in the iHandU project. It was also detected that for a full-scale range standard of ± 250 °/s in gyroscope, the sensor has saturation in some fast movements.

5. The initialization of each magnetometer is performed sequentially for each IMU. This process requires the bypass to be enabled by changing the bit1 to 1 of the register INT_PIN_CFG with address 0x37. The factory calibration values for each magnetometer axis are extracted and the magnetometer is set to the continuous mode data acquisition with a single full-scale range of ± 4800μT. Finally, the bypass is disabled, and the process is repeated for the other IMU.

3.3.2.2- **Loop**

The loop was developed to collect, process and send data from each of the IMUs sequentially, i.e., the hand's IMU first and then the arm's IMU.

1. Initially, the raw data values of the accelerometer contained in the first IMU are read and converted to g-forces from equation:

$$acc = raw_{acc} * \frac{2}{32768} - bias_{acc} \quad . \quad (3.2)$$

2. Similarly, the raw data registers of the gyroscope are read and converted to degrees per second from equation:

$$gyr = raw_{gyr} * \frac{2000}{32768} - bias_{gyr} \quad . (3.3)$$

3. Once again, the magnetometer raw data is read after enabling the bypass. The computation of the milliGauss value for each axis considering factory calibration and user environmental corrections is given by:

$$mag = raw_{mag} * \frac{10*4912}{32760} * factoryBias_{mag} - EEPROMBias_{mag} \quad . \quad (3.4)$$

4. After acquiring the data from the first IMU (hand's IMU), these values are sent by Bluetooth through transparent UART with the following configuration:

$$* Acc_x; Acc_y; Acc_z; Gyr_x; Gyr_y; Gyr_z; Mag_x; Mag_y; Mag_z\# \quad , \quad (3.5)$$

where * and # represent the initialization and termination character, respectively. The loop processes referred until here occur again for the second IMU (arm's IMU), but the data is packaged to send as follows:

$$+Acc_x; Acc_y; Acc_z; Gyr_x; Gyr_y; Gyr_z; Mag_x; Mag_y; Mag_z\# \quad , \quad (3.6)$$

where + and # represent the initialization and termination character, respectively. In this way, the processing by the following layers becomes simplified since the initialization character is distinct for each IMU.

5. The magnetometer calibration process is performed when the "cal" character sequence is found in the input buffer of the Bluetooth. As soon as this sequence is detected by the Arduino, the message "ACK1" is sent back to indicate that the wearable device started the magnetometer calibration phase. The bypass of the first IMU is enabled and the calibration lasts 19 seconds, with 15 seconds of sampling [150].

   This calibration provides better sensor accuracy through environmental corrections by reducing the effect of non-ideal response surfaces. The ideal response surface for a triaxial magnetometer is a sphere centered at the 3D origin, which means that the value must be equivalent when each of the magnetometer axes is oriented towards a given magnetic field.

   This problem is mostly caused by hard iron biases and the implemented solution collects the bunch of the magnetometer data as the sensor is slowly moved in a figure eight pattern and stores the maximum and minimum of each axes. After the average computation between the maximum and minimum of each axis, the hard iron correction bias is given by:

$$environmentBias = averageBias_{mag} * \frac{10*4912}{32760} * factoryBias_{mag} \quad (3.7)$$

   After this process, the message "ACK2" is sent by Bluetooth, meaning that the calibration of the hand's IMU has been completed and the same processing will be applied to the arm's IMU. In the end, the message "ACK3" is sent stating that the calibration has ended and the computed bias for each axis of each magnetometer is stored in the EEPROM, restarting a new loop iteration.

The set of processes referred in the loop section occur at a frequency of ≈22Hz, except when magnetometers calibration is required. These processes use 67% of the storage, and the global variables use 69% of the dynamic memory. During the development it was necessary to review the whole code in order to make the code lighter for the Arduino, reaching the referred values. One of the most notable cases is the sequentially reading and transmission of data for each IMU. This process has been chosen to recycle the variables and decrease the amount of data in the Bluetooth buffer at a time, thus minimizing the data loss. Therefore, it will be difficult to add more functionalities without changing the microprocessor, since occupancy of the last quarter of memory can cause instability.

3.4 - Sensor Fusion Algorithm

The next step in the processing of sensor data involves the integration of the fusion algorithms in the smartphone. Both Madgwick and Mahony Filters have constant gains that must be studied to provide the best accuracy possible. As such, it becomes necessary to perform an offline study to apply the final version of the algorithm with better performance. After the wearable device becomes properly calibrated, the data was sent via Bluetooth to the Android Application described in the next section. The data was directly saved to a text file and transferred to the computer. For this analysis, 3 datasets were developed to test each of the Tait-Bryan angles individually. For each angle relative movements were performed of approximately 30°, 60° and 90° with return to the initial position at each iteration (0° -> 30° -> 0° -> 60° -> 0° -> 90° -> 0°). Each static position is maintained for 15 seconds. The values were acquired with the hardware placed on the rotating arm of the Bosch angle gauge (figure 3.16), which indicates the angle between the two arms with one decimal place (measurement accuracy of 0.2°). The value read by the Bosch sensor was recorded for ground truth comparison to the IMU measurements. In this study, only the data of an IMU was used since they are equal models and would give similar results. In this case, it was used the IMU of the hand.

Figure 3.16 - IMUs placed in the Bosch sensor (model PAM 220).

The algorithm developed was written in R using the RStudio and the respective activity diagram is represented in figure 3.17. Although there are already ideal values for the constant gains of each complementary filters tested, it is necessary to study the best constants that translate into an output with a smaller error when compared to ground truth [116, 127, 129].

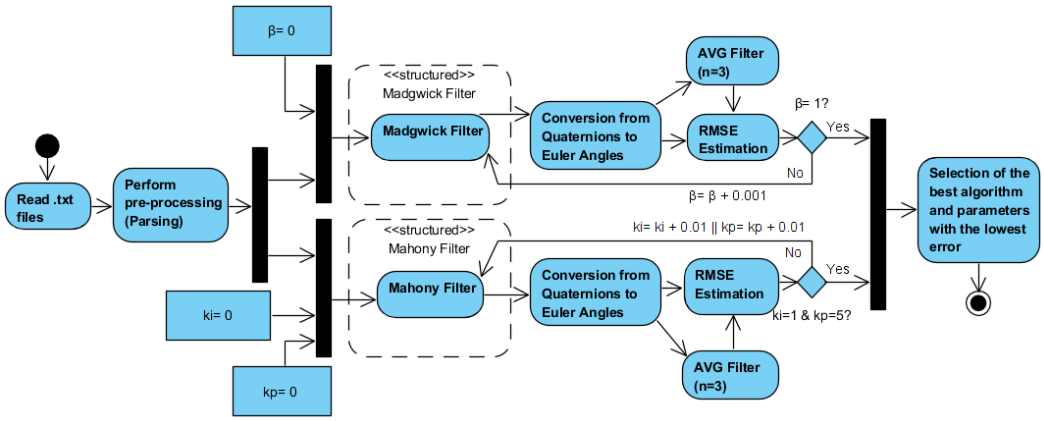

Figure 3.17 - Offline Algorithm Activity Diagram.

The first step of the algorithm is to read the three acquired text files. Afterward, the data in each file is parsed, saving only the data of the distal IMU. The datasets data are then submitted to the two fusion algorithms already implemented in the "RAHRS" Package [151]. This is an iterative process for each dataset, where the two filters with different constant gains are tested, and the output of each iteration is converted from quaternion to Tait-Bryan angles using the z-y-x convention.

The Madgwick Filter was tested with ß values between 0 and 1 with an increment of 0.001. As for the Mahony Filter, it was tested with all combinations of Ki values between 0 and 1 with increments of 0.01 with Kp ranging from 0 to 5 with increments of the same order of magnitude as the previous one. The range of these values were defined based on the existing literature and on practical experience, since the minimum error values should not be obtained in the maximum constant gains tested [116, 130]. The sampling time was set at a constant interval of 0.045 seconds, assuming that all samples have reached the smartphone.

The constant offsets are removed from the measured angles originated by the difficulty of placing at an exact 0° in the base position (the measured value is in relation to the NED coordinate system). The offset is computed by the average of the 100 random values at each 0° step. The points corresponding to the initial and final 10 seconds are removed from these data. In the initial phase, constant gains make the filter respond at different rates, an aspect considered acceptable that should not influence the conclusions of the study. On the other hand, in the final phase there may be oscillation related to the movements on completion of the acquisition.

After processing the output with the steps referred to above, each angle of interest is compared with that corresponding ground truth taken from the Bosch sensor. This comparison was performed through the root-mean-square error (RMSE) value, where it is tested against the original values and after a moving average filter of size 3, in an attempt to improve the result. A larger window could be used, but with a frequency of ≈ 22Hz and with a real-time analysis perspective it would be an impractical process. The RMSE values are saved with reference to the constant gain used, and a new iteration is started.

As an example, the graphs of figure 3.18 illustrate the three datasets collected. In this case, the values are the Madgwick Filter output for a ß of 0.106 (value chosen in the study) before any processing. In these graphs, it is verified that for each dataset acquired the three Tait-Bryan angles are calculated, but only one of them was really analyzed.

From these graphs some conclusions can be drawn. Firstly, as already mentioned, there is an initial time for the angles to reach the measured value, depending on the constant gains.

Secondly, it is possible to verify the good behaviour of the IMU and the fusion algorithm, since the variation of an angle scarcely anything affects the adjacent ones. Finally, for the dataset in which the pitch is analyzed, the existence of the gimbal lock at 90° is verified, where the roll and the yaw lose stability.

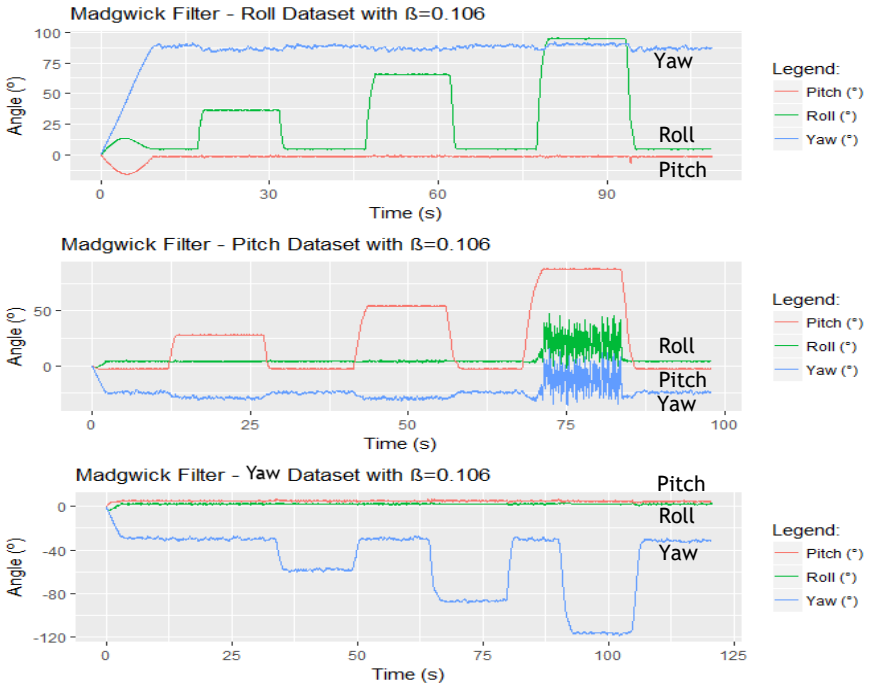

Figure 3.18 - Output of the acquired datasets for Madgwick Filter with ß of 0.106.

Thus, the graphs of figure 3.19 illustrate the RMSE values as a function of ß in the Madgwick Filter for the three angles acquired independently. In these graphs it is possible to verify that the filter has minimum errors below 2°, reaching the approximate 1.33° in roll, 1.56° in pitch and 1.97° in yaw (indicated in the graphs) for its best constant gain ß. It is possible to verify that for the moving average, the values improve in the 2^{nd}/ 3^{rd} decimal place, which are not significant for the requirements of this work.

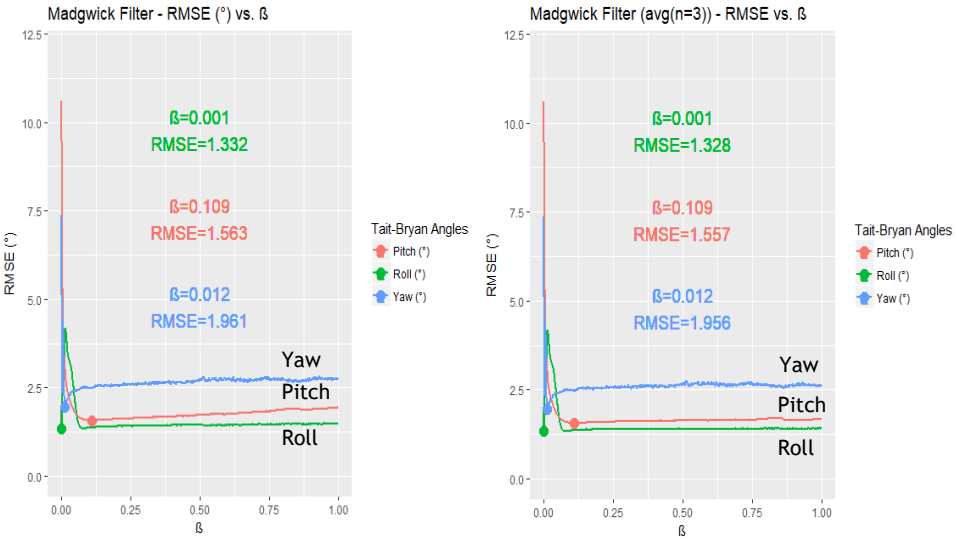

Figure 3.19 - RMSE as a function of ß for the original output of the Madgwick filter and after the moving average filter.

Similarly, the same type of analysis was performed for the Mahony Filter. The results are shown for each angle in the 3D graphs of figure 3.20 and 3.21. The PI filter completes its results with a minimum RMSE of approximately 1.77° in roll, 2.93° in pitch and 2.14° in yaw. Once again, comparing the original values with the values after the average filtering reveals an insignificant difference for the project.

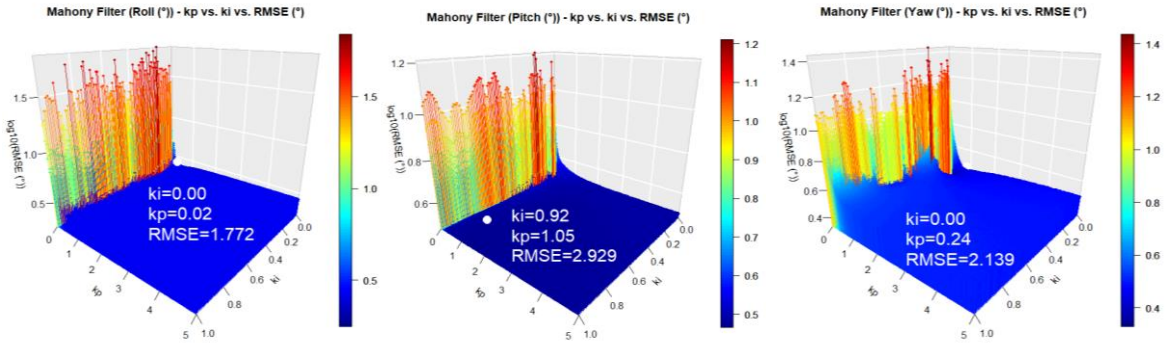

Figure 3.20 - RMSE as a function of Ki and Kp for the original output of the Mahony filter.

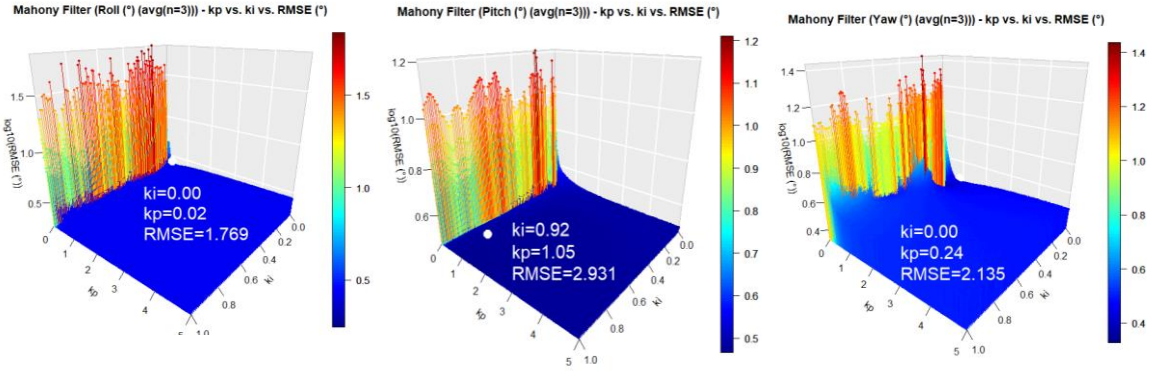

Figure 3.21- RMSE as a function of Ki and Kp for the original output of the Mahony filter after the moving average filter.

The results up to this stage are shown in table 3.2. Each value shown here was independently calculated from the others.

Table 3.2- Results obtained by the Sensor Fusion Algorithms.

	Roll (RMSE (°))	Pitch (RMSE (°))	Yaw (RMSE (°))
Magwick Filter	1.332 (ß=0.001)	1.563 (ß=0.109)	1.961 (ß=0.012)
Madwick Filter (average filter)	1.328 (ß=0.001)	1.557 (ß=0.109)	1.956 (ß=0.012)
Mahony Filter	1.772 (ki=0.00 & kp=0.02)	2.929 (ki=0.92 & kp=1.05)	2.139 (ki=0.00 & kp=0.24)
Mahony Filter (average filter)	1.769 (ki=0.00 & kp=0.02)	2.931 (ki=0.92 & kp=1.05)	2.135 (ki=0.00 & kp=0.24)

For the analysis of the results above, it is evident the preference for the Madgwick Filter instead of the Mahony Filter which produces inferior results and creates an increased difficulty finding global Ki and Kp values. After choosing Madgwick Filter, it is necessary to find a global constant gain ß. For this purpose, several possible solutions were considered as the average of the best three ß or feed three filters constantly with each ß and collected

only the values of the desired angle. However, the first is a more blind process where the average may not really be the best global ß with lower RMSE values, and the second process increases the computational cost.

At this point, a chart was developed (figure 3.22), where each point represents a ß and each axis represents the value of the RMSE obtained in each dataset. Consequently, the closest point to the origin of the graph corresponds to the best global ß (calculated from the Euclidean distance), achieving a weighted loss in the value of RMSE. This calculation led to a global value for the ideal constant gain of 0.106, with RMSE values of approximately 1.36° in roll, 1.56° in pitch and 2.47° in yaw. These values are all higher than in an ideal independent ß, but the differences are minimal except for the yaw, where the most prominent occurs.

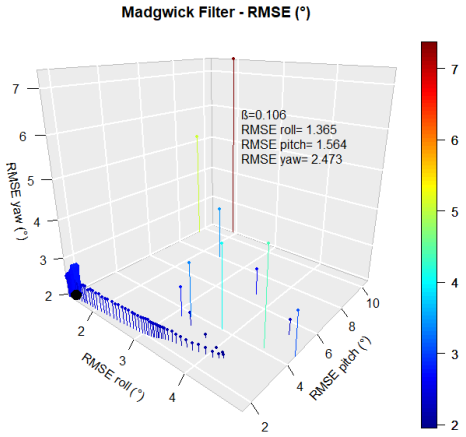

Figure 3.22 - Relation between the several RMSE values for a given ß.

Now that the fusion algorithm and the constant gain have been defined, the visual results between the acquired values and the ground truth can be visualized in figure 3.23.

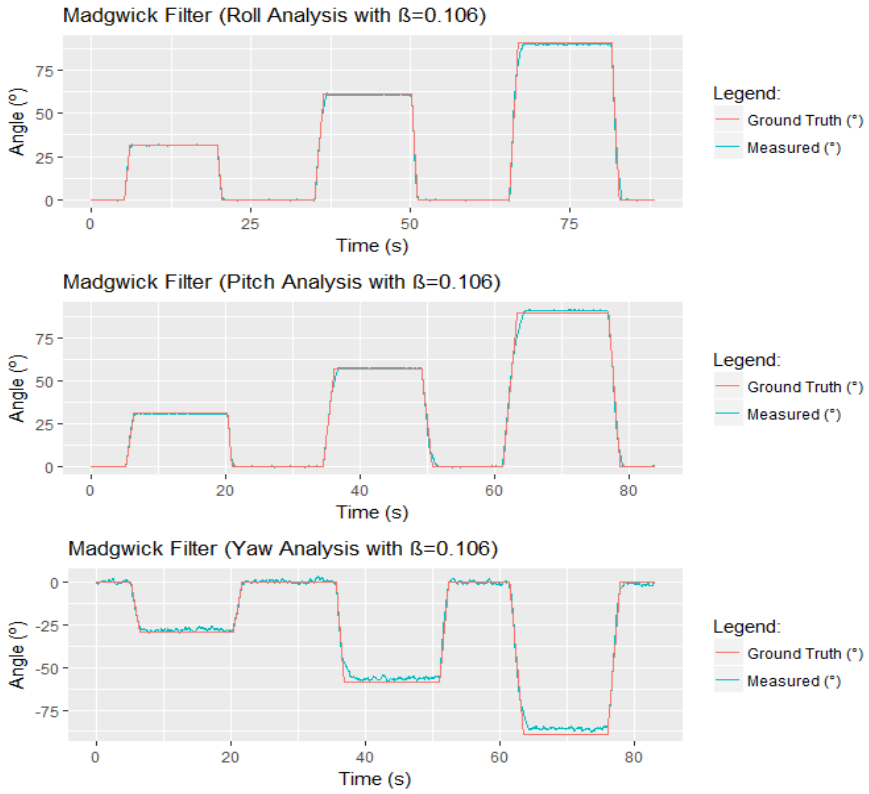

Figure 3.23- Estimated/measured angles vs. ground truth for roll, pitch and yaw.

The graphs show the clear similarity between the acquired angles and the ground truth. The roll and pitch compatibility are almost excellent with some exceptions in the transition between steps, where it is found a more curved stabilization than in the ground truth. These variations affect the results but will hardly be eliminated in the methodology used, since the movements have some imprecisions when compared to a linear transition. The yaw has a more significant difference than the previous ones, mainly responsible for the noise added by the nature and fidelity of the magnetometer. In addition, it is also verified that this angle presents values slightly different from the ground truth in the steps. This can be explained by a higher magnetometer intervention and by the increased difficulty of its acquisition with the Bosch sensor.

In a more in-depth analysis, the sets of values illustrated in the previous figure are represented in the respective Bland-Altman plots. These plots represent the agreement between two quantitative measurements. The Bland Altman analysis results in a xy scatter plot, in which the x-axis represents the mean and y-axis the difference between two paired measurements. The visual analysis of these graphs allows the evaluation of the global agreement between the two measurements, through the mean difference and the interval between ± 1.96 of the standard deviation (SD) of the differences, with a confidence interval (CI) of 95% if the differences are normally distributed (Gaussian) [152].

The plots of figure 3.24 show a pattern of lines centered in each step (0°, 30°, 60°, 90°) with a special concentration of points in the mean of the differences, being this value close to 0° for the roll and pitch, exceeding the unit value only in yaw. It is also possible to extract that the sensors have reasonably linear values when stagnated since the points beyond the 95% confidence interval are measurements in transition phases, whose differences are visible in figure 3.23. These differences are easily detectable mainly in the arrival and departure of the steps, where they are compared with linear movements. For this study, the graphs do not allow the identification of large constant discrepancies in the differences since the biggest errors are found in the comparison between rise and fall between steps, respectively.

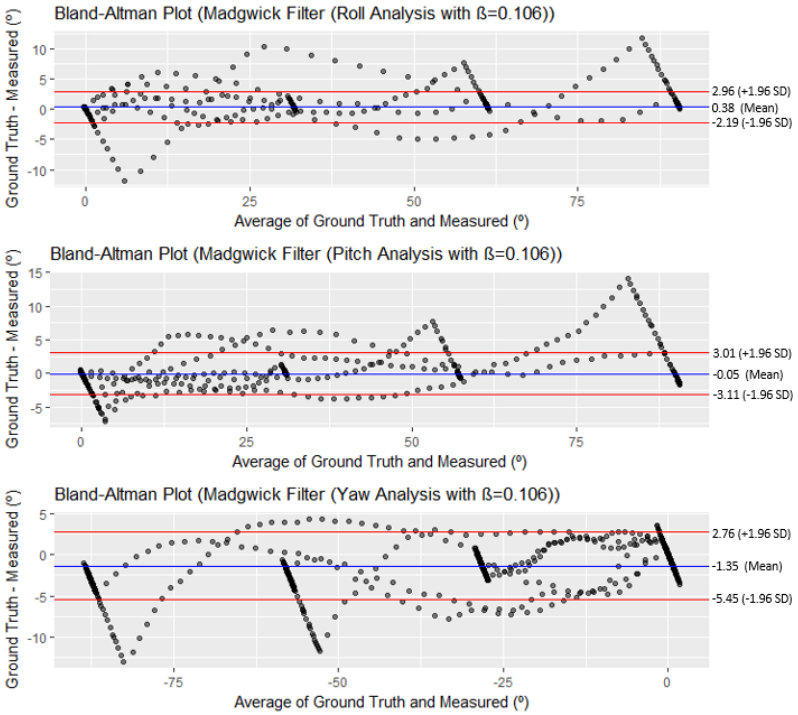

Figure 3.24- Bland-Altman Plots for roll, pitch and yaw.

Given all the data from the Bland-Atman Plots, it is concluded that to close this study properly, the RMSE should be re-computed only for the steps, using the same selected filter and constant gain. By repeating the chosen algorithm and calculating the RMSE value just for the 10 central seconds of each step (values contained in the red rectangles of figure 3.25), only the errors associated to the sensor are obtained and most points outside the confidence interval are eliminated.

Just with these sections an RMSE of 0.48° for roll, 0.60° for pitch and 2.09° for yaw was reached. These values demonstrate the excellent performance of the chosen algorithm, presenting values much more satisfactory than the entire analysis of each dataset.

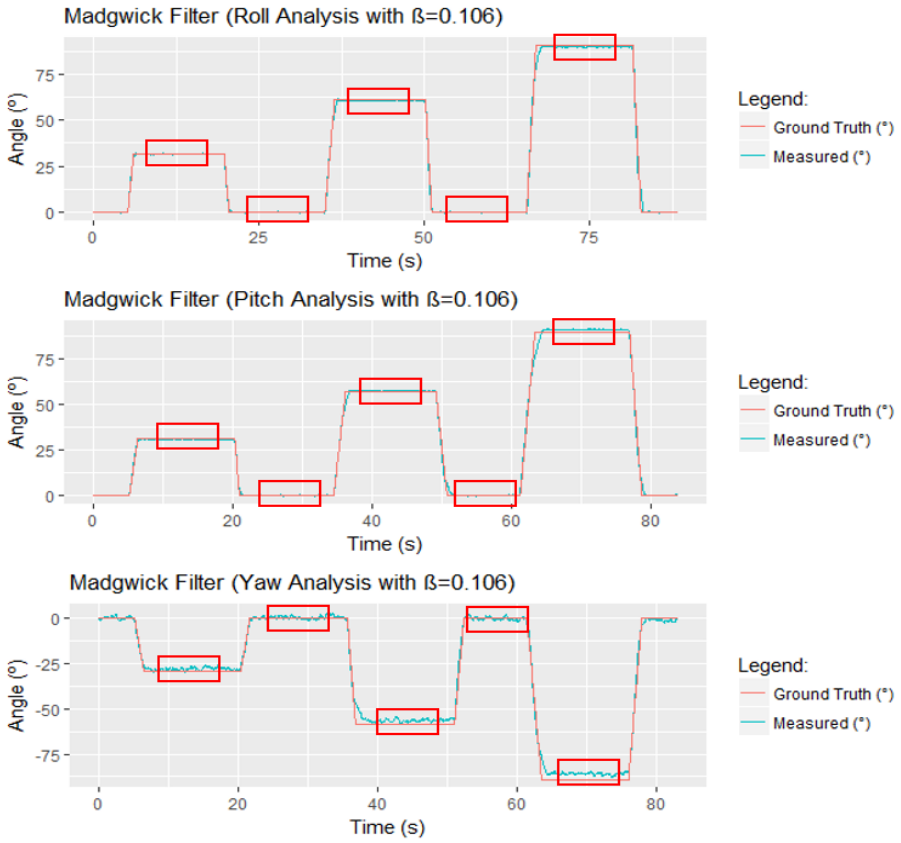

Figure 3.25- RMSE analysis for each step.

As before, the respective Bland-Altman plots for this set of values were also re-computed, shown in figure 3.26. By comparison with the previous graphs, it is found that the mean value of the differences did not improve significantly. On the other hand, the confidence interval decreased drastically, although values were kept higher at yaw angle as expected for the reasons already mentioned. The in-line patterns made by the analyzed points of each step are smaller in size and have a greater slope compared to previously, thus proving the accuracy of the prototype. For the axes of the graphs and considering that now only the evaluation of static measurements, the size of the lines made by the points and the corresponding slope is directly related to the characteristic noise of the type of sensors used in this work and the processing of the fusion algorithm.

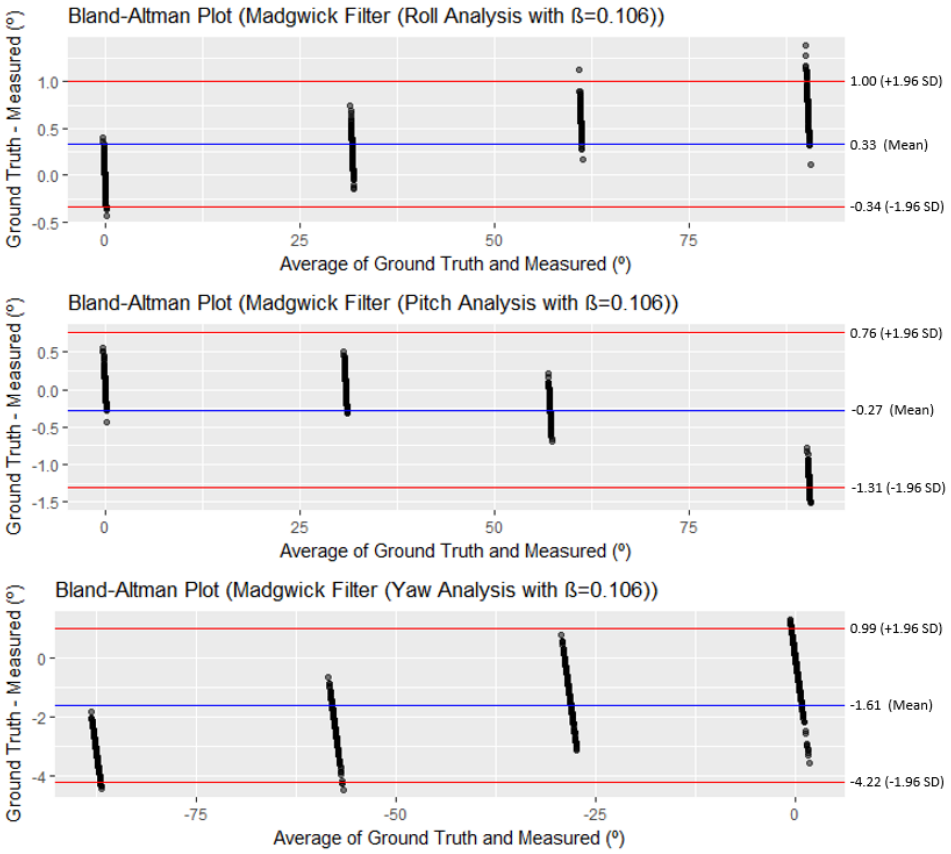

Figure 3.26- Bland-Altman Plots for roll, pitch and yaw in each step.

Now that the study has revealed the best algorithm and constant gain to implement (Madgwick filter with ß= 0.106), it will be explained the development and features of the Android application.

3.5 - Android Application

For this dissertation, it was developed an Android application to communicate directly with the wearable device and the web service behaving as the central element of the system and occupying the second tier of the Wearable Health Systems architecture. The application was implemented in Android Studio (official integrated development environment), using Java as a back-end language and XML to develop the interfaces and layouts.

After collecting the main requirements for the application, they were transferred to the use cases diagram of figure 3.27. This topic is divided by the main features provided to the user and sets of interfaces (activities in Android) where it will be explained the processing, working principles and data flows.

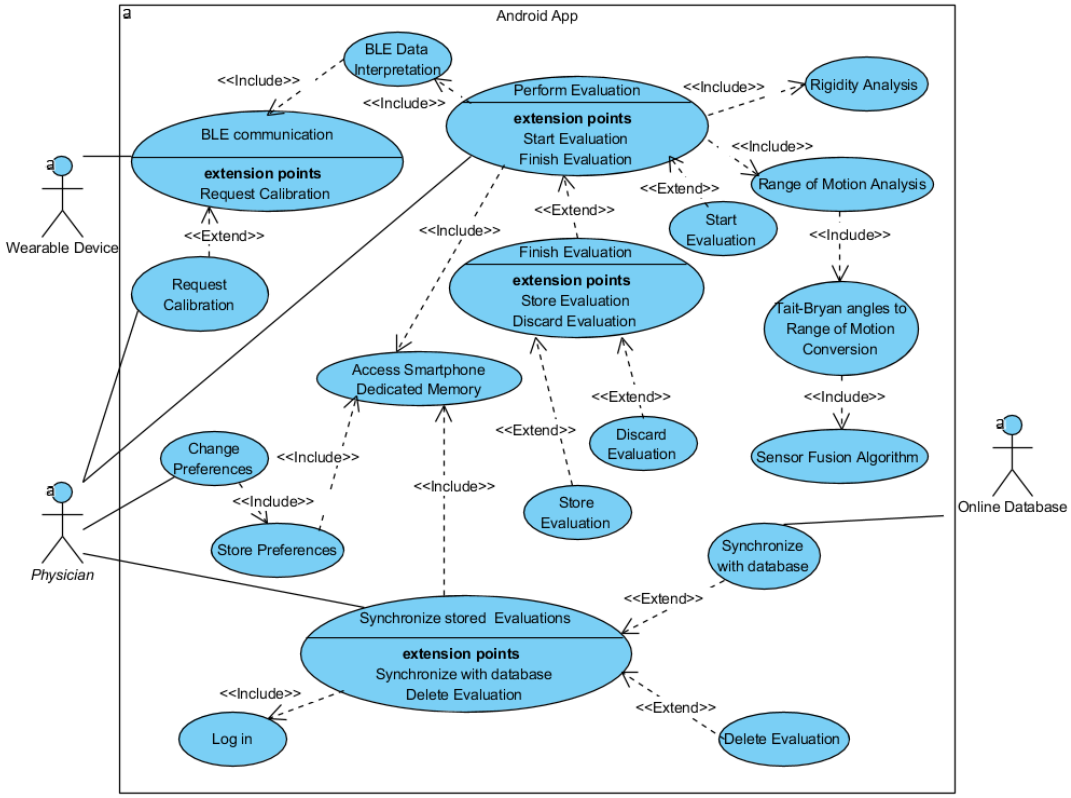

Figure 3.27- Use cases diagram of the Android application.

3.5.1- Welcome Interface

The Android application has an intro screen shown in figure 3.28. This interface is quite rudimentary and only indicates the name of the project, the icon chosen to represent the project and the logo of the associated entity. This screen lasts only 3 seconds and afterwards, it automatically switches to the main menu.

Figure 3.28- Welcome Interface.

3.5.2- Main Menu

After the first screen, the main menu shown in figure 3.29 appears. This menu allows the user to select the desired activity, which can start the evaluation, calibrate the wearable device, change the preferences and synchronize the performed evaluation with the server. On the first use, the user is requested permission to read and write in external memory since it is necessary to have access to save some information to the system non-volatile memory as it will be described in detail on the evaluation interface. Still in the first time, the default range of the maximum angles to measure are saved to ensure that the values exist to start the evaluation. The values are stored through a library called TinyDB that provides a simplified interface with Android's Shared Preferences to store data in memory with an associated key [153]. The values can be replaced at any time in the preferences interface.

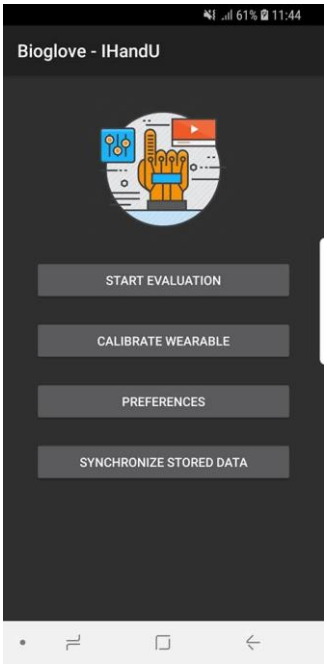

Figure 3.29 - Main menu interface.

3.5.3- Evaluation Interface

The evaluation interface becomes one of the most important interfaces in the developed Android application since it actually allows the user to obtain the absolute measurements of the range of motion as well as the rigidity improvement in the wrist. Before the main interface, the user needs to define which Bluetooth device is intended to connect through the interface of figure 3.30 (A). This interface is shared with the calibration option, in which the main menu sends the following activity to execute.

This first activity scans the devices (using the Android BluetoothLeScanner) for 10 seconds and as soon as they are found, the devices are placed on the list with the name and the respective MAC address. After the 10 seconds, it is possible to re-scan by clicking the upper right button. As soon as the user selects a device, the evaluation activity starts using the chosen Bluetooth name and MAC address. If the Bluetooth on the smartphone is turned off at the beginning of the first activity, a dialog initiated by Android itself will appear, where the user must give consent to switch it on (figure 3.30(B)).

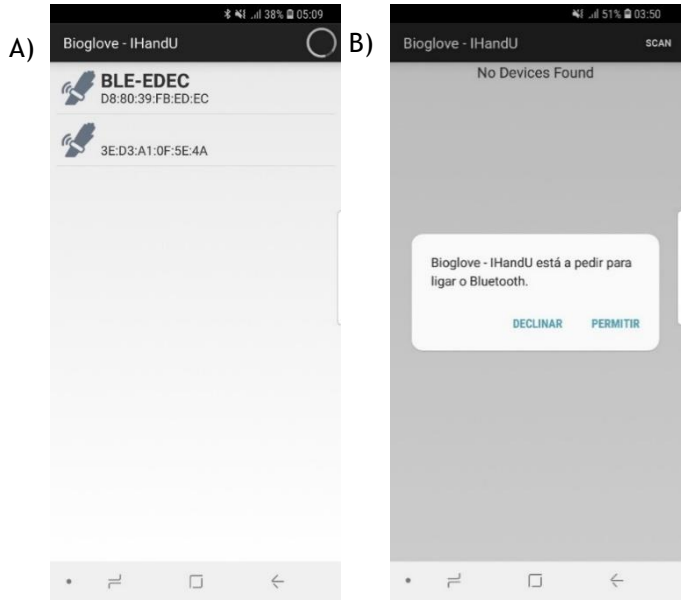

Figure 3.30 - Interface to select the Bluetooth device to connect. The figure represents the selection interface in A, and the request to connect the Bluetooth in B.

After arriving at the evaluation activity, the label with the state of the Bluetooth connection is placed as "Connecting" and all buttons are disabled except for the "Start Evaluation" button (figure 3.31 (A)). For a few seconds, the Android service in the background starts to establish the Bluetooth connection with the device/MAC address selected. The service is bonded to the activity by verifying that the GATT profile available through Bluetooth has the same expected UUIDs for the Service and Characteristics, which is specified by the Transparent UART of the BLE already defined in the Firmware section. If there is UUIDs agreement the connection is made, and the evaluation activity communicates with the wearable device through the Android Service and illustrates the "Connected" label. On the other hand, assuming there is no compatibility during the 5-second attempt, the state becomes "Disconnected" and an error message is sent, forcing it to re-scan (figure 3.31 (B)). These UUIDs specified by the BLE guarantee the application specificity in which only devices with these identifiers can connect.

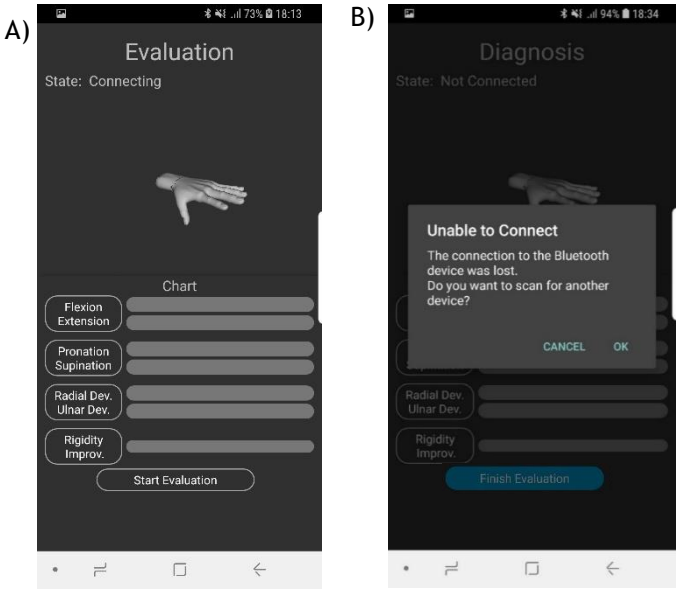

Figure 3.31 - Evaluation Interface. The figure represents the main interface in A, and the connection failure notification in B.

Once the connection is made, the evaluation can start as soon as the user clicks the "Start Evaluation" button. The click starts a new dialog where the user inserts the limb of the wrist to be analyzed, the position of the sensors (placed on the top or bottom of the hand) and the patient ID (figure 3.32). These options allow the user to adjust the data processing so that the left and right limbs can be evaluated, and the sensors can be placed either on the face of the hand (position in figure 3.9) or on the palm. As soon as the "OK" dialog is selected, the date and time of the evaluation are saved and a new file with the name in the format "patientID ddmmyyyy hhmmss" is created in the "Bioglove-iHandU" directory of the smartphone's internal memory. From now on the evaluation starts and all the buttons are enabled.

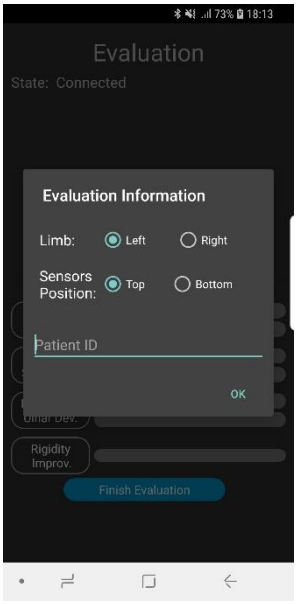

Figure 3.32- Evaluation Information Dialog.

The interface also has a 3D animation where it is possible to visualize in real-time the movement that is being performed by the patient. The animation is performed from a lightweight library/framework called Min3D developed from Java and OpenGL ES, which enables a simplified way to implement object movements in a 3D environment [154]. This small library requires the orientation of the arm and hand independently since it does not allow articulated objects. The 3D model was taken from [155] and changed in Blender (professional, free and open-source 3D computer graphics software) to split the object into two pieces (arm and hand) and to generate the model for both limbs. Thus, the displayed model is loaded from a .obj file according to the limb selected by the user (figure 3.33 (A)).

The range of motion is evaluated in pairs as they are antagonistic (flexion/extension, pronation/supination, and radial/ulnar deviation), except the wrist rigidity improvement. When required by their respective buttons, the calculated values are shown in real time on the bars in front of each button but can also be viewed on the graph that covers the 3D animation when the word "Chart" is slid up (figure 3.33 (B)). The graph developed through the Graphview library allows the visualization of the angles for the required movements and the angular velocity used to evaluate the wrist rigidity improvement as it will be explained below [156].

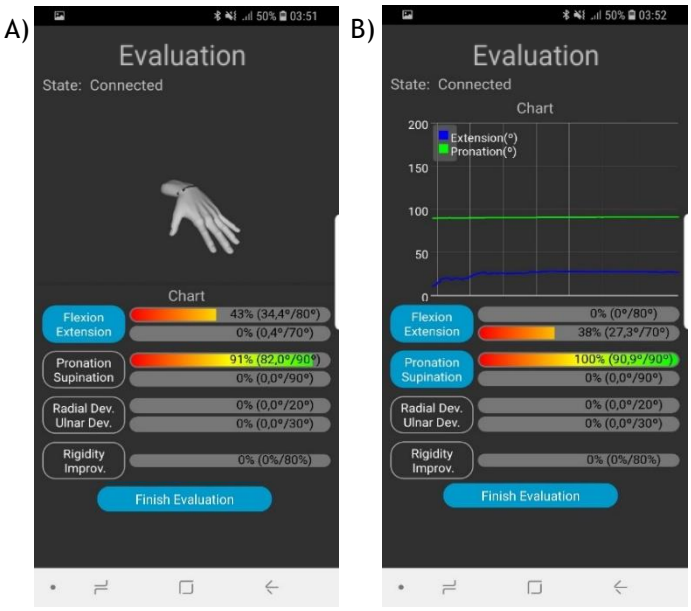

Figure 3.33 - Interface with active evaluation.

After a brief explanation of the interface, the data processing in back-end will be emphasized. Whenever the service implemented in Android receives the notification or indication with a new value in the characteristic of the BLE, a BroadcastReceiver handles the event fired by the service and sends the received string to a handler where the data is processed.

The received string does not always match the full string sent by the wearable, meaning that it may be necessary to save the received string and append in the next iteration. This process occurs while the string does not have one of the initialization characters (* or +) and the termination character (#) defined in firmware. Likewise, if the received string contains data after the "#" character, it is separated, and the second substring is used to append in the next iteration. When the string has one of the initialization characters at index 0 and the end character at the last index, it is ready to be processed.

The first step makes sure that string is complete in your content. To achieve this, it is verified if 8 semicolons are separating the data, which if it does not exist the string is automatically discarded. After this step, the initialization and finalization characters are removed, and the values are parsed, updating the current data array of the respective IMU.

According to the data, the integration time is calculated by the time difference with the last complete data received from the respective IMU. For each IMU data, a Madgwick Filter is applied with β of 0.106 (value obtained in R). Depending on the data received, the values and the integration time are inserted into the corresponding filter and the estimation is updated. The quaternion output is transformed into Tait-Bryan angles from the equations described in state of the art, allowing the change to range of motion. In this phase and after estimation of the angles for the received data, the 9 values of each IMU together with the Tait-Bryan angles are stored in the file as:

$$*Acc_x;Acc_y;Acc_z;Gyr_x;Gyr_y;Gyr_z;Mag_x;Mag_y;Mag_z\#roll;pitch;yaw\# \quad (3.8)$$

,or

$$+Acc_x;Acc_y;Acc_z;Gyr_x;Gyr_y;Gyr_z;Mag_x;Mag_y;Mag_z\#roll;pitch;yaw\# \; . \quad (3.9)$$

Conversion from Tait-Bryan angles to range of motion is only performed if the corresponding button is active. However, the Tait-Bryan angles have some particularities that must be understood. The figure 3.34 shows the output of roll, pitch and yaw angles in the x-y-z convention for a rotation from 0° to 360°. These graphs now represented prove that the conversion to range of motion is not that straightforward and requires further processing.

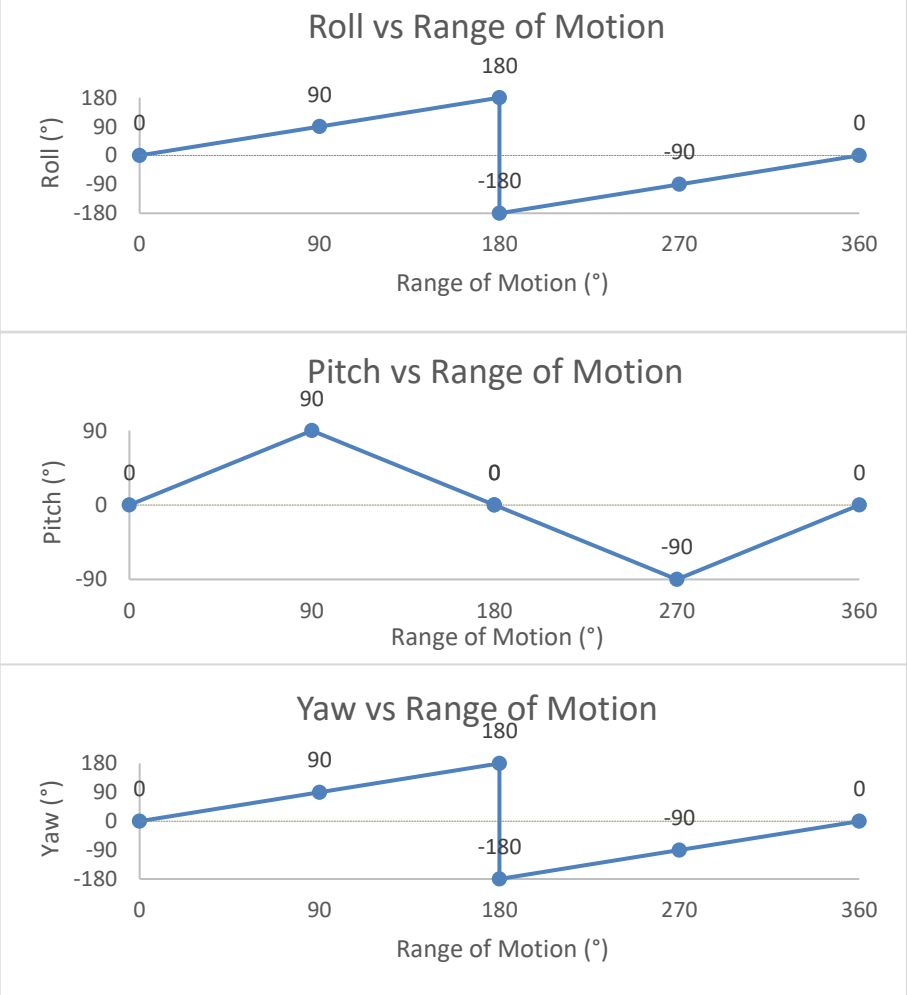

Figure 3.34 - Tait-Bryan angles vs range of motion.

3.5.3.1- Flexion/Extension Evaluation

The first button allows the evaluation of the flexion and extension through the roll angles from the hand and arm, given the orientation of the sensors. The flexion/extension is calculated by the difference between the angles as:

$$diff = armRoll - handRoll\ . \qquad (3.10)$$

In this evaluation, both left and right hand do not require different calculations. Even when the sensors are placed in the palm of the hand, simply reverse the signal of the subtraction to calculate the same way as when placed on the face of the hand. In flexion/extension as well as others permissible movements, the 360° of movement was considered to increase the fidelity of the system, even though it is not common in clinical evaluations.

The ideal and most used case in practice (figure 3.35), it is verified by the first graph of figure 3.34 that if the hand is completely horizontal and both IMUs are parallel the value of the difference will be approximately 0°. If the evaluation is performed in this position, there is no concern about the 180° roll discontinuity since physiologically it is not possible to achieve such a high amplitude. Thus, if the subtraction of the two values is negative (assuming the interval between 0° and -180°), the movement is classified an extension and the simple subtraction illustrates the result of the real-time range. Considering the same horizontal position, if the value is positive (assuming the interval between 0° and 180°), the movement is labelled as a flexion and the result is given by the simple subtraction of the two angles.

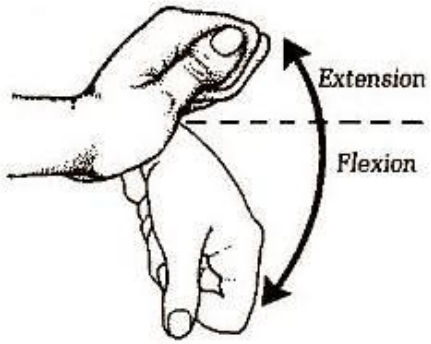

Figure 3.35- Ideal flexion/extension position used in clinical evaluation [157].

When the evaluation is not carried out in the original position it is necessary to take into account the discontinuity at -180°/180°. Although in practice this implies going with the arm beyond the vertical position which does not make much sense, from the point of view of the system this is a problem that must be solved to minimize the failures. In these cases, the subtraction between the two values is not enough, and it becomes necessary to resort to another methodology.

Considering that in a 360° rotation, the practical difference between the two angles cannot exceed -180°/180°. When the difference between the roll of the arm and the hand exceeds this value, it means that the final value must be calculated differently. For a subtraction with a result lower than -180° it means that the wrist is in flexion and the real difference is given by:

$$realDiff = 360 + diff \qquad (3.11)$$

Likewise, if the calculated difference is greater than 180°, the wrist is in extension and the real angle is given by:

$$realDiff = 360 - diff \qquad (3.12)$$

This process of conversion is performed at each iteration. For either case, the absolute values are placed on the interface, along with the percentage reached compared to the target defined in preferences. As soon as the user clicks on the "Flexion/Extension" button again, the values are replaced by the maximum values measured. Once the button is clicked again, the variables are set to 0 and a new measurement is performed. This process of storing the maximum measurements occurs for all possible measuring angles in the system.

3.3.3.2- Pronation/Supination Evaluation

The second button at the interface allows the evaluation of the pronation and the supination. Once this button is clicked the evaluation of these two movements in the wrist begins. In this case, only the pitch angle of the arm is used, since it contains all the necessary information. These two movements are evaluated in relation to the neutral position of the arm, as shown in figure 3.36. In order to evaluate the amplitude of the movement, it is necessary to rotate inwards or outwards, placing the palm of the hand down or up, respectively. It is called pronation to the movement of rotating inwards and supination to the movement of rotating outwards, in which the direction of rotation of each one is dependent on the limb.

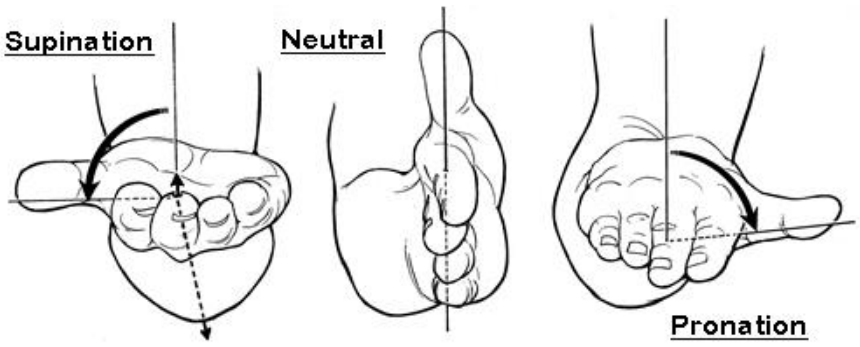

Figure 3.36- Ideal pronation/supination position [158].

In order to measure these two movements, there are 4 different positions that must be taken into account individually, originated by the set of possibilities to evaluate the limbs (left and right) with different positions of the sensors (top and bottom). As for flexion/extension, the calculated values allow measurement at 360° (180° of pronation and 180° of supination) even though clinical examinations are performed in the ideal position. These range of values are physiologically impossible to reach, except with the help of the forearm.

Considering the evaluation of the left limb with sensors at the top, the conversion of the pitch from arm to amplitude is initially performed by:

$$temp = armPitch + 90 \qquad (3.13)$$

With this sum, the 0 value is no longer the original when the IMU is horizontal and changes to the neutral position shown in figure 3.36. Since the pitch has a range between -90° and 90°, the perception of which motion is being performed needs to come from a second auxiliary. By the conformation of the sensors and the position in which the movements are evaluated, this perception is acquired from the signal of the acceleration value on the z-axis. In the neutral position the acceleration value on the z-axis is practically zero, but as rotation occurs, the axis begins to have the positive or negative gravity component, depending on the direction of rotation. If the value is positive, it means that the calculated value belongs to pronation. On the contrary, when the acceleration value is negative, the computed value belongs to supination.

Still in the evaluation in the left limb, the sensors can be placed in the palm of the hand. Based on the same considerations as above, if the pitch value is positive, the transformation to range of motion is performed from:

$$temp = -(armPitch - 90) \quad (3.14)$$

If the pitch is negative, the range of motion is given by:

$$temp = -armPitch + 90 \quad (3.15)$$

Thus, if the acceleration value on the z-axis is negative, the calculated value belongs to the pronation and if it is positive belongs to the supination. Note that once the sensors are placed upside down, the perception through the effect of gravity on the accelerometer is performed in reverse order from the previous example.

The third case occurs for the right limb with the sensors at the top. As before, if the pitch is positive, the transformation is given by:

$$temp = -(armPitch - 90) \quad (3.16)$$

If the pitch is negative, the corresponding equation is:

$$temp = -armPitch + 90 \quad (3.17)$$

Once again, if the acceleration value on the z-axis is positive, the value corresponds to the pronation, otherwise it corresponds to the supination.

The fourth and last configuration refers to using the right limb with the sensors in the palm of the hand. In this configuration, the pitch transformation is done by the equation:

$$temp = armPitch + 90 \quad (3.18)$$

Thus, if the acceleration value is negative, the calculated value corresponds to the pronation, otherwise it corresponds to the supination.

Since the computation of the range of motion at this angle intrinsically requires the acceleration of gravity, it was chosen to give a warning signal whenever the arm roll angle exceeds the ranges -60° to 60° or -120° to 120°, indicating that the values may not be consistent. Although it is possible to get the effect of gravity on the other axes of the accelerometer, the pronation/supination of the wrist for the intervals referred has the major component in yaw and would make the algorithm much more complex.

As in the previous button, once it is clicked again the values shown are no longer in real-time and become the maximum acquired amplitude. At any time, when clicked again a new evaluation is performed.

3.5.3.2- Radial/Ulnar Deviation Evaluation

The third button allows the evaluation of the radial and ulnar deviation from the yaw angle of the arm and the hand. This evaluation is performed by the outward range of motion when the ulnar deviation is evaluated, and inward when the radial deviation is evaluated, as shown in figure 3.37. Accordingly, the aspect to be taken into account is the opposite difference between the movements in each limb. The position of the sensors (top or bottom) is indifferent in the conversion of yaw to range of motion.

In this case, the yaw value is based on the magnetic north, and the discontinuity at -180°/180° can be easily achieved as long as the user is oriented to that position. From the graphs of figure 3.34, it is noted that the graph of yaw is similar to the roll. Thus, the conversion to range of motion turns out to be quite similar to roll, using the two IMUs to calculate the deviation through the yaw difference:

$$diff = armYaw - handYaw \quad (3.19)$$

To evaluate the radial or ulnar deviation, it is sufficient to reverse the signal of the difference value for the right hand, making the processing similar to the left hand.

In the ideal case and used in the clinical evaluation (with the palm of the hand facing down as shown in figure 3.37), the value of each angle yaw can present a value other than 0°, since each angle is measured in relation to the magnetic field of the earth. Thus, if the difference between the yaw angle of the arm and the hand is in a range of values between 0° and -180°, the movement is classified as radial deviation and the absolute value calculated corresponds directly to the amplitude measured in time real. On the other hand, if the result is in the range between 0° and 180°, the movement corresponds to the ulnar deviation and the simple subtraction results in the measured value.

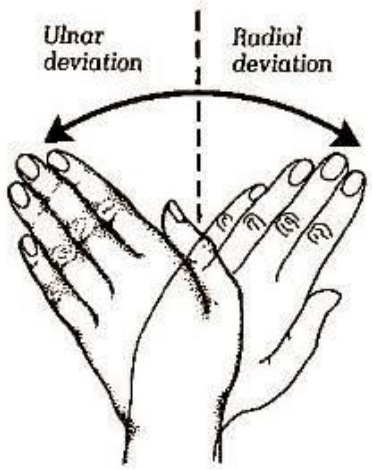

Figure 3.37- Ideal radial/ulnar deviation position used in clinical evaluation [157].

As in the evaluation of flexion/extension, it is necessary to take into account the discontinuity at -180°/180° that is easily attainable in yaw. Considering the 360° rotation and knowing that the difference between the two angles cannot exceed -180° or 180°, if the result of the subtraction is less than -180° it means that the movement to be measured corresponds to an ulnar deviation, and the amplitude is given by:

$$realDiff = 360 + diff \quad (3.20)$$

Conversely, if the result of the difference between the two yaw angles is greater than 180°, it means that the movement performed is the radial deviation and the amplitude of the motion is given by:

$$realDiff = 360 - diff \quad (3.21)$$

This is a process that occurs for each iteration just like the previous ones. For either case, the absolute values are placed at the interface with the percentage reached by comparison with the defined maximums. As soon as the button is clicked again, the maximum values reached are shown, and a new evaluation is carried out again when clicked.

3.5.3.3- Wrist Rigidity Improvement Evaluation

The fourth and last button of the evaluation activity allows the evaluation of the rigidity improvement in the wrist. Although not one of the main requirements of this dissertation, the set of the wearable device and the Android application made it easy to integrate the excellent pioneering work of the Brain group in this area with the iHandU project. The algorithm presented here for the rigidity was previously developed and only embedded in this project.

In the assessment of rigidity, the physician imposes a passive flexion on the wrist similar to figure 3.38, and through his perception of the resistance to flexion assigns a score that is subsequently translated into the severity of the muscle rigidity. This type of evaluation is widely used during Deep Brain Stimulation (DBS) surgery to evaluate the improvement in rigidity for different stimulation settings [159].

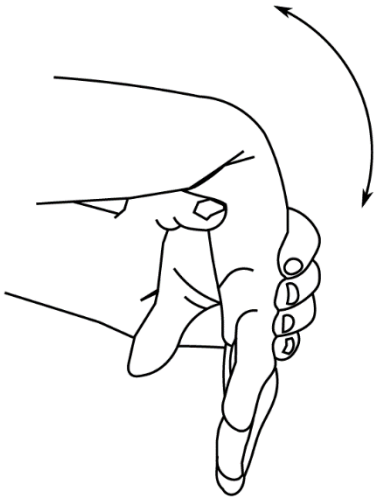

Figure 3.38- Physician method to assess wrist rigidity [159].

Having that said, the BRAIN group has developed an automatic classification system of rigidity improvement, during DBS surgeries in the Functional Surgery and Movement Disorders Unit of Hospital São João. The system developed so far uses an IMU in the palm of the hand (MoMo), and only the gyroscope data of the axis of rotation on which the wrist flexion takes effect is processed. In this case, only the values of the angular velocity during flexion has clinical interest, and consequently, the values corresponding to extensions are set to 0.

Considering that the rigidity affects the amplitude, range and smoothness of the angular velocity signal of the wrist flexion, after collecting a signal with 200 samples two features are calculated: average angular velocity, μ_ω, and average peak angular velocity, μ_p. The peaks considered here are the highest values separated by a valley, over a margin of $0.2^\circ/s$. Since these features are very susceptible to signal shape, both features were combined in a descriptor φ, to have a higher discriminative power through the equation:

$$\Phi = \sqrt{\mu_\omega * \mu_p} \quad (3.22)$$

The descriptor φ is then placed in a polynomial model developed to compute the improvement of rigidity as a percentage, built from previous acquisitions classified with medical labels and represented by equation:

$$improvement = -0.4525\Phi^2 + 16.0483\Phi - 56.8166 \quad (3.23)$$

The computed values should be in the range of 0% to 80%, where improvement values greater than 80% or less than 0% are replaced by the nearest values in the corresponding range. Still, values below 35% do not satisfy the minimum improvement expected and are very difficult to classify by the physician, being classified as 0%. The algorithm used here was completed with an accuracy above 75% [159].

In this application, as soon as the user clicks to start this evaluation, the angular velocity acquired on the x-axis of the gyroscope of the arm is subtracted to the corresponding value in the hand. As soon as there are 200 samples, the processing takes place, the result is displayed, and the process repeats. As with all previous evaluations, as soon as the user completes this evaluation, the maximum value is displayed, and the value is saved. Comparing with the existing project, the possibility of using a second IMU in the arm to remove the angular velocity components that do not belong to the flexion/extension of the wrist is an added value that can lead to a better accuracy.

During the implementation process there were still some concerns related to allowing more than one movement to be assessed at the same time and beyond ideal positions already mentioned. The major problem found that was not solved with set equations demonstrated above is the gimbal lock. As already mentioned in previous chapters, for pitch values of -90° and 90°, the remaining angles (roll and yaw) become unstable and impossible to extract coherent values. This is a problem that does not occur for the ideal positions but becomes a failure of the system from the moment the user/physician intends to study the flexion/extension and the radial/ulnar deviation in the neutral position of the pronation/supination. To solve this problem, a process was developed to act before calculating any range of motion.

Considering that in practice gimbal lock occurs for pitch values greater than 80° or less than -80°, as pitch enters these ranges of values, the subtraction in flexion/extension or radial/ulnar deviation ceases to be calculated in angles and is now calculated in quaternions. The difference between the two quaternions is given by:

$$diffQuaternion = handQuaternion * inverse(armQuaternion) \quad (3.24)$$

Since the estimated quaternions are unit quaternions, their inverse is equal to their conjugate, simplifying the calculation of the inverse by negating the 3 complex numbers. Calculating the quaternion that represents the difference between the two rotations at the gimbal lock, in the conversion to Tait-Bryan angles the gimbal lock is eliminated since the roll, pitch, and yaw angles represent the result of the subtraction. In this way, it is ensured that gimbal lock never occurs, since the difference in pitch value is approximately 0° because

the pronation/supination movement happens in the hand in the same way as in the arm. Thus, when the system is in gimbal lock, the range of motion in flexion/extension is no longer calculated by the methods explained above, and it is used the yaw from the previous quaternion. Likewise, the radial/ulnar deviation is computed using the roll angle from the same quaternion as before.

As already mentioned, the 3D animation represents the real-time motion performed by the patient. For each iteration, even if the evaluation was not required, the amplitudes of movement for flexion/extension and radial/ulnar deviation are calculated in a similar way as above and placed in the axis systems of the animation, representing only the range of motion (figure 3.33). In the pronation/supination, the calculated values are based on the same technique used above but, in this case, it is not necessary to add the 90° offset. These values are calculated at each iteration but only at the end of 3, the average values are sent to the animation, in order to reduce the noise tremor. In the graphic each pair of movements and the value of the angular velocity are represented by different colours, only illustrated when required by the buttons, as shown in figure 3.33.

Once the doctor or user wishes to finish the evaluation, simply click on the button labelled as "Finish Evaluation". This button starts a dialog with all the maximum values reached by the user, the methodology used (with or without help) and again the patient ID, as shown in figure 3.39. In this interface all fields can be changed if necessary. After the confirmation or rectification of the variables, the user can select between: dismiss, save and finish, and save and continue.

By clicking on the "Dismiss" option, the evaluation is discarded, and the text file is deleted from the directory. On the other hand, by clicking on "Save & Continue", the data visible in figure 3.39 along with the evaluated limb, the date and the time are organized into a data structure. Once organized, the object is stored in an array of evaluations performed on the smartphone through the tinyDB library. This array has all the evaluations that have not been deleted or sent to the web service. Then, the dialog closes and the user is allowed to start a new evaluation. Finally, by clicking "Save & Finish" the same process as before occurs, but now the evaluation interface is finished, and the user returns to the main menu.

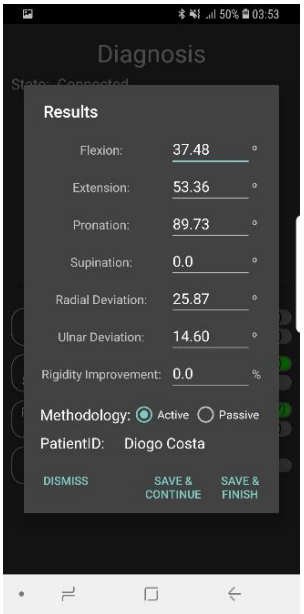

Figure 3.39- Final dialog interface.

The evaluation presented here allows the calculation of the range of motion in any of the positions previously mentioned, with the possibility of simultaneous evaluations. However, for the most accurate outcome, the assessment should be performed at similar positions used by the physicians who perform these diagnoses. Another aspect to take into account is the evaluation of more than one movement at a time or in incorrect positions. In such cases, the measured angle may not translate into the maximum value since the same set of muscles are being used for other movements.

3.5.4- Wearable Device Calibration

As already referenced by the Firmware section, the feature now introduced allows the user to calibrate IMU magnetometers of the wearable device. Therefore, similarly to the previous section, the user can select a device to connect by reusing the same interface and activity used in the previous section and again illustrated in figure 3.40 (A). Just as before, after selecting the device, the new activity is started and connects to the same Android service as before (with the same error handling), but now with the interface represented in the figure 3.40 (B). Once the BLE connection is established, calibration may be required. The request is made as soon as the user clicks the "Calibrate" button that remains in loading until the end of the operation.

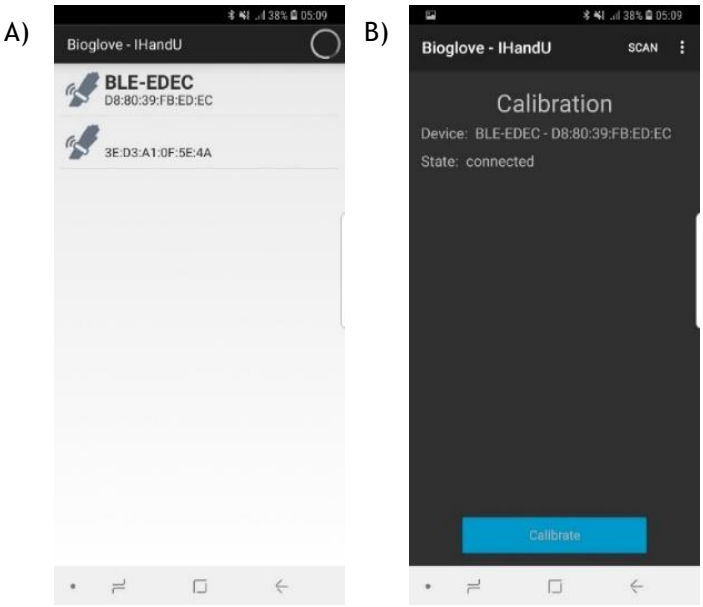

Figure 3.40 - Calibration Interfaces. The figure represents the selection interface in A, and the main calibration interface in B.

When this button is pressed, a timer is triggered to send the string "cal" through the RX characteristic defined by the Transparent UART of the BLE. This timer is repeated every second (10 times) with 0.1 seconds between characters until receiving the first "ACK1" message, ensuring that character set was received by the wearable device. At this stage, the interface will give feedback to the user that the hand's IMU is being calibrated and must repeat the movement represented by the horizontal eight patterns, as shown in figure 3.41 (A). As soon as the wearable device initiates the calibration of the arm's IMU, the message "ACK2" is received and the animation that represents the processing state is passed to the second IMU (figure 3.41 (B)). Finally, the firmware sends the message "ACK3" to the

smartphone. Once it's received, the smartphone gives the calibration as finished (figure 3.41 (C)) and returns to the main menu.

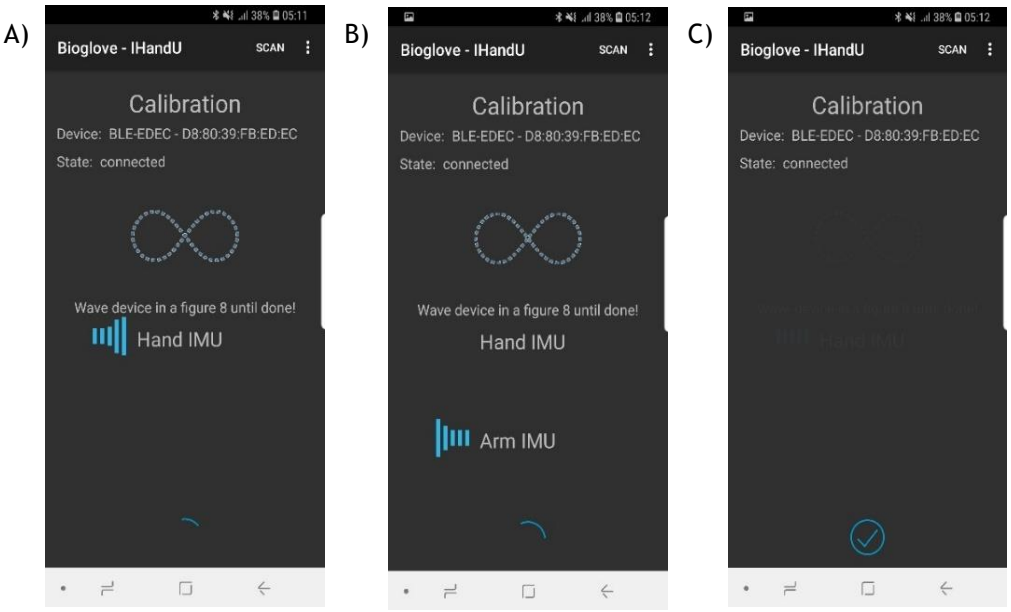

Figure 3.41- Interfaces of the calibration process.

3.5.5- Preferences

The preferences interface can be accessed from the main menu. In this activity, the user can define the maximum angles expected for each movement that can be evaluated. Subsequently, these values are used as a comparison in the evaluation. Initially and according to figure 3.42, the default maximum angles indicated by the literature already referenced in state of the art are placed in the corresponding positions. The user can set the values as needed, replacing those already in memory. It is also allowed to restore the default values to replace the changes made. As soon as the user returns to this interface, it will be shown the previously defined values.

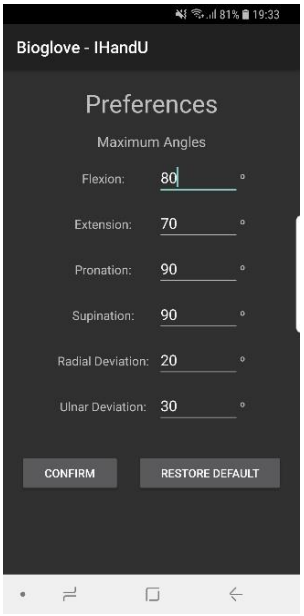

Figure 3.42- Preferences Interface.

3.5.6- Synchronize Stored Data with Online Database

This section of the application requires the prior knowledge of Hypertext Transfer Protocol (HTTP) used to communicate between the smartphone and the server. The HTTP functions as a request/response protocol in the client/server model, by which two machines communicate using a reliable, connection-oriented transport service such as the TCP/IP protocols. In general, it is a stateless and straightforward protocol used to transfer data over the web where the connection is maintained between client and server only for the immediate request. The most common methods are GET, POST, PUT and DELETE, but there are others that are not so frequently used. For the present situation, it was decided to use POST since it is more difficult to hack, the parameters are not stored in browser history or in web server logs and the variables are not displayed in the URL.

Therefore, the feature of synchronize data in the application allows the user to upload the performed evaluations to the web service. This section has two sequential screens, where the first screen works as user validation through its credentials as shown in figure 3.43 (A). In this "Sign In" screen, the user must enter their corresponding username and password. The confirmation button is only enabled when there is an internet connection, which is verified by a BroadcastReceiver. The account creation, as well as its maintenance, is only performed by the web service, as it will be seen in the corresponding section.

Once the user clicks the "Sign In" button, a set of account certifications are triggered. The password is encrypted into a 128-bit hash value from the MD5 message-digest algorithm (the methodology used to store the passwords in the database), and together with the username are placed in a list with the respective keys. This parameter list is sent via POST method in an HTTP request to a file allocated on the FEUP servers. This file whose directory is defined in the URL was written in PHP and receives the parameters sent by the Android. After verifying that both parameters have been received is performed a query on the online database (also allocated in FEUP servers) by the desired username, returning a response in JSON with a success tag and a message to the smartphone that is directly displayed to the user on Android via Toast.

The null result of the query indicates that the username does not exist, and the response returned has the "success" tag with 0 value and the "Username does not exist" message. If the query returns a compatible profile with the username, the next step is to compare the password sent by the Android with the password stored in the database. Supposing that passwords are not compatible, just as before a message is sent to the Android with the tag at 0 saying "Password is incorrect". The last check happens if the profile exists and the passwords are compatible, verifying if the account is active or inactive (defined by the administrator). If the account is inactive a tag is sent with value 0 and the "Account is disabled" message. Finally, if all certification steps are completed, a response is sent to Android with the tag at 1 and the message "Sign in". With the "success" tag at 1, the server authorizes the user to synchronize the data of the evaluations stored in the smartphone, and the application automatically changes to the data synchronization interface.

While the entire certification process occurs in background, it is illustrated a progress dialog with the "Connecting ..." message that ends as soon as the smartphone receives the response from the server (figure 3.43 (B)). This interface also allows the user to save the credentials for future usage through the TinyDB library.

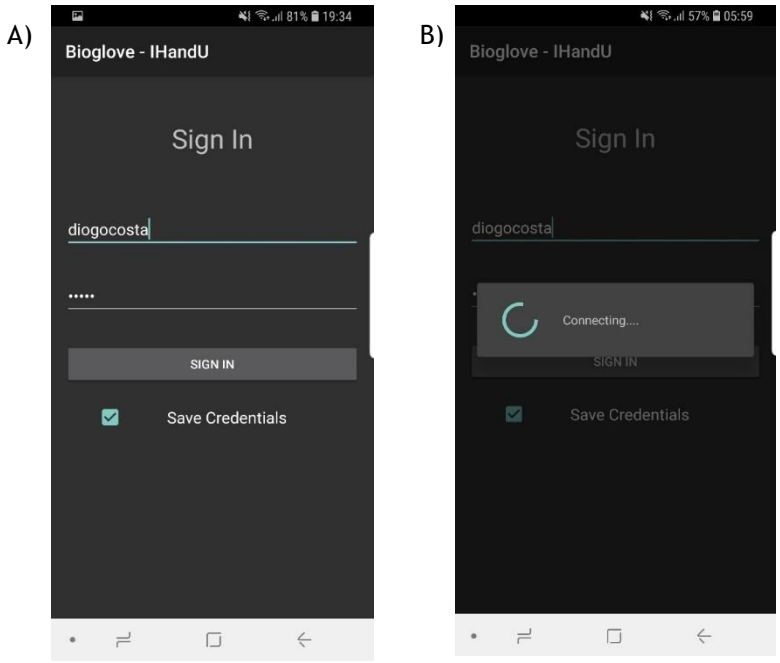

Figure 3.43- Sign In interface.

After account certification, the user has access to the synchronization interface with the database, showing the entire list of evaluations performed by the smartphone where the application is installed. The list that this activity accesses is the same used by the evaluation activity to add a new evaluation and it can be accessed by TinyDB, in the form of an array where each evaluation follows the data structure already mentioned. In this screen only the patient, date and time of each evaluation are represented, allowing the user to dismiss or to synchronize each assessment individually by swiping it to the left or right, respectively (figure 3.44).

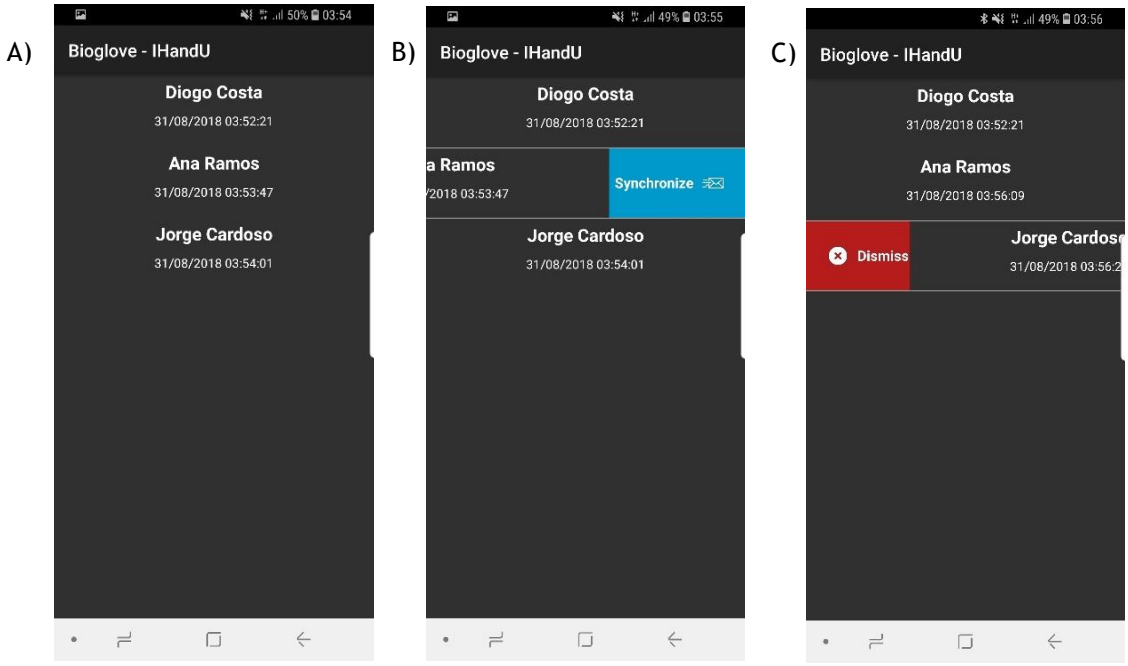

Figure 3.44- Evaluation management interface.

Supposing that the user decides to dismiss, the selected evaluation is eliminated from the list, being no longer in the memory of the smartphone by updating the previous list by the new one. In this regard, the corresponding file with the name in the format "patientID ddmmyyyy hhmmss" from the "Bioglove-iHandU" directory of the internal memory is deleted.

On the other hand, if the user wants to synchronize the evaluation with the database, the process requires a new HTTP request. While the data is being sent, and the smartphone waits for the response from the server, a progress dialog starts with the message "Saving ...". Similarly to the previous interface, the corresponding diagnostic data is placed in a parameter list with an associated key, where the username is also added. This list is sent in an HTTP request with the POST method to a PHP file with a specified URL.

The file on the server starts by checking that all expected fields are populated to insert the data in the evaluations table of the database. Assuming that all variables are filled, they are placed in the database as a new evaluation associated to the user. After the insert execution is sent back to Android a response in JSON with a "success" tag and a message. If the content of the "success" tag is 1 indicates that the insert has been successfully performed and the evaluation is deleted from the list, otherwise it is retained for further attempts.

In this context, it is also sent the corresponding text file with the data from the sensors and the Tait-Bryan angles of each iteration stored in the "Bioglove-iHandU" directory of the smartphone. If the text file exists, it is sent in a POST request with the enctype defined as multipart/form-data in order to simulate the upload of the file via form to the URL of the third PHP file developed, saving it in the "files" directory of the server. If the server response code is 200, the file has been correctly uploaded and it is removed from the smartphone's memory.

In conclusion, this feature allows the user to download or discard any evaluation independently with automatic deletion of information whenever required or as soon as the data and files are placed on the server. At any time, if the internet connection is no longer available, the alert is given by the BroadcastReceiver and the interface automatically switches to “Sign In” again. Throughout the development, small manual tests were carried out in order to guarantee the total operation of the application. However, a greater number of reliability tests (manual and automatic) should be performed, and in a second step the application should be introduced in real environment where levels of interoperability and user experience should be assessed.

3.6 - Web Platform

The web platform developed for this dissertation fills the third and last tier of Wearable Health Systems architecture, closing the cycle of the developed system. This platform essentially has two forms of contact: through Android to certify the user and upload the data of the evaluations, and through a set of web pages that constitute a website to view the performed evaluations and for maintenance of the database. In this context, it was also essential to have user accounts and an administrator account for the BRAIN group to perform database maintenance and access all evaluations in order to have as much data as possible for future improvements in the system. Therefore, it was developed to the use cases of figure 3.45. The platform was designed in PHP as the main back-end language with small parts in JavaScript to make pages more dynamic, and with HTML and CSS for the frontend. The database for saving all information was developed in SQLite.

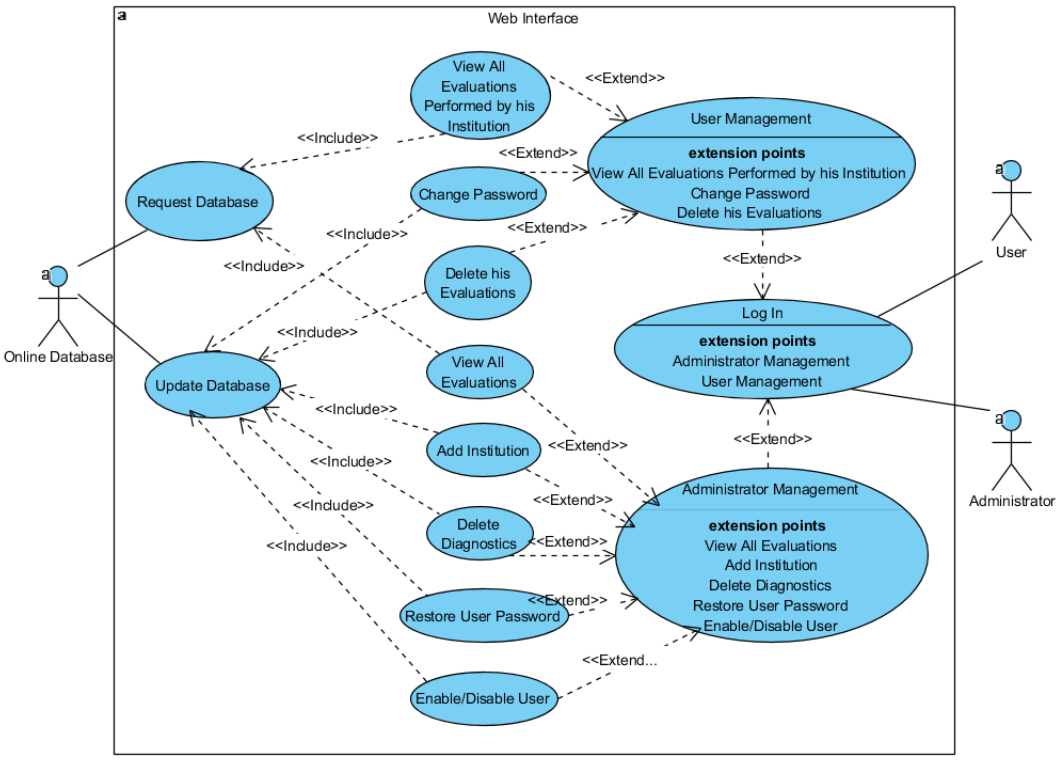

Figure 3.45- UML Use Cases of the developed web platform.

3.6.1 - Database Structure

Before describing the interface and main features, it becomes imperative to describe the structure of the database developed. The entity-relationship model (ER) of the database developed in SQLite from the DB Browser for SQLite is represented in the schematic of figure 3.46. In addition to the obvious variables that contain essential information for this dissertation, there are others used for data management that will be referenced throughout this section.

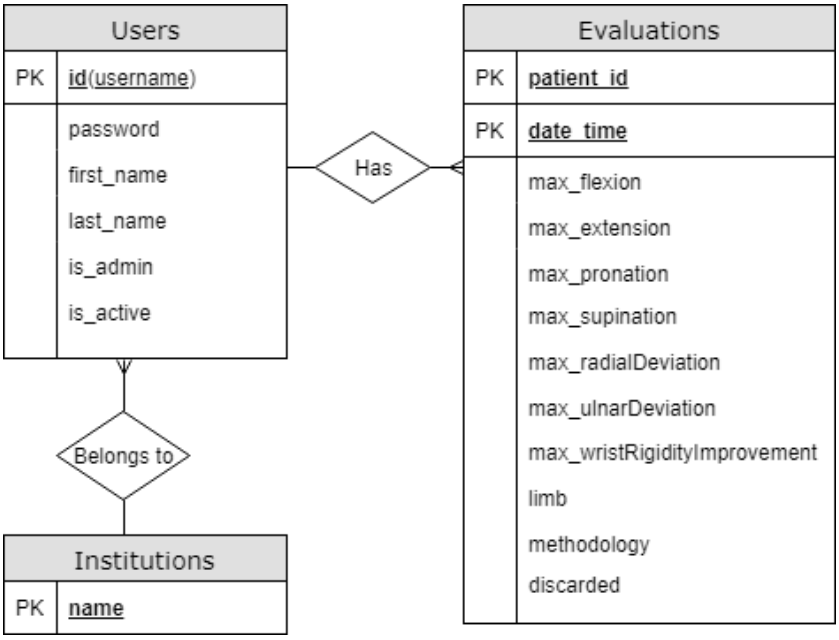

Figure 3.46- Entity-relationship model of the database.

From this model it was possible to transpose to the relational model, also with 3 tables, which represents the database created in SQLite with the following structure:

Users (id (username), password, first_name, last_name, is_admin, is_active, institution)

Institutions (name)

Evaluations (patient_id, date_time, max_flexion, max_extension, max_pronation, max_supination, max_radialDeviation, max_ulnarDeviation, max_wristRigidityImprovement, limb, methodology, discarded, user_id)

, where the variables with solid underlines are the primary keys of each table, and the dashed underlines are the foreign keys of the tables to which they bind.

Here, it was decided to create a table only with the name of the institutions so that the administrator can add new ones, even if there are no users connected. In this way, the users are allowed to merge with an institution in an independent and standardized way. After the database, the purposefully developed website that works as an interface to the database will be explained.

3.6.2- Website Interface Design

The website developed to complete the system is very simple and intuitive, and it has all the functionalities illustrated by the use cases diagram shown above. This section is divided into 3 main interfaces: sign in, administrator and user interface.

3.6.2.1- Sign In Interface

The sign-in page is the first interface of the website. This interface represented by figure 3.47, allows both the administrator and a user to access the account through their username and password. Once the credentials are inserted and the "Sign In" button is clicked, the two variables are sent by the POST method in an HTTP request to a PHP file. This file allows the verification if the user exists in the database and if the password inserted, which was encoded with the MD5 function, is compatible with the one in the database.

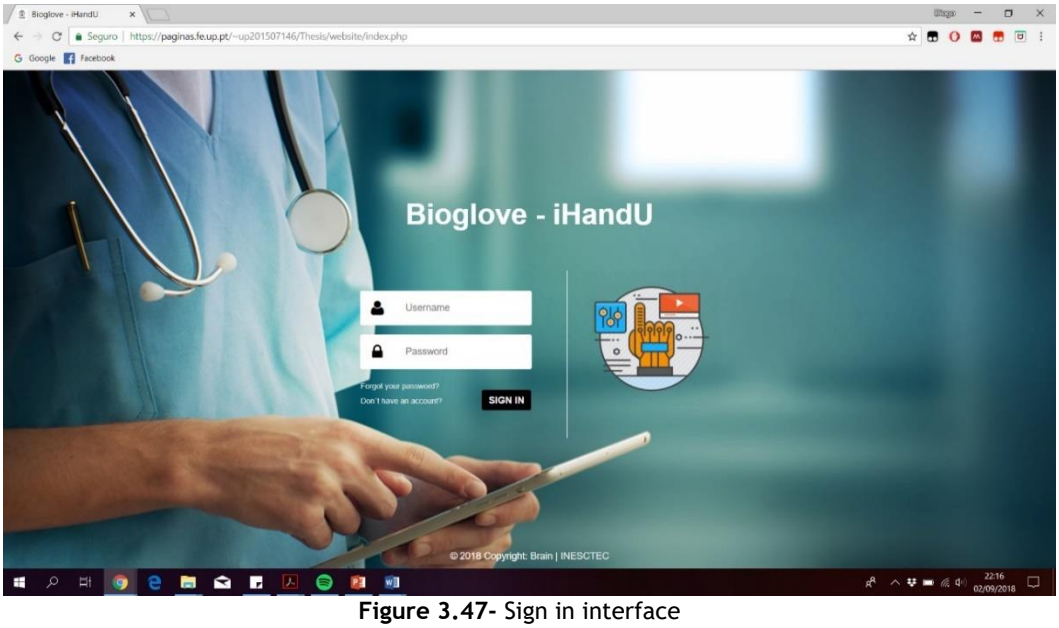

Figure 3.47- Sign in interface

If one of these processes fails, the website returns to the sign-in page in a GET request with the variable “error” containing the value 1 (in the header of the HTTP request), which leads the homepage to launch the error message "Invalid Username or Password" as shown in the figure 3.48 (A). On the other hand, if the user exists in the database and the credentials are correctly inserted, a third certification verifies if the user account is active. Once again, if the account is inactive the site returns to the homepage through a GET method but with the “error” as 2. As soon as the homepage receives this value, it produces the message with the caption "Inactive User" as shown in figure 3.48 (B).

A 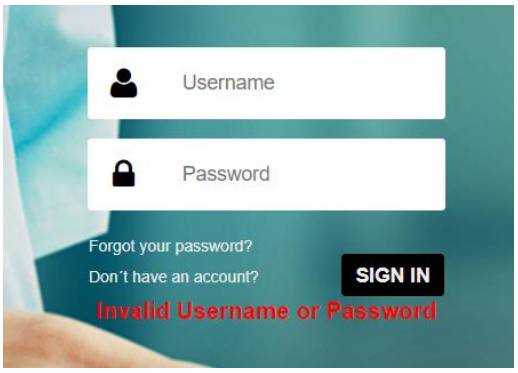

B 

Figure 3.48- Account Control Messages.

Lastly, if the PHP file verifies that the credentials are correct, and the account is active, the user is automatically directed to the corresponding page type (administrator or user) according to the value registered in the “is_admin” variable of the database. Once the account is certified, the username and the password are placed in a PHP session, making the user/administrator recognized on the webpages without having to sign in constantly. If the session is already started from previous times, when the user accesses the homepage, it automatically redirects to the respective account webpage.

From the main page, it is still possible to receive help for when the user believes to have lost his password or create a new account. If the user selects the "Forgot your password?" option, a simple message is displayed with the following: "For more information, contact the administrator" similar to figure 3.49. This message is triggered by the recursive call to the same webpage with the variable “forgot” of value 1 in the header.

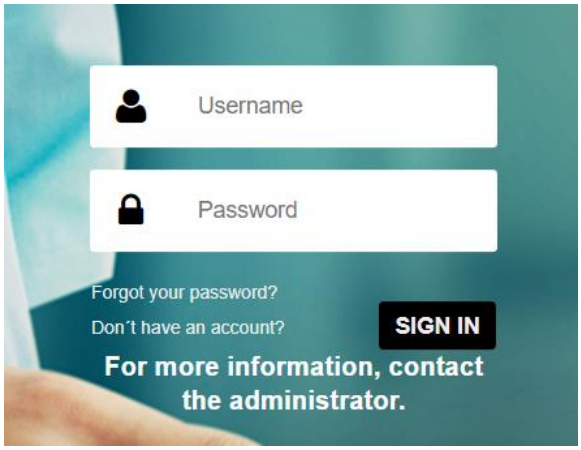

Figure 3.49- Message to recover the password.

On the other hand, if the user clicks "Do not have an account?" it triggers a new recursive call with the “createAccount” variable of value 1, also in the header, that changes the interface from the first webpage for one similar to figure 3.50. In this form all the fields have to be filled, where there is a set of institutions available, controlled by the administrator, to which the user can join. After all the fields are filled in, the "Create" button sends all the variables to an intermediate page written in PHP where certification occurs.

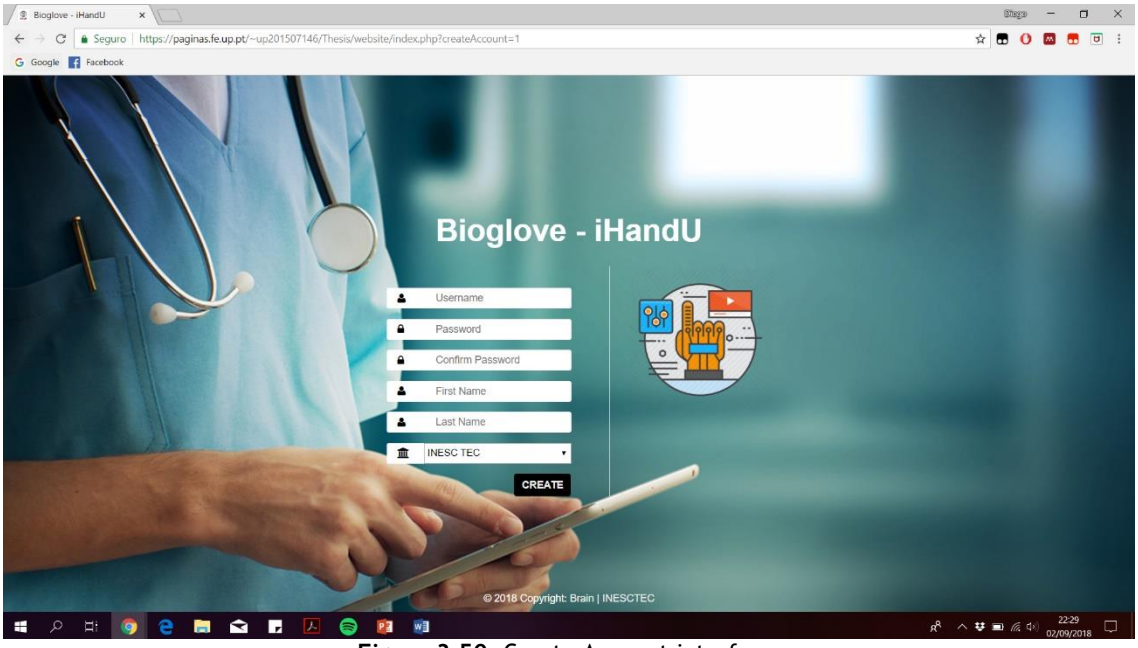

Figure 3.50- Create Account interface.

This certification verifies if the chosen username already exists in the database and if the password and its confirmation coincide. In the first case, if the username already exists in the database, the user automatically returns to the same page with the message "Username already exists", triggered by the variable "username" with value 1 in the header, as shown in figure 3.51 (A). Similarly to the previous situation, if the username does exist in the database but the passwords do not match, the variable "password" with value 1 is passed by the header, and triggers the message "Incorrect passwords", as shown in figure 3.51 (B). Finally, if the username is available and the passwords match, the account is created with the data inserted by the user. However, this insertion in the database automatically places the “is_admin” and “is_activ” variables to 0, and the user cannot access the account until be accepted by the administrator.

A 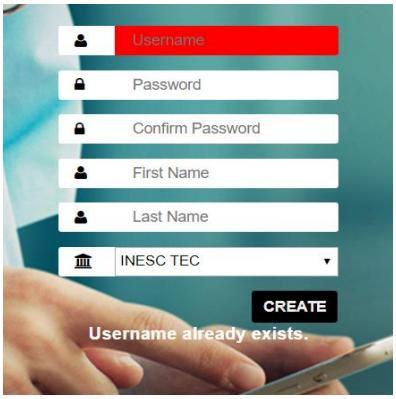

B 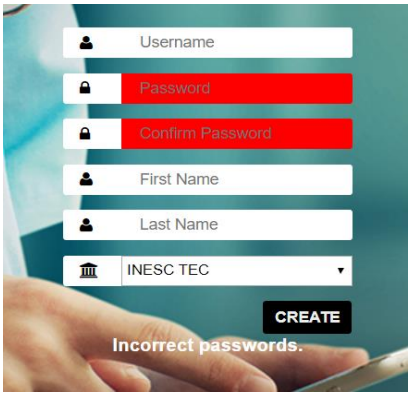

Figure 3.51- Create Account Messages.

3.6.2.2- User Interface

After the sign in as a common user, it is shown the user interface. This interface has as main objective to allow the user to visualize any evaluation made by the institution to which it is inserted. In addition, the user can discard his own evaluations and change his password.

Having that said, in the initial phase there is a verification process to check if there is any username in the PHP session, in case of negative it returns to the homepage. This makes it so that direct access to this webpage without an account started is blocked. If there is an active session started, all the diagnoses performed by the institution to which the username belongs are sorted by date and displayed in a table as in figure 3.52. This table allows the user to dynamically search for a specific patient ID, date, or any other variable through the "Filter" button without refreshing the webpage. Each of the evaluations have two buttons: one to discard the evaluation that is only available if it was done by username with the session started, and the other to download the text file if it exists in the folder "files" of the server (only visible when it is available).

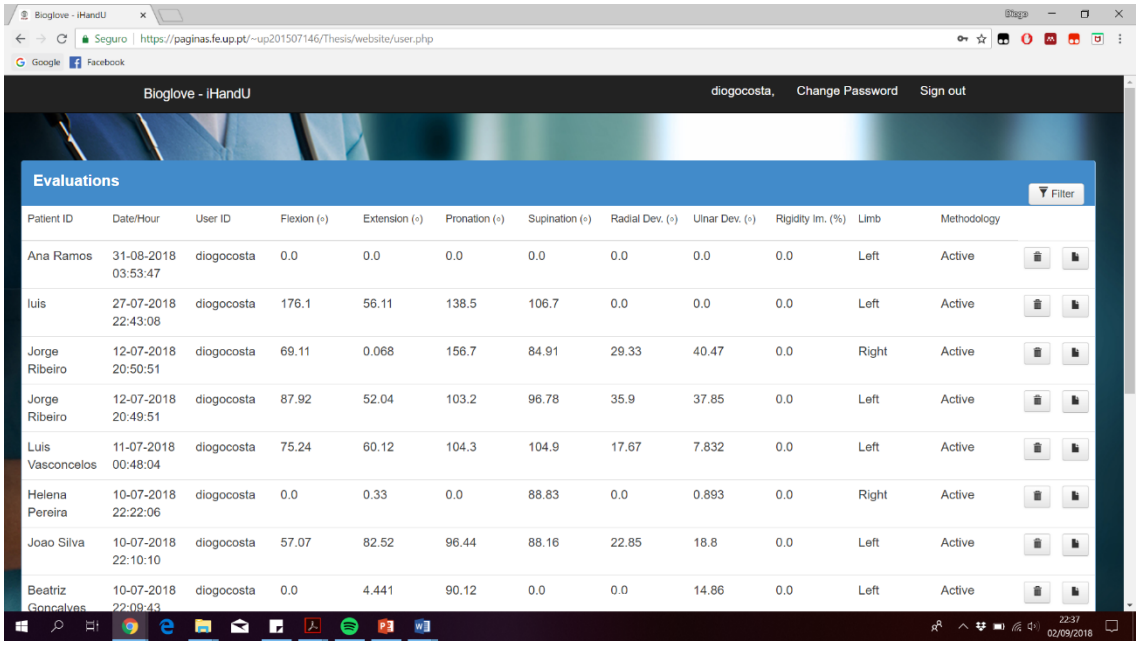

Figure 3.52- User interface.

If the user decides to discard the evaluation, it can be done by clicking the button with the trash bin icon. When pressed, this button calls a PHP file to which the primary keys (patient ID and date/time) of the corresponding evaluation are sent. This file updates the discarded variable to 1, removing it from the common user interface. On the other hand, if the button with file icon is available for the intended evaluation, it is possible to download the text file with the sensor data and Tait-Bryan angles. From the medical point of view, this file may not be very useful, but later it can be replaced by an automatic report according to future requirements.

In the upper right corner of the user webpage (visible in the previous figure), it is available the option to change the password of the account. Once selected, the webpage is recursively called with the “changePassword” parameter with value 1 in the GET method, illustrating the interface represented in figure 3.53.

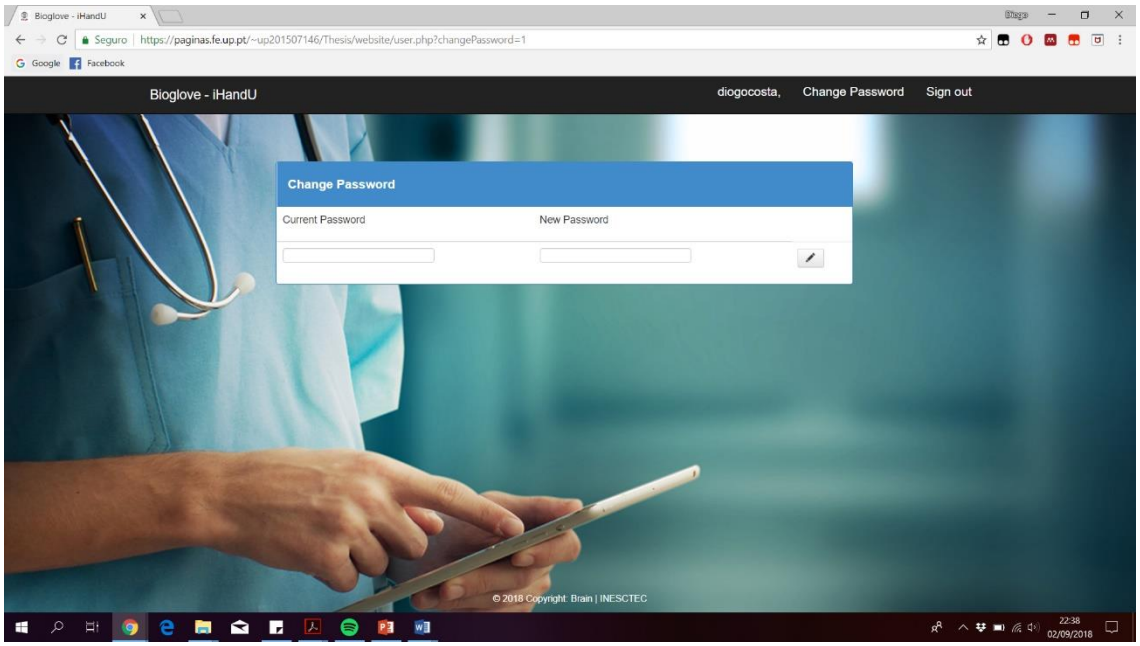

Figure 3.53- Change Password interface.

When the button is pressed, the current password and the new one are sent in the POST method to a PHP file where both are encoded using the MD5 function, and the current password is compared to the existing one in the database. If both match, the new password is inserted into the database and the user automatically returns to the homepage. Otherwise, the user returns to the same webpage with the variable “done” to 0 in the GET request, forcing the page to illustrate the message "Invalid Password" as shown in figure 3.54. Finally, if the user decides to sign out, it can be done by the button in the upper right corner, destroying the session in PHP, and taking the user to the first webpage.

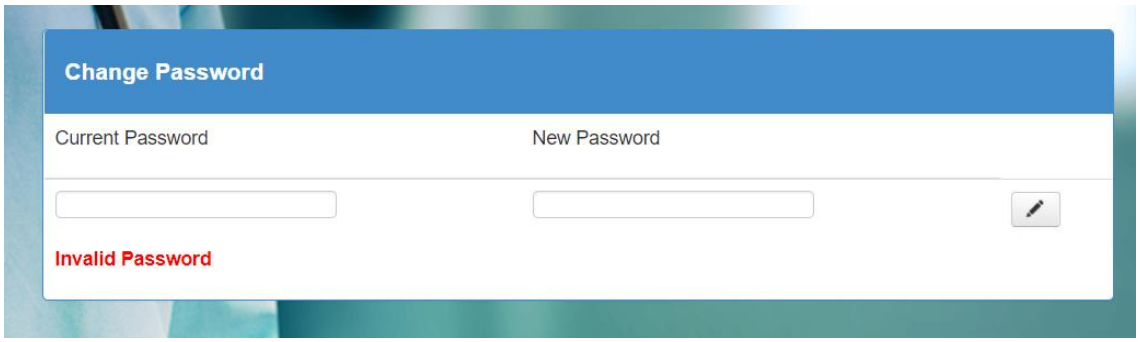

Figure 3.54- Invalid password message.

3.6.2.3 -Administrator Interface

In addition to the common user interface, the platform also has the administrator interface. Its main function is to enable the BRAIN group to manage and control the service in its entirety. More specifically, this interface allows the administrator to access and manage all the evaluations, manage the user accounts and add new institutions.

Similarly to the previous interface, in the initial phase it is checked if there is any username in the PHP session and even if the username is actually an administrator by

querying the database. As before, if the access is denied, it automatically returns to the user page or the homepage according to the session found. By accessing this page, the administrator has access to all evaluations performed by all users organized by date in a table as shown in figure 3.55. Unlike the previous interface, the evaluations discarded by the user are shown and identified by the gray color. This process is done by checking the "discarded" variable for each evaluation. As before, the administrator can dynamically search for any parameter through the "Filter" button. In addition, for each evaluation 3 functionalities are allowed: discard/revalidate the evaluation, permanently delete the evaluation, and download the corresponding text file if it exists in the directory.

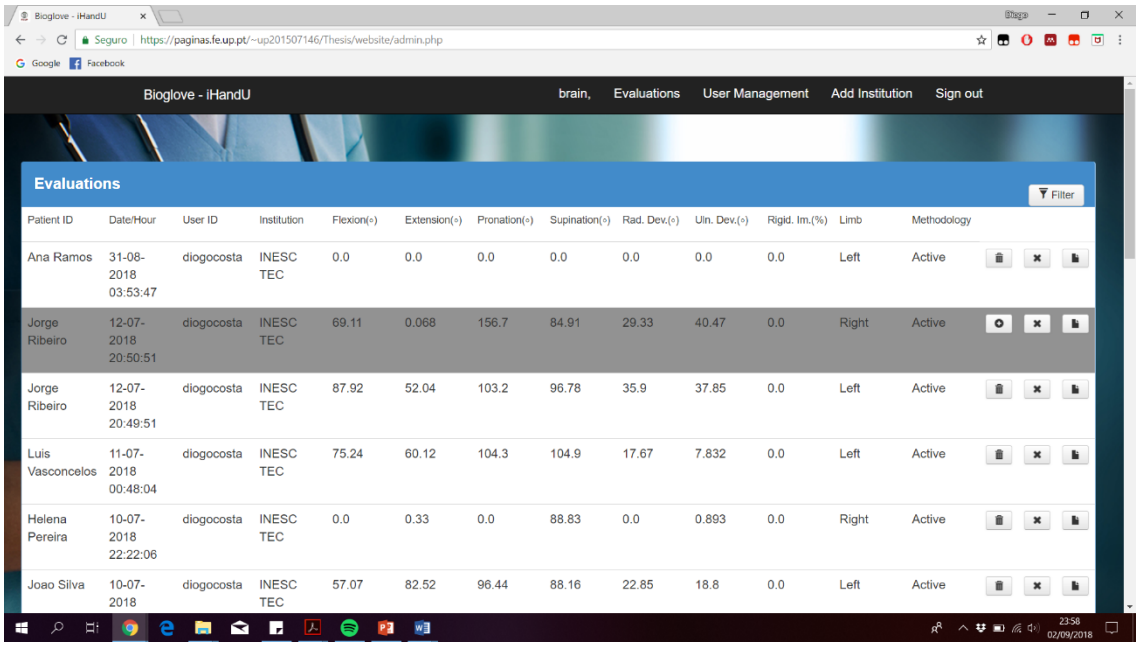

Figure 3.55- Admin interface (evaluations table).

The first button changes the icon (trash bin or plus) depending on whether the evaluation was discarded or not, respectively. If the evaluation was not discarded, as soon as the administrator clicks the button, it calls the same PHP file as before, updating the variable "discarded" to 1, and disappearing the evaluation from the common user interface. On the other hand, if the evaluation was discarded, the administrator can validate it again by clicking on the button with the plus sign icon. In this configuration, the button calls the PHP file responsible for re-validating the evaluation, by passing the primary keys (patient ID and date/time) of the corresponding evaluation. The PHP file verifies that the initiated account corresponds to an administrator by verifying the variable "is_admin" in the database, updates the variable "discarded" of the respective evaluation to 1 and returns to the administrator page.

Each evaluation also presents a second button with the icon “x” that allows the permanent deletion of the evaluation in the database. Once clicked by the administrator, this button calls another PHP file that has the same type of verifications as above, and permanently deletes the database evaluation and returns to the administrator page. The third and last button in the evaluations table allows the download of the text file with sensor data and the Tait-Bryan angles. Now, this functionality becomes essential for the BRAIN group to continue developing the system, getting as much data as possible in a simple, intuitive and automatic way. The bar at the top of the webpage also allows access to the management of

users and institutions. The administrator also has access to these features by scrolling down, since all management are contained on the same webpage.

Thus, the second main functionality allows the management of user accounts, as represented in figure 3.56. This table, also with dynamic search, allows the administrator to reset users' passwords and enable/disable the accounts. To restore the password of a specific user, the administrator clicks the button in the "Restore Password" column, making a call to a new intermediate PHP file. This PHP file, similar to the previous ones, verifies if the session belongs to an administrator and encodes the password "brain2018", replacing it with the one in the database. In this way, the user can access his account with a temporary password and replace it with a new one through his own account.

The second button in this table works similarly to the processing of discard and revalidate evaluations, but now updates the variable "is_active" to 0 or 1 of the selected user, according to the previous state. As previously for the cases where evaluations were discarded, the non-active users are colored in gray. Therefore, when a user creates his account, the account only becomes operational after the administrator accepts him in this section.

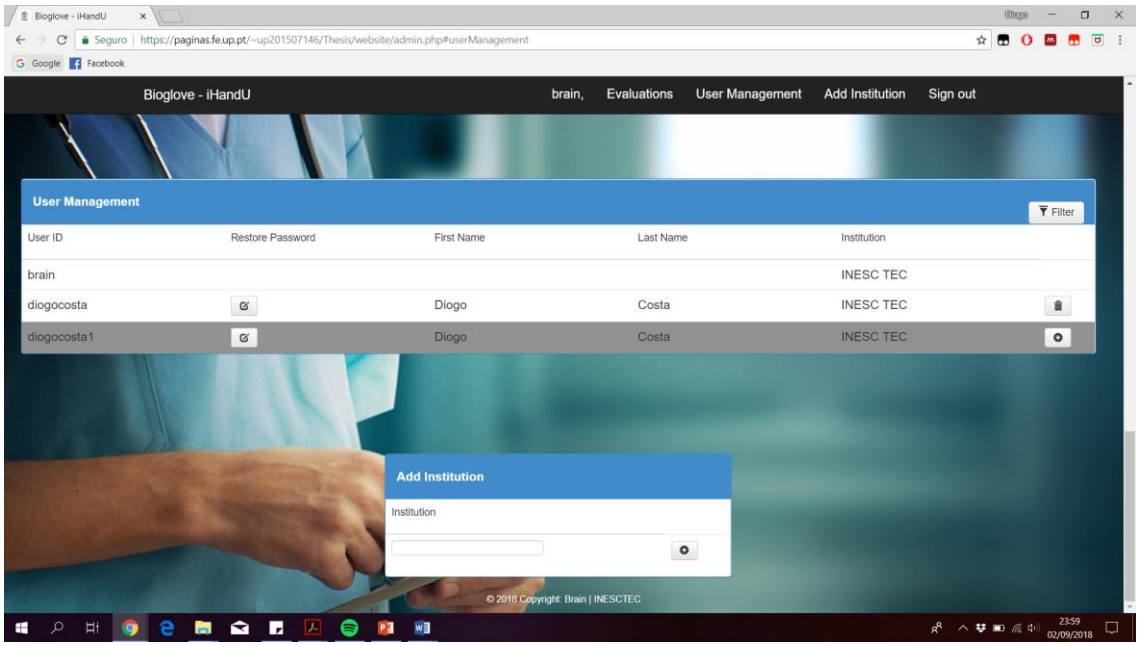

Figure 3.56- Admin interface (account and institution management).

The third and final functionality offers the administrator the insertion of new institutions that require the service. To make this possible, it was provided a section according to figure 3.55, where the administrator inserts the name of the new institution. Once the button with the plus icon is clicked, an intermediate PHP file is called to insert the new institution. This insertion is only performed if the administrator account is started and if there is no institution with the same name in the database. In the end, the administrator is returned to the previous webpage.

The platform has the minimum-security requirements, since it is used a coding function to store the passwords, all webpages and intermediate PHP files have verification of the type of account that is trying to access, and all contact with the database is done with the PHP prepare and execute methods, preventing SQL injection attacks. The homepage is available at: “https://paginas.fe.up.pt/~up201507146/Thesis/website/index.php”, where it is possible

to sign in with the username "diogocosta" and password "diogo" for a user account, and as a "brain" with the password "brainlab" for the administrator account.

In conclusion, the developed platform increase the quality of the entire system, giving total control to the Brain group. In this way, the platform favours the visualization of the results for the user, being able to draw some conclusions on the temporal evolution of a given patient, and at the same time it allows an enormous ease of obtaining the data for future developments that can grow from this point forward.

3.7- Wearable System

The set of services provided in this dissertation are summarized in this section. The wearable device prototype communicates directly via Bluetooth to the Android application to send data from both IMUs and receive the calibration request. The Android application has a main menu with several options, being the wrist range of motion and the quantification of rigidity analysis the ones that stand out the most. There's also the possibility to request the calibration and the synchronization of the data with the online database. Finally, there is a website available for evaluation visualization and database management. This set of services allows the physician to have the evaluations on a global platform, and the BRAIN group to continue the development of the project with full access to the data previously gathered.

In conclusion, it was possible to create a wearable device supplemented by a service with two platforms (Android and Web application), including all the essential functionalities, as shown in figure 3.57. Battery life tests were also performed with the prototype continuously connected to the smartphone. The 190mAh battery allowed an acquisition of 13h30.

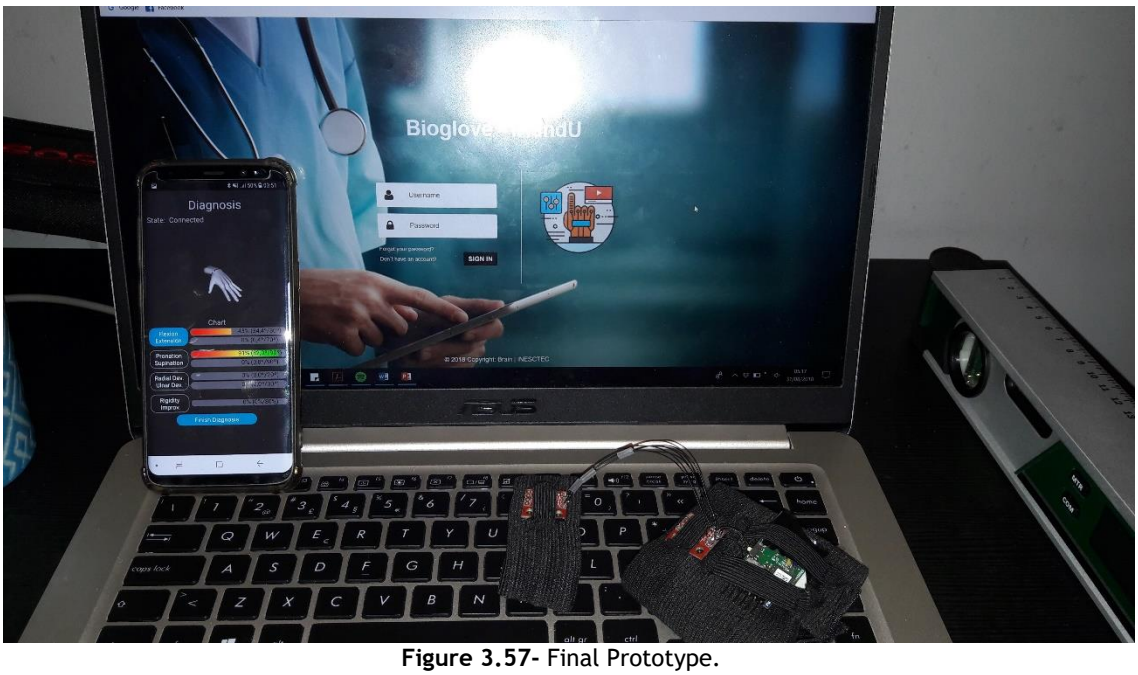

Figure 3.57- Final Prototype.

Chapter 4

Prototype Performance Evaluation

Now with the system prototype properly structured and developed, it was time to test it. Despite the excellent results in the estimation of orientation obtained in the algorithm developed in R, it is essential to compare the prototype with the gold standard currently used in clinical practice. Throughout this chapter, it will be illustrated the results obtained in the evaluation of the range of motion and in the quantification of the rigidity improvement in DBS surgeries.

4.1- Range of Motion

Starting the illustration of the results by the quantification of the maximum angles, the system proposed in this dissertation was compared with a goniometer similar to that of figure 4.1, which has a measurement uncertainty of ± 0.5°. For each movement, there were obtained 5 samples with arbitrary positions in the same individual with the prototype and with the goniometer, simultaneously. In this case, the most relevant aspect in validation is accuracy from different angles. The use of the device in different individuals has reduce or none effect on the validation of the prototype. In all measurements, the device was used in the right limb with the sensors at the top of the hand. The individual was seated with the forearm properly supported, the fingers relaxed and stabilized to prevent the involuntary pronation/supination movements.

Figure 4.1- Goniometer similar to the one used in this work [160].

The first movement to evaluate was the flexion. In this regard, the individual performed 5 flexion movements to a random position and the values were acquired by the prototype and

the goniometer, as shown in table 4.1. The goniometer was properly positioned according to the literature with the axis lateral to the wrist, in the triquetrum zone, the stationary arm aligned with the ulna and the moving arm aligned as the 5th metacarpal, similar to figure 4.2 (A) [161]. The uncertainty of the measurements are given by the confidence interval shown in the Bland-Altman plots of figure 3.26. The values presented in the table show an RMSE of 1.38°.

Table 4.1- Measurements obtained in flexion.

Prototype ±0.7°	Goniometer ±0.5°
67.1	69
59.2	61
65.5	65
44.0	45
48.8	50

Similar to the previous evaluation, with the goniometer in the same position, the movement of the extension was evaluated (figure 4.2 (B)). The values of the 5 repetitions are represented in table 4.2, presenting a final RMSE of 1.43°.

Table 4.2- Measurements obtained in extension.

Prototype ±0.7°	Goniometer ±0.5°
37.1	39
35.8	38
54.6	54
50.4	51
62.0	61

A 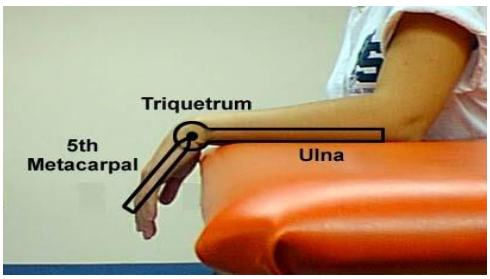

B 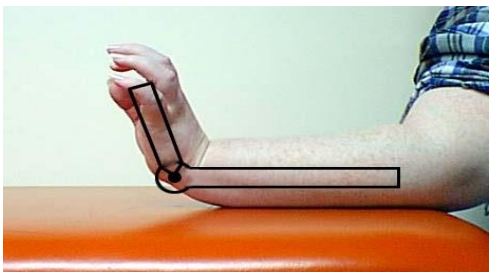

Figure 4.2- Positions for evaluation of flexion in A and extension in B [162].

The following movement that was evaluated with the device and compared to the value measured by the goniometer was the radial deviation. For this purpose, the 5 amplitudes were evaluated with the axis of the goniometer in the capitate, the stationary arm aligned with the epicondyle side of the forearm and the moving arm aligned with the metacarpal of the middle finger, as shown in figure 4.3. The evaluations are illustrated in table 4.3, concluding the evaluation with an RMSE of 1.62°.

Table 4.3- Measurements obtained in radial deviation.

Prototype ±2.6°	Goniometer ±0.5°
10.4	12
17.0	15
13.6	12
17.6	16
13.8	15

Once again, by placing the goniometer in the same position as before, the ulnar deviation was evaluated according to figure 4.3. The evaluations are shown in table 4.4, with a final RMSE of 2.57°.

Table 4.4- Measurements obtained in ulnar deviation.

Prototype ±2.6°	Goniometer ±0.5°
11.3	9
22.2	26
15.4	14
23.5	21
12.3	10

A 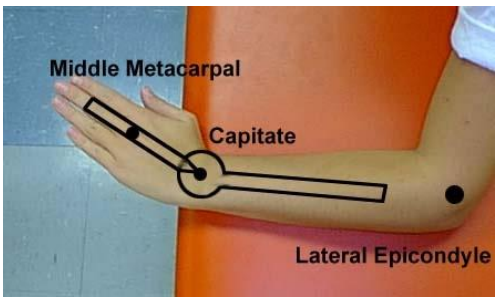

B 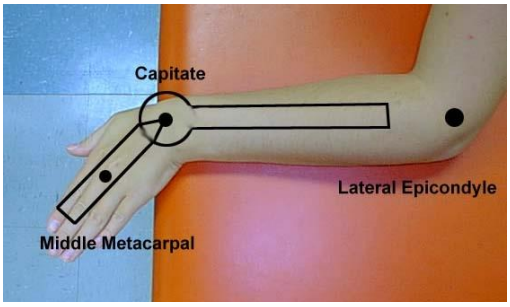

Figure 4.3- Positions for evaluation of radial deviation in A and ulnar deviation in B [162].

Although the prototype developed has the capacity to evaluate the movements of pronation/supination (with a measurement uncertainty of ± 1.03°), the goniometer does not allow to evaluate this movement. In addition, this movement occurs within the forearm, and usually it is not present in the set of diagnoses performed for the range of motion analysis.

In general, the values reveal a clear discrepancy when compared with the values reached in the determination of the best algorithm. It would be expected similar values since the processing of Tait-Bryan angles to range of motion conversion is based on sums and subtractions and does not change the accuracy of the final result. However, this difference can be explained by two main factors.

The main factor is difficulty in placing the two IMUs in the exact positions, which can cause an error in the subtraction between the estimation of the two orientations of some degrees. However, if this error is considered as systematic, it will similarly affect all evaluations. The second factor focuses on the fact that the handling of the goniometer has not been performed by a health care professional, which can involve small errors related with the position of the measurement. Furthermore, the analysis of the range of motion by the

goniometer is not as accurate as the proposed prototype, since there is a greater facility of error due to the visual measurement. Still, while with the goniometer the patient needs to stabilize at the maximum amplitude so that the physician can perform the measurement, with this prototype the patient only needs to reach the maximum amplitude instantaneously.

Finally, this study allowed to realize that the measurement of the range of motion by the prototype developed in this dissertation presents a good accuracy, even with the estimation of the orientation from simple complementary filters. In this sense, this set of evaluations also allowed to conclude that radial/ulnar deviation computed from yaw angle presents a satisfactory error considering that it is one of the angles most affected by the read values of the magnetometer. However, the results are not always consistent, and there are sometimes substantial changes in the value measured by changes in the external magnetic field, although it can be attenuated by a calibration before each evaluation.

4.2- Rigidity Quantification

In the slope of the rigidity quantification by integration of the algorithm already developed by the BRAIN group, the prototype developed was tested during DBS surgery performed at the Hospital S. João (figure 4.4). This system compared to the one currently being used by the group in these surgeries has a second IMU that allows excluding the angular velocity that does not belong to the movement of the flexion. The main goal was to collect information from the two devices (the prototype and the current device) to compare the improvement computed by each one with the medical label. Unfortunately, the hardware eventually failed to withstand the continuous stress of motion throughout the operation, where the wires that connects the microprocessor to the IMUs eventually collapsed.

From this opportunity to test the prototype in real environment can be drawn two main conclusions: the first is the confirmation that the hardware needs to be more robust, there's a need to take it to the next iteration for a more stable prototype such as the improvement of the wire connections, the development of new PCBs and the design of new textile models; the second conclusion comes from the first, since the prototype definitely needs to be smaller, more resilient and more comfortable, so the physician can continue to carry out his own evaluation without worrying about the potential stress on top of the wearable device.

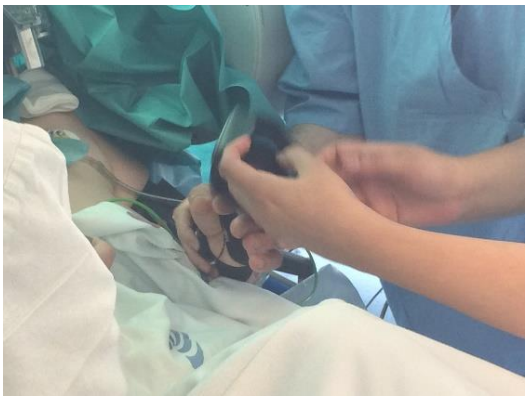

Figure 4.4- Prototype tested during surgery.

Chapter 5

Conclusion and Future Work

Wearable health devices are a relatively recent concept in the medical field with plenty of growth opportunities, improving the medical service in a wide range of applications. Under the WHS (Wearable Health Systems), the prototype system developed in this master thesis complies with all the requirements initially proposed. In addition, throughout the work, new functionalities were implemented that aimed the improvement of the entire system, achieving satisfactory results.

Thus, it was developed a prototype as a proof of concept where the hardware is easily inserted and removed from the two designed bands to simplify the placement of the wearable device on the patient's wrist. The set of hardware and firmware allows the acquisition of kinematics data that is sent to the Android application and converted into range of motion of the wrist. Additionally, given the compatibility of the data, it was integrated the algorithm of rigidity quantification that has been developed in the iHandU project. Although not initially planned, the development of a web platform has become an added value, incorporating the easiness of obtaining data for a continuous integration of the developed project. However, this prototype has some limitations that should be addressed as part of future work.

The current limitations are primarily focused on the hardware and the Android application. On the hardware, the wire connections between the sensors and Bluetooth module with the microprocessor rupture with relative easiness due to the stress caused by the movement. Therefore, as short-term future work, it would be ideal to improve the connections in the hardware through connectors or similar components that favour the stability of the prototype.

Furthermore, the firmware developed is at the limit of the memory capacity of the microprocessor, and the BLE module used has internal complications that affect the reliability of the prototype, having been necessary to replace it several times.

Despite the IMUs used in this dissertation revealed enough competence in the accuracy of the measurements, it is necessary to replace the microprocessor by one of higher capacity according to the processing to be performed. At best, the Tait-Bryan angles computation could be implemented in the firmware, drastically decreasing the amount of data to send via Bluetooth. The replacement of the BLE module for a more stable model should also be

considered. Thereby, it will be essential as future work to develop a new PCB hardware in order to give more stability, pondering the direct integration in a possible new textile model.

Additionally, the conversion of Tait-Bryan angles to the range of motion developed in the Android application does not work perfectly under all conditions, since each of the movement is always computed from the same angle. To overcome this problem, it would be necessary to develop an intelligent algorithm to determine the position of the arm and decipher which Tait-Bryan angle to use. Nevertheless, this is a limitation that does not affect the accuracy of the system for the vast majority of the positions, and especially for the positions used in clinical practice.

Also as future work, the new prototype can take on a scaled model with a more significant number of IMUs to measure the range of motion in each finger already with force sensors. These sensors can be placed in strategic positions to measure the amount of strength the physician needs to assess rigidity during DBS surgery, providing data to optimize the rigidity quantification algorithm. In another perspective, force sensors can be designed to measure the patient's strength during pinch and grasp movements. More ambitiously, if the new design continues with separate bands, the communication between them can be performed via Bluetooth, suppressing the connection by wires. Bearing in mind the other components developed, it would be interesting to allow the physician to write down observations at the end of the evaluation in the Android application. These notes could be part of the data sent to the database with access through the web platform. In this platform, it will be interesting to replace the text file provided to the user by an evaluation report or set of evaluations over time for a given patient.

Finally, the prototype system developed under this master thesis contributes to a new stage of opportunities in the projects developed in the BRAIN group, becoming even closer to develop a device to rectify the current lack of technology in this area.

References

[1] "Hand Anatomy, Pictures & Diagram | Body Maps." [Online]. Available: https://www.healthline.com/human-body-maps/hand. [Accessed: 20-Dec-2017].

[2] G. Elkoura and K. Singh, "Handrix: animating the human hand," *Proc. ACM SIGGRAPH 2003 Symp. Comput. Animat.*, pp. 110–120, 2003.

[3] H. W. Wallmann, "Overview of wrist and hand injuries, pathologies, and disorders: Part 2," *Home Heal. Care Manag. Pract.*, vol. 23, no. 2, pp. 146–148, 2011.

[4] M. T. Duruöz, L. Cerrahoglu, Y. Dincer-Turhan, and S. Kürsat, "Hand function assessment in patients receiving haemodialysis.," *Swiss Med. Wkly.*, vol. 133, no. 31–32, pp. 433–8, 2003.

[5] F. Dincer and G. Samut, "Physical Examination of the Hand," pp. 23–41, 2014.

[6] L. Lippert, *Clinical Kinesiology and Anatomy , 5th ed. Philadelphia*. 2011.

[7] P. J. Mansfield and D. A. Neumann, *Essentials of kinesiology for the physical therapist assistant*. Elsevier Health Sciences. 2014.

[8] "Ligament | anatomy | Britannica.com." [Online]. Available: https://www.britannica.com/science/ligament. [Accessed: 07-Dec-2017].

[9] J. R. Ralphs and M. Benjamin, "The joint capsule: structure, composition, ageing and disease.," *J. Anat.*, no. Pt 3, pp. 503–9, 1994.

[10] T. Mcmahon, P. C. M. Van Zijl, and A. A. Gilad, "Fluid movement and joint capsule strains due to flexion in rabbit knees," vol. 27, no. 3, pp. 320–331, 2015.

[11] J. C. Leggit and C. J. Meko, "Acute finger injuries: Part I. Tendons and ligaments," *Am. Fam. Physician*, vol. 73, no. 5, pp. 810–816, 2006.

[12] H. Bade, M. Schubert, and J. Koebke, "Functional morphology of the deep transverse metacarpal ligament," *Ann. Anat.*, vol. 176, no. 5, pp. 443–450, 1994.

[13] P. K. Levangie, C. C. Norkin, and P. K. Levangie, *Joint structure and function : a comprehensive analysis*. F.A. Davis Co, 2011.

[14] "Hand | Clinical Gate." [Online]. Available: https://clinicalgate.com/hand-3/. [Accessed: 11-Jan-2018].

[15] "Muscle | Britannica.com." [Online]. Available: https://www.britannica.com/science/muscle. [Accessed: 17-Dec-2017].

[16] "How do hands work?" [Online]. Available: https://www.ncbi.nlm.nih.gov/books/NBK279362/. [Accessed: 17-Dec-2017].

[17] "What is RA? Rheumatoid Arthritis Diagnosis." [Online]. Available: https://www.webmd.com/rheumatoid-arthritis/diagnosing-ra?print=true. [Accessed: 30-Dec-2017].

[18] "Kinematics | physics | Britannica.com." [Online]. Available: https://www.britannica.com/science/kinematics. [Accessed: 30-Dec-2017].

[19] R. F. Gans, "Engineering dynamics: From the lagrangian to simulation," *Eng. Dyn. From Lagrangian to Simul.*, pp. 1–267, 2013.

[20] D. Dragulescu, V. Perdereau, M. Drouin, L. Ungureanu, and K. Menyhardt, "3D active workspace of human hand anatomical model," *Biomed. Eng. Online*, vol. 6, pp. 1–12, 2007.

[21] A. M. R. Agur, M. J. Lee, and J. C. B. (John C. B. Grant, *Grant's atlas of anatomy*.

Lippincott Williams & Wilkins, 1999.
[22] J. M. (James M. Hunter, *Rehabilitation of the hand : surgery and therapy*. Mosby, 1990.
[23] L. Ombregt, “Applied anatomy of the wrist, thumb and hand,” *A System of Orthopaedic Medicine*, pp. e102–e111, 2013.
[24] C. C. Norkin and D. J. White, *Measurement of joint motion : a guide to goniometry*. F.A. Davis, 2003.
[25] W. Lowe, “Orthopedic Assessment In Massage Therapy,” in *Orthopedic Assessment in Massage Therapy*, Orthopedic Massage Education & Research Institute, 2006, p. 4.
[26] J. Fox and R. (Richard J. Day, *A physiotherapist’s guide to clinical measurement*. Churchill Livingstone/Elsevier, 2009.
[27] Departement of Social and Health Service, “Range of Joint Motion Evaluation Chart,” *Washingt. State*, pp. 2002–2003, 2003.
[28] “MRC Muscle scale - Research - Medical Research Council.” [Online]. Available: https://www.mrc.ac.uk/research/facilities-and-resources-for-researchers/mrc-scales/mrc-muscle-scale/. [Accessed: 31-Dec-2017].
[29] S. Balasubramanian, A. Melendez-Calderon, A. Roby-Brami, and E. Burdet, “On the analysis of movement smoothness,” *J. Neuroeng. Rehabil.*, vol. 12, no. 1, pp. 1–11, 2015.
[30] T. Beukelman, L. Callahan, and L. Murphy, “Arthritis By The Numbers,” p. 99, 2017.
[31] J. L. Poole, D. D. Santhanam, and A. L. Latham, “Hand impairment and activity limitations in four chronic diseases,” *J. Hand Ther.*, vol. 26, no. 3, pp. 232–237, 2013.
[32] E. Halilaj *et al.*, “In vivo kinematics of the thumb carpometacarpal joint during three isometric functional tasks,” *Clin. Orthop. Relat. Res.*, vol. 472, no. 4, pp. 1114–1122, 2014.
[33] C. A. Taylor, J. M. Bell, M. J. Breiding, and L. Xu, “Traumatic Brain Injury–Related Emergency Department Visits, Hospitalizations, and Deaths — United States, 2007 and 2013,” *MMWR. Surveill. Summ.*, vol. 66, no. 9, pp. 1–16, Mar. 2017.
[34] “Impact of Stroke (Stroke statistics).” [Online]. Available: http://www.strokeassociation.org/STROKEORG/AboutStroke/Impact-of-Stroke-Stroke-statistics_UCM_310728_Article.jsp#.Wndwdqhl9Pb. [Accessed: 04-Jan-2018].
[35] I. Carpinella, J. Jonsdottir, and M. Ferrarin, “Multi-finger coordination in healthy subjects and stroke patients: A mathematical modelling approach,” *J. Neuroeng. Rehabil.*, vol. 8, no. 1, p. 19, 2011.
[36] “What is stroke? | Stroke.org.” [Online]. Available: http://www.stroke.org/understand-stroke/what-stroke. [Accessed: 04-Jan-2018].
[37] C. S. Mang, K. L. Campbell, C. J. D. Ross, and L. A. Boyd, “Promoting Neuroplasticity for Motor Rehabilitation After Stroke: Considering the Effects of Aerobic Exercise and Genetic Variation on Brain-Derived Neurotrophic Factor,” *Phys. Ther.*, vol. 93, no. 12, pp. 1707–1716, 2013.
[38] “Parkinson’s Foundation: Better Lives. Together.” [Online]. Available: http://parkinson.org/Understanding-Parkinsons/Causes-and-Statistics/Statistics. [Accessed: 04-Feb-2018].
[39] A. P. Rocha, H. Choupina, J. M. Fernandes, M. J. Rosas, R. Vaz, and J. P. Silva Cunha, “Parkinson’s disease assessment based on gait analysis using an innovative RGB-D camera system,” *2014 36th Annu. Int. Conf. IEEE Eng. Med. Biol. Soc.*, pp. 3126–3129, 2014.
[40] M. D. Mayes *et al.*, “Prevalence, incidence, survival, and disease characteristics of systemic sclerosis in a large US population,” *Arthritis Rheum.*, vol. 48, no. 8, pp. 2246–2255, 2003.
[41] National Spinal Cord Injury Statistical Center, “Spinal cord injury. Facts and figures at a glance.,” *J. Spinal Cord Med.*, vol. 28, no. 4, pp. 379–80, 2005.
[42] “WHO | Spinal cord injury,” *WHO*, 2016.
[43] K. Nas, “Rehabilitation of spinal cord injuries,” *World J. Orthop.*, vol. 6, no. 1, p. 8, 2015.
[44] A. E. Barr, M. F. Barbe, S. Billing, B. D. Clark, S. Changes, and F. Email, “Work-Related Musculoskeletal Disorders :,” *Rev. Lit. Arts Am.*, vol. 03970, 2004.
[45] M. Trybus, J. Lorkowski, L. Brongel, and W. Hľadki, “Causes and consequences of hand

injuries," *Am. J. Surg.*, vol. 192, no. 1, pp. 52–57, 2006.
[46] M. Abreu, "Conceção de uma luva sensorial para avaliação da capacidade de aposição do polegar," FEUP, 2015.
[47] "Twin-axis Goniometer 110mm, BSL | SS20L, SS21L, SS22L, SS23L | Education, Research | BIOPAC." [Online]. Available: https://www.biopac.com/product/goniometers-torsiometers-dsub9/. [Accessed: 04-Feb-2018].
[48] M. de Kraker, R. W. Selles, T. A. R. Schreuders, S. E. R. Hovius, and H. J. Stam, "The Pollexograph??: A New Device for Palmar Abduction Measurements of the Thumb," *J. Hand Ther.*, vol. 22, no. 3, pp. 271–277, 2009.
[49] "Joat Resources Sdn Bhd." [Online]. Available: http://joat.com.my/product/measuring/hand.html. [Accessed: 02-Jan-2018].
[50] "Grip Repair, Inc. - Specializing in Hand Therapy Equipment Since 1992." [Online]. Available: https://www.griprepair.com/large_hydraul_pinch.htm. [Accessed: 11-Jan-2018].
[51] "Jamar Hydraulic Hand Dynamometer | OPC Health." [Online]. Available: http://www.opchealth.com.au/jamar-hand-dynamometer. [Accessed: 11-Jan-2018].
[52] F. Cutolo *et al.*, "A sensorized glove for hand rehabilitation," *Bioeng. Proc. Northeast Conf.*, 2009.
[53] D. J. Sturman and D. Zeltzer, "A Survey of Glove-based Input," *IEEE Comput. Graph. Appl.*, vol. 14, no. 1, pp. 30–39, 1994.
[54] J. Peddie, *Augmented Reality*. Cham: Springer International Publishing, 2017.
[55] "Data Gloves | 5DT." [Online]. Available: http://www.5dt.com/data-gloves/. [Accessed: 12-Jan-2018].
[56] J. Connolly, J. Condell, B. O'Flynn, J. T. Sanchez, and P. Gardiner, "IMU Sensor-based Electronic Goniometric Glove (iSEG-Glove) for clinical finger movement analysis," *IEEE Sens. J.*, vol. 1748, no. c, pp. 1273–1281, 2017.
[57] J. Connolly, J. Condell, K. Curran, and P. Gardiner, "A new method to determine joint range of movement and stiffness in rheumatoid arthritic patients," *Proc. Annu. Int. Conf. IEEE Eng. Med. Biol. Soc. EMBS*, pp. 6386–6389, 2012.
[58] "Section 17: Virtual Reality." [Online]. Available: https://excelsior.asc.ohio-state.edu/~carlson/history/lesson17.html. [Accessed: 12-Jan-2018].
[59] Z. Shen, J. Yi, X. Li, L. H. P. Mark, Y. Hu, and Z. Wang, "A soft stretchable bending sensor and data glove applications," *2016 IEEE Int. Conf. Real-Time Comput. Robot. RCAR 2016*, pp. 88–93, 2016.
[60] "Flex Sensor." [Online]. Available: https://www.sparkfun.com/datasheets/Sensors/Flex/FlexSensor.pdf. [Accessed: 18-Jan-2018].
[61] G. Saggio, "Bend sensor arrays for hand movement tracking in biomedical systems," *Proc. 4th IEEE Int. Work. Adv. Sensors Interfaces, IWASI 2011*, pp. 51–54, 2011.
[62] N. P. Oess, J. Wanek, and A. Curt, "Design and evaluation of a low-cost instrumented glove for hand function assessment," *J. Neuroeng. Rehabil.*, vol. 9, no. 1, p. 2, 2012.
[63] D. L. Gardner, "Inside story on: The power glove," *Des. News*, vol. 45, no. 23, p. 63, 1989.
[64] "CyberGlove III — CyberGlove Systems LLC." [Online]. Available: http://www.cyberglovesystems.com/cyberglove-iii/. [Accessed: 18-Jan-2018].
[65] "Product Information Datasheet." [Online]. Available: https://manus-vr.com/pdf/datasheet-manusvr.pdf. [Accessed: 18-Jan-2018].
[66] "A brief history of wearable gaming." [Online]. Available: https://www.wareable.com/gaming/the-history-of-wearable-gaming. [Accessed: 18-Jan-2018].
[67] "Manus VR." [Online]. Available: https://manus-vr.com/press/. [Accessed: 18-Jan-2018].
[68] "StretchSense | Soft Robotics Toolkit." [Online]. Available: https://softroboticstoolkit.com/stretchsense. [Accessed: 18-Jan-2018].
[69] "Stretch Sense." [Online]. Available: https://www.stretchsense.com/. [Accessed: 05-Feb-2018].
[70] D. Roetenberg, H. Luinge, and P. Slycke, "Xsens MVN: Full 6DOF Human Motion

Tracking using Miniature Inertial Sensors," *Xsens Motion Technol.*, no. April, pp. 1–9, 2013.
[71] K. Karimi, "The Role of Sensor Fusion and Remote Emotive Computing (REC) in the Internet of Things," 2013.
[72] H. G. Kortier, V. I. Sluiter, D. Roetenberg, and P. H. Veltink, "Assessment of hand kinematics using inertial and magnetic sensors Assessment of hand kinematics using inertial and magnetic sensors," 2014.
[73] "Synertial IGS Cobra Glove - Tracklab." [Online]. Available: http://tracklab.com.au/products/hardware/synertial-igs-cobra-glove/. [Accessed: 19-Jan-2018].
[74] "COBRA GLOVES | Synertial." [Online]. Available: https://www.synertial.com/cobragloves. [Accessed: 19-Jan-2018].
[75] D. F. Stegeman *et al.*, "Applications of the PowerGlove in healthy aging and Parkinson ' s disease," pp. 381–384.
[76] B. O' Flynn *et al.*, "Integrated Smart Glove for Hand Motion Monitoring," *SENSORCOMM 2015 Ninth Int. Conf. Sens. Technol. Appl.*, no. c, pp. 45–50, 2015.
[77] P. C. Hsiao, S. Y. Yang, B. S. Lin, I. J. Lee, and W. Chou, "Data glove embedded with 9-axis IMU and force sensing sensors for evaluation of hand function," *Proc. Annu. Int. Conf. IEEE Eng. Med. Biol. Soc. EMBS*, vol. 2015–Novem, pp. 4631–4634, 2015.
[78] "Polhemus Electromagnetics." [Online]. Available: http://polhemus.com/applications/electromagnetics/. [Accessed: 18-Jan-2018].
[79] F. Raab, E. Blood, T. Steiner, and H. Jones, "Magnetic Position and Orientation Tracking System," *IEEE Trans. Aerosp. Electron. Syst.*, vol. AES-15, no. 5, pp. 709–718, Sep. 1979.
[80] I. Oikonomidis, N. Kyriazis, and A. Argyros, "Efficient model-based 3D tracking of hand articulations using Kinect," *Procedings Br. Mach. Vis. Conf. 2011*, p. 101.1-101.11, 2011.
[81] "Markers - Markers & Targets - Products - ART Advanced Realtime Tracking." [Online]. Available: https://ar-tracking.com/products/markers-targets/markers/. [Accessed: 19-Jan-2018].
[82] "Fingertracking - Interaction - Products - ART Advanced Realtime Tracking." [Online]. Available: https://ar-tracking.com/products/interaction/fingertracking/. [Accessed: 19-Jan-2018].
[83] "Motion Capture for Life Science | VICON." [Online]. Available: https://www.vicon.com/motion-capture/life-sciences. [Accessed: 19-Jan-2018].
[84] J. Abreu, G. Leporace, and L. Menegaldo, "Hand kinematics evaluation using bts smart," pp. 3–4, 2013.
[85] W. Goebl, "Movement and Touch in Piano Performance," in *Handbook of Human Motion*, Cham: Springer International Publishing, 2017, pp. 1–18.
[86] P. Lukowicz, T. Kirstein, and G. Tröster, "Wearable systems for health care applications," *Methods Inf. Med.*, vol. 43, no. 3, pp. 232–238, 2004.
[87] A. Nayyar and V. Puri, "Data Glove: Internet of Things (IoT) Based Smart Wearable Gadget," *Br. J. Math. Comput. Sci.*, vol. 15, no. 5, pp. 1–12, 2016.
[88] A. Lymberis and L. Gatzoulis, "Wearable health systems: From smart technologies to real applications," *Annu. Int. Conf. IEEE Eng. Med. Biol. - Proc.*, pp. 6789–6792, 2006.
[89] V. Custodio, F. J. Herrera, G. López, and J. I. Moreno, *A review on architectures and communications technologies for wearable health-monitoring systems*, vol. 12, no. 10. 2012.
[90] Z. A. Khan, S. Sivakumar, W. Phillips, and B. Robertson, "ZEQoS : A New Energy and QoS-Aware Routing Protocol for Communication of Sensor Devices in Healthcare System," vol. 2014, 2014.
[91] M. Chan, D. Estève, J.-Y. Fourniols, C. Escriba, and E. Campo, "Smart wearable systems: Current status and future challenges," *Artif. Intell. Med.*, vol. 56, no. 3, pp. 137–156, 2012.
[92] A. Aliverti, "Wearable technology: Role in respiratory health and disease," *Breathe*, vol. 13, no. 2, pp. e27–e36, 2017.
[93] D. Dias, "VitalLogger: An adaptable wearable physiology and body-Area ambiance data logger for mobile applications," FEUP, 2015.

[94] T. Yilmaz, R. Foster, and Y. Hao, “Detecting vital signs with wearable wireless sensors,” *Sensors*, vol. 10, no. 12, pp. 10837–10862, 2010.
[95] R. Negra, I. Jemili, and A. Belghith, “Wireless Body Area Networks: Applications and Technologies,” *Procedia Comput. Sci.*, vol. 83, pp. 1274–1281, Jan. 2016.
[96] H. F. Rashvand and J. M. Alcaraz Calero, *Distributed sensor systems : practice and applications*. Wiley, 2012.
[97] J. Manuel, “VitalSensors - New wearable sensors for monitoring First Responders.” FEUP, 2015.
[98] “The Wearable Health Revolution,” 2014.
[99] “IDC Reveals Health Insights Predictions for 2015 | Business Wire.” [Online]. Available: https://www.businesswire.com/news/home/20141120005148/en/IDC-Reveals-Health-Insights-Predictions-2015. [Accessed: 22-Jan-2018].
[100] “Orange Healthcare.” [Online]. Available: http://healthcare.orange.com/en/Home. [Accessed: 22-Jan-2018].
[101] “Is Wearable Technology the Future of Healthcare? - RapidValue.” [Online]. Available: https://www.rapidvaluesolutions.com/wearable-technology-the-future-of-healthcare/. [Accessed: 22-Jan-2018].
[102] “Wearable band shipments rocket by 684% | Canalys.” [Online]. Available: https://www.canalys.com/newsroom/wearable-band-shipments-rocket-684. [Accessed: 22-Jan-2018].
[103] H. Lewy, “Wearable technologies – future challenges for implementation in healthcare services,” *Healthc. Technol. Lett.*, vol. 2, no. 1, pp. 2–5, 2015.
[104] M. Haghi, K. Thurow, and R. Stoll, “Wearable devices in medical internet of things: Scientific research and commercially available devices,” *Healthc. Inform. Res.*, vol. 23, no. 1, pp. 4–15, 2017.
[105] J. Nikolic and F. Renaut, “MEMS Inertial Sensors Technology,” *Students.Asl.Ethz.Ch*, 2013.
[106] C. C. Yang and Y. L. Hsu, “A review of accelerometry-based wearable motion detectors for physical activity monitoring,” *Sensors*, vol. 10, no. 8, pp. 7772–7788, 2010.
[107] M. Kok, J. D. Hol, and T. B. Schön, “Using Inertial Sensors for Position and Orientation Estimation,” 2017.
[108] A. Albarbar and S. H. Teay, “MEMS Accelerometers : Testing and Practical Approach for Smart Sensing and Machinery Diagnostics.”
[109] “Advantage of capacitive MEMS accelerometers vs other technologies.” [Online]. Available: https://www.slideshare.net/Colibrys/advantage-of-capacitive-mems-accelerometers-vs-other-technologies. [Accessed: 01-Feb-2018].
[110] R. Antonello and R. Oboe, “MEMS Gyroscopes for Consumer and Industrial Applications,” *Microsensors*, no. June 2011, pp. 253–280, 2011.
[111] Y. Cai, Y. Zhao, X. Ding, and J. Fennelly, “Magnetometer basics for mobile phone applications,” *Electron. Prod. (Garden City, New York)*, vol. 54, no. 2, 2012.
[112] S. Tumanski, “Modern Magnetic Field Sensors – A Review,” *Przegląd Elektrotechniczny*, no. 10, pp. 1–12, 2013.
[113] M. Magnetics, “Magnetic tunnel junction sensor development for industrial applications.”
[114] G. Laghi, “MEMS magnetometers: from application specifications to the development and characterization of a prototype beyond the state of the art,” Politecnico di Milano, 2015.
[115] M. J. Thompson and D. A. Horsley, “Lorentz force mems magnetometer,” *Proc. 2010 Work. Solid-State Sensors, Actuators Microsystems Work.*, pp. 2–5, 2010.
[116] S. O. H. Madgwick, “An efficient orientation filter for inertial and inertial/magnetic sensor arrays,” *Rep. x-io Univ. …*, p. 32, 2010.
[117] H. Figueiredo, A. Bittar, and O. Saotome, “Platform for quadrirotors: Analysis and applications,” *2014 Int. Conf. Unmanned Aircr. Syst. ICUAS 2014 - Conf. Proc.*, pp. 848–856, 2014.
[118] J. L. Marins, Xiaoping Yun, E. R. Bachmann, R. B. McGhee, and M. J. Zyda, “An extended Kalman filter for quaternion-based orientation estimation using MARG sensors,” *Proc. 2001 IEEE/RSJ Int. Conf. Intell. Robot. Syst. Expand. Soc. Role Robot.*

Next Millenn. (Cat. No.01CH37180), vol. 4, pp. 2003–2011, 2003.
[119] A. Noureldin, T. B. Karamat, and J. Georgy, *Fundamentals of inertial navigation, satellite-based positioning and their integration*. 2013.
[120] H. Schaub and J. L. Junkins, *Analytical mechanics of space systems*. American Institute of Aeronautics and Astronautics, 2009.
[121] P. Berner *et al.*, "Technical Concepts Orientation, Rotation, Velocity and Acceleration, and the SRM," *TENA (Test Train. Enabling Archit. Proj. by SEDRIS*, no. June, p. 21, 2008.
[122] T. R. Penn, "All Source Sensor Integration Using an Extended Kalman Filter," 2012.
[123] N. Ho, Q. Phuong, S. Korea, H. Kang, Y. Suh, and Y. Ro, "A DCM Based Orientation Estimation Algorithm with an Inertial Measurement Unit and a Magnetic Compass," *J. Univers. Comput. Sci.*, vol. 15, no. 4, pp. 859–876, 2009.
[124] A. M. Sabatini, "Kalman-filter-based orientation determination using inertial/magnetic sensors: Observability analysis and performance evaluation," *Sensors*, vol. 11, no. 10, pp. 9182–9206, 2011.
[125] S. O. H. Madgwick, A. J. L. Harrison, and R. Vaidyanathan, "Estimation of IMU and MARG orientation using a gradient descent algorithm," *IEEE Int. Conf. Rehabil. Robot.*, pp. 1–7, 2011.
[126] A. Brandsma, "Computing the orientation of an IMU sensor Comparing the EKF and the SO (3) filter," no. 3, 2016.
[127] T. Filipe and R. Catarino, "Development of a Hand-Tracker :," no. September, 2016.
[128] A. Jensen, C. Coopmans, and Y. Chen, "Basics and guidelines of complementary filters for small UAS navigation," *2013 Int. Conf. Unmanned Aircr. Syst. ICUAS 2013 - Conf. Proc.*, pp. 500–507, 2013.
[129] R. Mahony, T. Hamel, J.-M. Pflimlin, J.-M. Pflimlin Nonlinear, and R. Mahony, "Complementary Filters on the Special Orthogonal Group," *IEEE Trans. Autom. Control. Inst. Electr. Electron. Eng.*, vol. 53, no. 5, pp. 1203–1217, 2008.
[130] F. Alam, Z. Zhaihe, and H. Jiajia, "A Comparative Analysis of Orientation Estimation Filters using MEMS based IMU," *2nd Int. Conf. Res. Sci. Eng. Technol.*, pp. 86–91, 2014.
[131] "MPU-9250 Hookup Guide - learn.sparkfun.com." [Online]. Available: https://learn.sparkfun.com/tutorials/mpu-9250-hookup-guide. [Accessed: 31-Jan-2018].
[132] InvenSense Inc., "MPU-9250 Product Specification," vol. 1, no. 408, 2016.
[133] "I2C - learn.sparkfun.com." [Online]. Available: https://learn.sparkfun.com/tutorials/i2c. [Accessed: 31-Jan-2018].
[134] InvenSense Inc., "MPU-9250 Product Specification," vol. 1, no. 408, p. 42, 2014.
[135] S. Jose, "MPU9250 Datasheet," *Prod. Specif.*, vol. 1, no. 408, pp. 1–4, 2016.
[136] "Arduino Pro Mini 328 - 3.3V/8MHz - DEV-11114 - SparkFun Electronics." [Online]. Available: https://www.sparkfun.com/products/11114?_ga=2.106735747.1028938250.1517286790-1288065613.1516237994. [Accessed: 31-Jan-2018].
[137] "SparkFun FTDI Basic Breakout - 3.3V - DEV-09873 - SparkFun Electronics." [Online]. Available: https://www.sparkfun.com/products/9873?_ga=2.212157844.1028938250.1517286790-1288065613.1516237994. [Accessed: 31-Jan-2018].
[138] Microchip Technology Inc., "RN4870/71 Bluetooth 4.2 Low Energy Module: Data Sheet," 2016.
[139] "RN4871 - Wireless - Bluetooth Module." [Online]. Available: http://www.microchip.com/wwwproducts/en/RN4871. [Accessed: 31-Jan-2018].
[140] "RN4871-V/RM118 Microchip Technology | RF/IF and RFID | DigiKey." [Online]. Available: https://www.digikey.com/product-detail/en/microchip-technology/RN4871-V-RM118/RN4871-V-RM118-ND/6130476. [Accessed: 31-Jan-2018].
[141] J. Valdez and J. Becker, "Understanding the I2C Bus," *Slva704*, no. June, pp. 1–8, 2015.
[142] "I2C - learn.sparkfun.com." [Online]. Available: https://learn.sparkfun.com/tutorials/i2c. [Accessed: 30-Jan-2018].
[143] "Serial Communication - learn.sparkfun.com." [Online]. Available: https://learn.sparkfun.com/tutorials/serial-communication. [Accessed: 31-Jan-2018].

[144] “GATT | Introduction to Bluetooth Low Energy | Adafruit Learning System.” [Online]. Available: https://learn.adafruit.com/introduction-to-bluetooth-low-energy/gatt. [Accessed: 03-Sep-2018].
[145] *RN4020 Bluetooth ® Low Energy Module User ’ s Guide*. 2014.
[146] “SparkFun MPU-9250 Breakout Arduino Library MPU9250.” [Online]. Available: https://github.com/sparkfun/SparkFun_MPU-9250_Breakout_Arduino_Library/blob/master/src/MPU9250.cpp.
[147] “GitHub - SodaqMoja Microchip RN487x.” [Online]. Available: https://github.com/SodaqMoja/Microchip_RN487x.
[148] A. Team, “Arduino - SoftwareSerial,” 2015. [Online]. Available: http://arduino.cc/en/Reference/SoftwareSerial.
[149] Arduino Inc., “Arduino - EEPROM,” *Arduino*, 2018. [Online]. Available: http://arduino.cc/es/Reference/EEPROM.
[150] K. Winer, “Simple and Effective Magnetometer Calibration,” 2015. [Online]. Available: https://github.com/kriswiner/MPU-6050/wiki/Simple-and-Effective-Magnetometer-Calibration.
[151] “Title Data Fusion Filters for Attitude Heading Reference System (AHRS) with Several Variants of the Kalman Filter and the Mahoney and Madgwick Filters,” 2015.
[152] D. Giavarina, “Understanding Bland Altman analysis Lessons in biostatistics,” *Biochem. Medica*, vol. 25, no. 2, pp. 141–51, 2015.
[153] “TinyDB - Android (Shared Preferences) Turbo.” [Online]. Available: https://github.com/kcochibili/TinyDB--Android-Shared-Preferences-Turbo.
[154] “GitHub - min3d - A 3d library framework for Android using Java and OpenGL ES.” [Online]. Available: https://github.com/mengdd/min3d.
[155] “rigging - Hand model keeps bending finger when wrist is rotated - Blender Stack Exchange.” [Online]. Available: https://blender.stackexchange.com/questions/41089/hand-model-keeps-bending-finger-when-wrist-is-rotated?utm_medium=organic&utm_source=google_rich_qa&utm_campaign=google_rich_qa. [Accessed: 03-Sep-2018].
[156] “Android Graph View plotting library.” [Online]. Available: http://www.android-graphview.org/. [Accessed: 03-Sep-2018].
[157] “Biokinetic Golf Swing Theory: February 2012.” [Online]. Available: http://biokineticgolfswing.blogspot.com/2012/02/. [Accessed: 03-Sep-2018].
[158] “Pronation and ISR Clarification (Question for Chas_Tennis) | Talk Tennis.” [Online]. Available: https://tt.tennis-warehouse.com/index.php?threads/pronation-and-isr-clarification-question-for-chas_tennis.546324/. [Accessed: 03-Sep-2018].
[159] A. Sofia, M. De Castro, and R. Assis, “Kinematic evaluation of Parkinson ’ s disease patients during Deep Brain Stimulation surgery and pre-operative procedures,” FEUP, 2016.
[160] “Goniometer for Flexibility Measurement.” [Online]. Available: https://www.topendsports.com/testing/products/goniometer.htm. [Accessed: 03-Sep-2018].
[161] T. I. Carter *et al.*, “Accuracy and Reliability of Three Different Techniques for Manual Goniometry for Wrist Motion: A Cadaveric Study,” *J. Hand Surg. Am.*, vol. 34, no. 8, pp. 1422–1428, Oct. 2009.
[162] “Goniometry | Courses.” [Online]. Available: http://www.scranton.edu/faculty/kosmahl/courses/gonio/upper/index.shtml. [Accessed: 03-Sep-2018].